

Molecular dynamics simulations of self-assembled monolayers in the context of area-selective atomic layer deposition

Eva VANDAELE

Supervisor: Prof. Dr. A. Delabie
KU Leuven - IMEC

Supervisor: Prof. Dr. J. Harvey
KU Leuven

Mentor: Dr. T. Mihaylov
KU Leuven

Thesis presented in
fulfillment of the requirements
for the degree of Master of Science
in Chemistry

Academic year 2016-2017

©Copyright by KU Leuven

Without written permission of the promotors and the authors it is forbidden to reproduce or adapt in any form or by any means any part of this publication. Requests for obtaining the right to reproduce or utilize parts of this publication should be addressed to KU Leuven, Faculteit Wetenschappen, Geel Huis, Kasteelpark Arenberg 11 bus 2100, 3001 Leuven (Heverlee), Telephone +32 16 32 14 01.

A written permission of the promotor is also required to use the methods, products, schematics and programs described in this work for industrial or commercial use, and for submitting this publication in scientific contests.

Summary

The aim of this thesis is to contribute to the miniaturisation of integrated circuits (ICs) by investigating area-selective atomic layer deposition (AS-ALD). AS-ALD is a bottom-up technique for pattern replication with molecular level control based on the selective surface reactions of atomic layer deposition (ALD) precursor molecules on a pre-patterned substrate. The selectivity can be induced or enhanced by selective surface passivation in the areas where deposition of the film is not wanted. The surface can be passivated by hydrophobic self-assembled monolayers (SAMs). SAMs are dense, ordered monolayers that are spontaneously formed by the adsorption of organic molecules on a surface. For example, the adsorption of alkanethiol molecules on metal surfaces inhibits the deposition of metal oxide films on the metal. Nevertheless, not all ALD precursor molecules are equally inhibited. In addition, defects in the SAM act as nucleation sites for thin film deposition.

The SAM passivating properties were investigated in this thesis by molecular dynamics simulations. First, the structure of a dodecanethiol monolayer on a Au(111) surface was simulated at various temperatures to monitor the conformational changes of the SAM. At low temperatures (200 K), the SAM is perfectly ordered. A dense barrier is formed. In contrast, at higher temperatures (400 K), a disordered monolayer is observed. Hence, the temperature at which the ALD process is performed is an important factor for the applicability of AS-ALD.

Second, the presence of intrinsic diffusion channels in a perfect monolayer was investigated by simulating the interaction of gold atoms with the SAM. Although experiments revealed a continuous penetration of the monolayer, no diffusion in the SAM was observed during 100 ns simulations at low (200 K) and high (600 K) temperatures. These observations suggest that the penetration of gold atoms in the SAM is caused by defects or by transient diffusion channels formed by fluctuations in the alkanethiol positions.

Finally, the interaction of trimethylaluminium (TMA) molecules with a dodecanethiol SAM was examined. TMA is a frequently used precursor molecule in ALD of aluminium oxide films. Since the OPLS force field does not contain atom types for aluminium atoms, a TMA molecule was parametrised and the force field was extended. At 400 K, the TMA molecules clustered on top of the SAM surface, but no penetration was observed. Point and line defects were subsequently introduced by removing dodecanethiol molecules from the monolayer. The removal of two molecules from the monolayer resulted in the diffusion

of TMA to the substrate-SAM interface, where reaction with the Au or S atoms might occur. Hence, the presence of small pinholes in the SAM is sufficient to introduce ALD nucleation sites at the substrate-SAM interface.

Samenvatting

Het doel van deze thesis is om bij te dragen aan de miniaturisatie van geïntegreerde schakelingen door de oppervlakte selectieve atoomlaag depositie (AS-ALD) te onderzoeken. AS-ALD is een *bottom-up* techniek om patronen reproduceren met een moleculaire precisie gebaseerd op de selectieve chemisorptie van atoomlaag depositie (ALD) precursor moleculen op een heterogeen substraat. De selectiviteit kan verbeterd worden door het oppervlak te passiveren op gebieden waar de depositie niet gewenst is. Dit wordt verwezenlijkt door hydrofobe zelf-geassembleerde monolagen (SAMs) te vormen. SAMs zijn dense, geordende monolagen gevormd door de spontane adsorptie van organische moleculen op een oppervlak. De adsorptie van alkaanthiolen op metaaloppervlakken, bijvoorbeeld, kan de depositie van een metaaloxide film op het oppervlak blokkeren. Niet elke ALD precursor wordt echter evenveel verhinderd en defecten in de monolaag resulteren in de nucleatie van precursor moleculen op het substraat.

In deze thesis zijn de passiverende eigenschappen van de SAM onderzocht via moleculaire dynamica simulaties. Een dodecaanthiol monolaag op Au(111) is eerst gesimuleerd bij verschillende temperaturen om de conformationele veranderingen in de SAM na te gaan. Bij lage temperaturen, gelijk aan 200 K, is de SAM perfect geordend. Een dichte barrière wordt gevormd. Bij hogere temperaturen daarentegen, hoger dan 400 K, is de monolaag wanordelijk. De temperatuur waarbij het ALD proces uitgevoerd wordt is dus cruciaal voor de toepasbaarheid van AS-ALD.

Vervolgens is aanwezigheid van intrinsieke diffusiekanalen in een perfecte monolaag onderzocht door de interactie van goud atomen met de SAM te simuleren. Hoewel een continue penetratie van de monolaag geconcludeerd werd in experimenten, resulteerden 100 ns simulaties bij lage (200 K) en hoge (600 K) temperaturen niet in diffusie. Dit resultaat suggereert dat de diffusie van goud atomen in de SAM veroorzaakt wordt door defecten of door tijdelijke diffusiekanalen gevormd via fluctaties in de alkaanthiol posities.

Tot slot is de diffusie van trimethylaluminium (TMA) molecules in de SAM onderzocht. TMA is een populaire precursor voor de depositie van aluminiumoxide films via de ALD techniek. Aangezien het OPLS krachtveld geen atoomtypes voor aluminium atomen bevat, werd een TMA molecule geparametriseerd en het krachtveld uitgebreid. De TMA molecules vormden clusters op het SAM oppervlak bij 400 K, maar diffusie werd niet geobserveerd. Punt- en lijndefecten zijn vervolgens geïntroduceerd door dodecaanthiol moleculen te verwijderen uit de monolaag. De verwijdering van twee moleculen resulteerde in TMA diffusie

naar het substraat-SAM grensvlak, waar reactie met de goud of zwavel atomen mogelijk is. De aanwezigheid van kleine puntdefecten is dus voldoende om de nucleatie van ALD precursoren aan het substraat-SAM grensvlak mogelijk te maken.

Acknowledgements

I would like to thank my promotors and mentor for their help and advice during this project. This thesis would not have been possible without their excellent guidance. I am grateful to Prof. Delabie for introducing me to the interesting topic of area-selective deposition. Her enthusiasm always motivated me. My gratitude goes to Prof. Harvey, whose expertise and insights were essential for the success of this thesis. I would like to express my deepest gratitude and appreciation to Dr. Mihaylov for his advice and support. He always made time to help me, inspired me and learned me a lot about computational chemistry and research in general.

I would like to thank Dr. Pourtois for the helpful discussions and his interest in the project. I want to thank my colleagues at the quantum chemistry and physical chemistry department for the many pleasant moments and enriching conversations. I really enjoyed working in this group. I also want to thank my colleagues at IMEC.

Ik zou graag mijn ouders, zus en familie bedanken voor hun steun, begrip en interesse. Tenslotte wil ik mijn liefje, Robin, bedanken voor zijn steun tijdens moeilijke momenten, voor zijn hulp en voor de vele mooie momenten die we de voorbije vier jaar gedeeld hebben.

List of abbreviations

AFM	Atomic Force Microscopy
ALD	Atomic Layer Deposition
AS-ALD	Area-Selective Atomic Layer Deposition
CG	Conjugate Gradient
ChelpG	Charges from Electrostatic Potentials, Grid method
CPU	Central Processing Unit
Def2-TZVP	Default-2-Triple Zeta Valence basis set with Polarisation functions
DEZ	Diethylzinc
DFT	Density Functional Theory
EDS	Energy Dispersive X-ray Spectroscopy
fcc	face-centred cubic
GD3	D3 version of Grimme's Dispersion
GIXD	Grazing Incidence X-ray Diffraction
GPC	Growth Per Cycle
GoIP	Gold-Protein force field
Gromacs	Groningen Machine for Chemical Simulations
hcp	hexagonal close-packed
IC	Integrated Circuit
l-bfgs	limited-memory Broyden-Fletcher-Goldfarb-Shanno quasi-Newtonian minimiser
MD	Molecular Dynamics
MK	Merz-Singh-Kollman scheme
MM	Molecular Mechanics
MP2	Möller-Plesset perturbation theory of the second order
MPI	Message Passing Interface
NN	Nearest-Neighbour
NNN	Next-Nearest Neighbour
OPLS	Optimised Potentials for Liquid Simulations
pbc	Periodic Boundary Conditions
PES	Potential Energy Surface
PME	Particle Mesh Ewald
SAM	Self-Assembled Monolayer
SEM	Scanning Electron Microscopy

stdev.	Standard Deviation
STM	Scanning Tunneling Microscopy
TDMATi	Tetrakis(Dimethylamido)Titanium
TDMASn	Tetrakis(Dimethylamido)Tin
TMA	Trimethylaluminium
TPD	Temperature Programmed Desorption
UA	United-Atom
vdW	van der Waals
VMD	Visual Molecular Dynamics
XPS	X-ray Photoelectron Spectroscopy

Contents

Summary	i
Samenvatting	iii
Acknowledgements	v
List of abbreviations	vi
1 Introduction	1
1.1 Moore's law	1
1.2 Atomic layer deposition	2
1.2.1 Introduction	2
1.2.2 Thin film growth	4
1.2.3 Temperature dependence	4
1.2.4 Al ₂ O ₃ deposition	5
1.3 Top-down and bottom-up patterning	6
1.4 Self-assembled monolayers	7
1.4.1 Introduction	7
1.4.2 The alkanethiol SAM structure on a Au(111) surface	8
1.4.3 Thermal stability of the SAM	13
1.4.4 Defects	14
1.5 Atomic diffusion in SAMs	15
1.6 Area-selective deposition	16
1.6.1 Introduction	16
1.6.2 Impact of the ALD process in area-selective deposition	17
1.6.3 Enhanced selectivity	18
1.7 Problem statement	20
1.8 Objectives	20
1.9 Outline	20
2 Methods	21
2.1 Molecular dynamics	21
2.1.1 The simulation method	21

2.2	Force field	23
2.2.1	Bond stretching and angle bending contributions	23
2.2.2	Dihedral contributions	24
2.2.3	Improper torsions	25
2.2.4	Electrostatic contribution	26
2.2.5	van der Waals contributions	26
2.3	Atom types	27
2.4	Parametrisation	27
2.5	Periodic boundary conditions	28
2.6	Cut-offs	28
2.7	Thermostats	29
2.8	Energy minimisation methods	29
2.9	Density functional theory	30
2.9.1	Level of theory	31
2.9.2	Normal mode analysis	31
2.10	Programs	31
3	Structural model and methodology	33
3.1	Structure of the dodecanethiol SAM on Au(111)	33
3.1.1	Structural model	33
3.1.2	Building of the repeat unit	36
3.1.3	Multiplication of the repeat unit	36
3.2	Set-up for the molecular dynamics simulations	37
3.3	OPLS force field extensions	38
3.3.1	Force field extension for gold atoms	38
3.3.2	TMA parametrisation	39
3.3.3	Force field extension for a SAM	45
4	Results and discussion	47
4.1	Thermal stability of the SAM conformation	48
4.1.1	Simulation set-up	48
4.1.2	Results	49
4.1.3	Discussion	53
4.2	Gold atomic diffusion	56
4.2.1	Simulation set-up	57
4.2.2	Results	58
4.2.3	Discussion	59
4.3	TMA diffusion in a perfect monolayer	61
4.3.1	Simulation set-up	61
4.3.2	Results	63
4.4	TMA diffusion in a defective monolayer	64
4.4.1	Simulation set-up	65
4.4.2	Results	66

4.4.3 Discussion	67
5 Conclusions and outlook	69
Bibliography	72
Appendix A Figures	81
A.1 TMA charges	81
A.2 Temperature dependent SAM conformations	82
A.3 Dihedral distribution function	83
A.4 Average fraction of anti-periplanar torsional angles	85
Appendix B TMA vibrational frequencies	86
Appendix C Parameter files	87
C.1 Parameter file for the energy minimisations	87
C.2 Parameter file for the equilibration runs	87
Appendix D Scripts	89
D.1 Script to multiply the repeat unit	89
D.2 Script to generate the position restraints file	91
D.3 Script to generate the position restraints file for a defective monolayer	91
D.4 Script to change the TMA - propane distance	92

Chapter 1

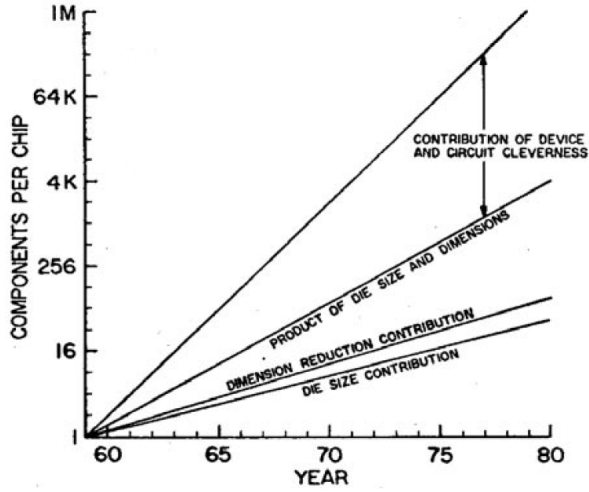
Introduction

1.1 Moore's law

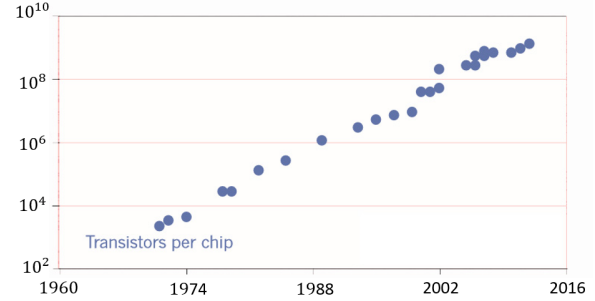
The invention of computers revolutionised our society. People all over the world use a computer every day and our economy relies on it. The main element of a computer is the central processing unit (CPU), which executes all operations. A CPU mostly consists of one chip or integrated circuit (IC), composed of billions of transistors. In 1965, Gordon Moore observed that the number of components on an IC doubled each year [1]. In addition, he predicted this trend to be continued in the future. Ten years later, in 1975, Moore adjusted the period to two years in a speech. Moore's law evolved from an observation and prediction to a goal for the semiconductor industry [2]. Over the years, computers became smaller, cheaper and faster at an astounding rate.

Maintaining the law required a myriad of technological advancements. Figure 1.1a depicts a graph used by Moore in his 1975 speech. He splits the technological improvements leading to the increasing number of transistors in three contributions. The first contribution arises from larger chip areas. The second denotes the dimensional reduction of features, as smaller structures allow for higher transistor densities. Nevertheless, these geometrical changes are not sufficient to explain the observed rate. A third, important contribution is given by new device architectures resulting in better packing efficiencies. Moore revised his initial prediction, because he thought progress here approached a limit.

Today, the third contribution still plays an important role. New devices architectures, materials and manufacturing processes are being developed. In the last decade, the three-dimensional FinFETs [3], new gate dielectric materials [4] and immersion lithography [5] were introduced. Currently, electronic devices are fabricated by the 14 nm process. The 10 nm process is expected to be incorporated later this year. As the dimensions further reduce, physical limits are reached and several researchers question the attainability of Moore's law [6]. Will the pace slow down in the coming years or will industry and academics drastically change today's electronic devices [7, 8]?



(a) Different contributions to the development of ICs according to Moore in 1975.



(b) The evolution of the number of transistors on an IC is still in line with Moore's law. The figure was adapted from ref. [6].

Figure 1.1

1.2 Atomic layer deposition

1.2.1 Introduction

Atomic layer deposition (ALD) has become a very important technique for the manufacturing of nanometre-scaled ICs [9]. ALD is a thin film deposition technique based on sequential self-limiting chemisorption reactions [10, 11]. First, an inorganic, gaseous precursor molecule is adsorbed on a solid substrate. Upon saturation, the reaction by-products and the excess of precursor are removed. A second gas-phase reagent is then introduced, which reacts at the surface to form the desired product. After purging, the cycle can be repeated, as shown in Figure 1.2. The two precursor molecules thus never meet in the gas-phase. The thickness of the final film is determined by the number of reaction cycles.

The ALD process has several advantages [11]. Since the deposition technique is based on self-limiting chemisorption reactions, control of the film thickness at a molecular level is achieved. In contrast to physical deposition techniques, such as physical vapour deposition, the interactions are specific and strong. This can be exploited for selective deposition on a patterned substrate. ALD allows for conformal deposition on three-dimensional substrates. Moreover, the technique can uniformly cover large samples or multiple substrates with variety of inorganic films. The ALD grown materials include oxides, sulphides, nitrides, ... of various elements [10]. ALD processes to deposit new materials are continuously being developed.

Good ALD reactants are volatile, thermally stable at the process temperature and

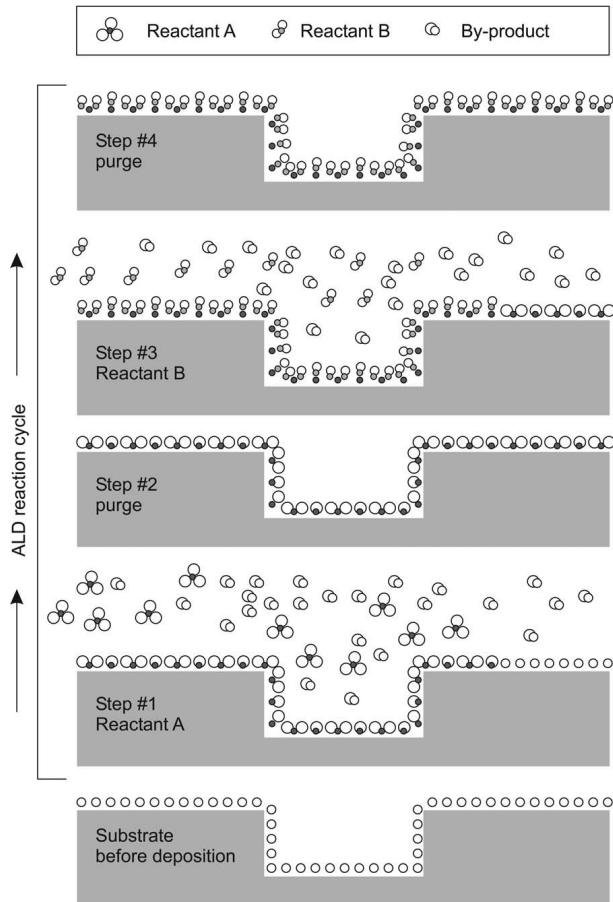


Figure 1.2: Schematic representing one ALD cycle taken from ref. [10].

undergo fast and complete reactions [10]. These properties can be optimised by adequate ligand design. However, ligands can also introduce steric hindrance or impurities in the film. A diverse range of inorganic and metalorganic ligands have been investigated, e.g. halides, cyclopentadienyls, alkoxides, β -diketonates, amidinates, ...

The deposition of an aluminium oxide film by ALD is well studied and serves as a model system [10, 11]. Aluminium oxide is widely investigated due to the large band gap and moderately high dielectric constant [12]. The most common precursor pair is $\text{Al}(\text{CH}_3)_3/\text{H}_2\text{O}$. Other reactants for Al_2O_3 film growth are O_3 , O_2 , H_2O_2 or even NO_2 . TMA is considered as an ideal precursor due to its self-terminating surface reactions and high reactivity. Steric hindrance is the main factor causing saturation of the TMA chemisorption on reactive surfaces. Other advantages include the high vapour pressure and production of inert by-products [13]. Alternatively, a trichloroaluminium precursor can be used. Nevertheless, in this case the ALD process produces corrosive HCl , which can etch the film [13].

1.2.2 Thin film growth

The growth per cycle (GPC) is defined as the amount of material deposited per ALD cycle [10, 14]. This is often less than one monolayer [11]. The GPC depends on the number of reactive surface sites, on the steric repulsion and on the temperature. In the initial stages of the deposition process, different values for the GPC can be observed based on the difference in reactivity of the substrate and the deposited film. Substrate inhibited, enhanced or linear growth can be distinguished, after which the GPC evolves to a constant value.

The different growth modes for ALD processes with GPCs less than one monolayer are given in Figure 1.3: (a) the formation of the second monolayer starts only when the first monolayer is completed. (b) shows the opposite case. In the first cycle nuclei are formed, which subsequently grow until the hemispheres coalesce. This model is called the island growth and is most often observed. Random deposition, (c), is preferred when all reactive sites have an equal probability for chemisorption. It should be emphasised that the GPC and the growth mode are uncorrelated. The reactivity of the substrate cannot be related to the growth mode and vice versa.

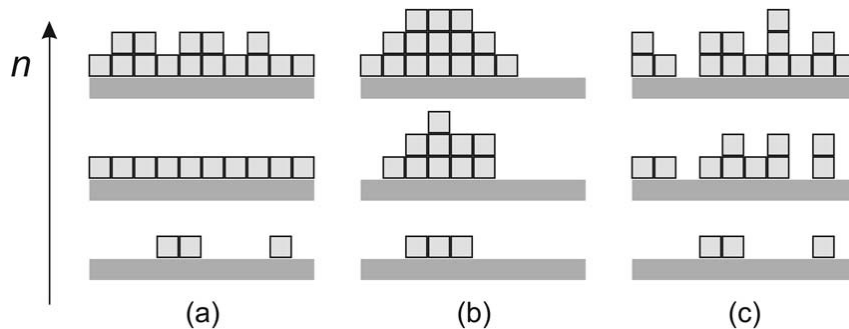


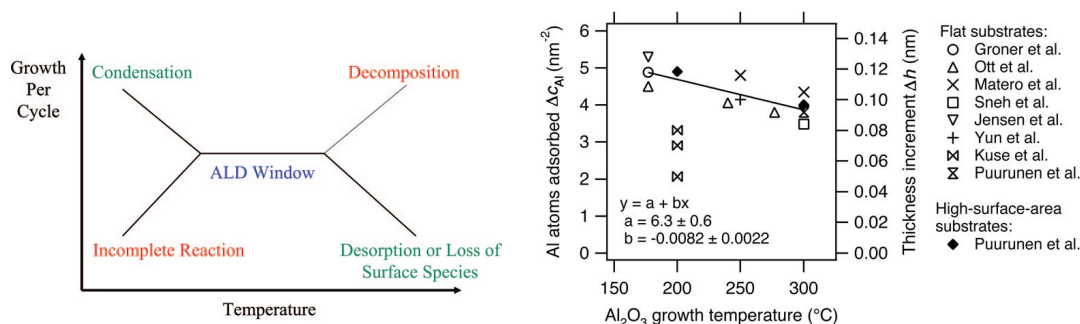
Figure 1.3: Different ALD growth modes versus the cycle number n , taken from ref. [10].

1.2.3 Temperature dependence

The ALD window is defined as the processing temperature range in which the growth proceeds by self-limiting surface reactions, as shown in Figure 1.4a. At too high temperatures, the precursor molecules decompose or desorb from the surface, resulting in limited GPCs [11]. At low temperatures, incomplete reactions and physisorption introduce impurities. In addition, slower mass transport and lower reaction rates increase the time to reach saturation [15]. The GPC can also vary in the ALD window, as the reaction mechanism and the number of active surface sites may depend on the temperature.

The $\text{Al}(\text{CH}_3)_3/\text{H}_2\text{O}$ deposition is characterised by a wide temperature range. Smooth aluminium oxide layers were grown at temperatures as low as 306 K [15]. The upper temperature for the $\text{Al}(\text{CH}_3)_3/\text{H}_2\text{O}$ ALD process is defined by the TMA decomposition at

600 K [16]. Figure 1.4b illustrates the variation of the aluminium oxide GPC within the ALD window. The negative slope of the line is due to the decreasing number of the surface hydroxyl groups [12].



(a) Schematic of the temperature dependence of the GPC. Figure taken from ref. [11].

(b) Temperature dependence of the Al₂O₃ growth. Figure taken from ref. [10].

Figure 1.4

1.2.4 Al₂O₃ deposition

Density functional theory (DFT) calculations on cluster models resolved the Al(CH₃)₃/H₂O ALD reaction mechanism on hydroxyl and thiol terminated Si(100) and Ge(100) substrates [14]. A similar reaction mechanism for the Al(CH₃)₃/H₂O ALD process on hydroxylated alumina substrates was found by periodic DFT calculations [12]. As shown in Figure 1.5, a Lewis acid-base complex between TMA and the hydroxyl/thiol functional group is formed first. The hydroxyl/thiol hydrogen is then transferred to a methyl ligand and a methane molecule is released. The aluminium atom forms a coordinative bond to the substrate to maintain a tetrahedral geometry and a second methane molecule is released by the dimethylaluminium complex. Further dissociation of monomethylaluminium is thermodynamically/kinetically unfavourable for hydroxyl/thiol terminated substrates respectively.

The addition of water molecules causes the liberation of the last Al-bound methyl group to form an aluminium oxide. Nevertheless, a competitive mechanism involves a hydrogen transfer to a substrate - O/S - Al backbond. The resulting monomethylaluminium terminated substrate leads to a lower GPC for the second ALD reaction cycle, as this surface is only slowly hydrolysed. The formation of methyl terminated surfaces and associated ALD blocking from the second cycle on is also observed for TMA chemisorption on a bare substrate. On an oxide material without hydroxyl groups, the TMA methyl groups are transferred to bridging oxygens until saturation of the surface with methyl groups. In standard reaction conditions, the ligand exchange reaction at hydroxyl functional groups

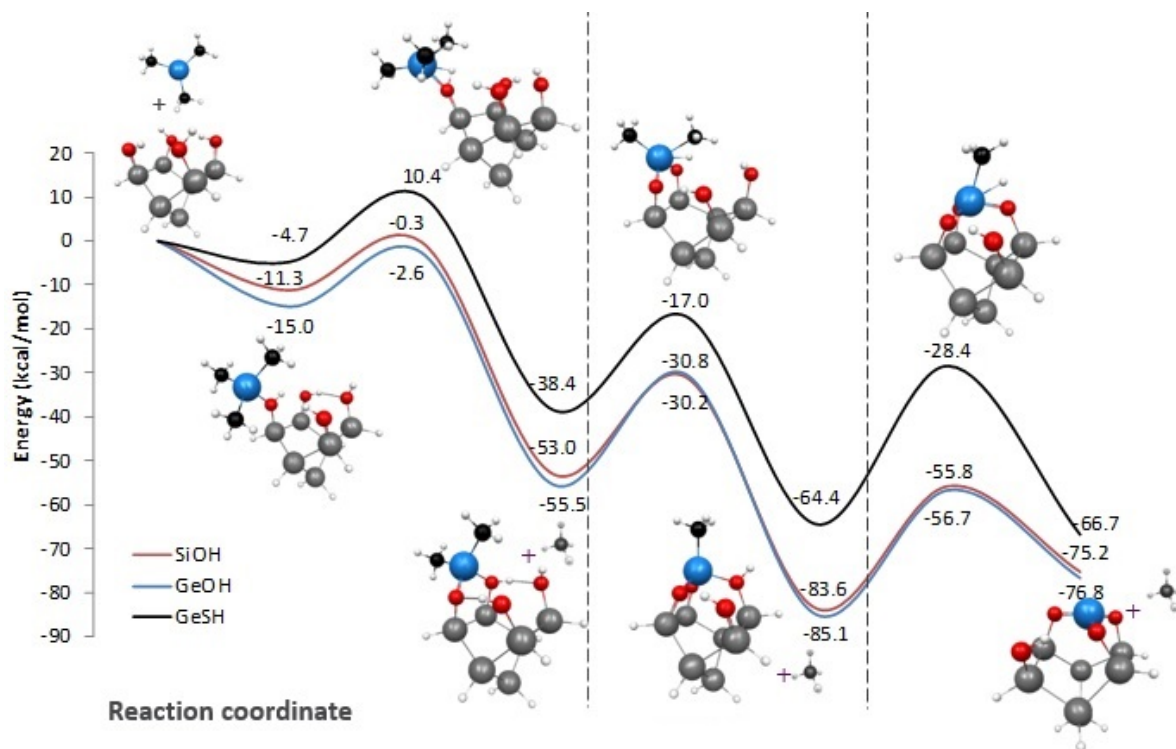


Figure 1.5: Mechanism of the TMA chemisorption reaction on hydroxyl and thiol terminated surfaces according to ref. [14].

and dissociative adsorption on bridge sites compete [12, 17]. Finally, hydrophobic surfaces, such as hydrogen terminated silicon surfaces, effectively inhibit the aluminium oxide ALD process [18].

1.3 Top-down and bottom-up patterning

Although thickness control on an atomic scale can be achieved by the ALD process, the trend towards smaller and more three-dimensional features complicates the fabrication of IC. One of the challenges imposed by the miniaturisation is the patterning. In order to make the ICs, several thin layers of different conducting and isolating materials must be deposited and patterned into a well-defined structures on the chip.

Photolithography is a popular method to pattern various types of materials [19, 20]. A photosensitive resist layer, often a polymer [21], and a patterned mask are placed on top of the substrate. Exposure to ultraviolet light induces photochemical reactions in the resist, after which part of the resist is removed by dissolution. The template is etched in the underlying substrate and the resist is striped off. As a result, the mask pattern is replicated in the matrix material by means of a protective resist layer.

However, the self-alignment error is a major problem of photolithography [22]. While

reproducing a pattern, small shifts can occur, as visualised in Figure 1.6. The continuous downscaling of transistor sizes requires very accurate pattern placement. Errors in the alignment can have large consequences for the performance. In addition, high energy photons are needed to match the wavelength with the device dimensions. Finally, photolithography is a complicated, expensive and time-consuming process [23]. As a result, the development of new patterning methods is an important goal for the semiconductor industry.

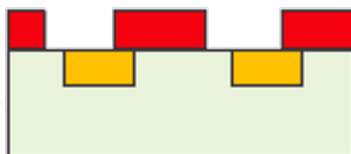


Figure 1.6: Schematic of the edge alignment error.

Bottom-up patterning alternatives are increasingly gaining attention to replace the current top-down approaches [24]. Instead of patterning a material, the next layer is selectively deposited on top of a pre-existing pattern based on a difference in chemical affinity between the different substrate materials. The area-selective ALD process is based on the selective chemisorption of ALD precursor molecules on specific areas of a substrate. For example, it was mentioned in the previous section that the TMA ALD process is inhibited on methyl- and hydrogen-terminated surfaces [14, 18]. The selectivity can be enhanced by surface passivation or activation [22, 23]. Passivation can be achieved by the selective formation of hydrophobic self-assembled monolayers (SAMs) on certain substrate areas. The patterning of integrated circuits by the AS-ALD technique could become more accurate, cheaper, simpler and faster as compared to the traditionally used photolithography. Moreover, the SAM deposition can be performed in the ALD reactor and therefore be integrated in the ALD process. [25].

1.4 Self-assembled monolayers

1.4.1 Introduction

Self-assembled monolayers arise from the spontaneous adsorption and assembly of organic molecules on a surface in well-defined, closely packed structures [26, 27, 28]. The resulting aggregate is an ordered, laterally organised monolayer. One such molecule typically consists of a head group, backbone and end group [29], as shown in Figure 1.7. The solution or vapour-deposited molecules chemisorb on the substrate through the interaction with the headgroup. A dense barrier is formed, since the organic molecules tend to align and tilt with respect to the surface in order to optimise the van der Waals interactions between the backbones [30]. By altering the end group one can modify the surface properties e.g.

the mechanical and physical properties or the reactivity of the surface [29]. The specific properties of several functional end groups have been characterised [26, 31].

The most well-investigated example is the organisation of alkanethiol molecules on metal surfaces. Other examples include the affinity of silanes towards hydroxylated surfaces or the adsorption of phosphonic acids on metal oxides [29, 32]. Due to their easy preparation, stability and controllable surface properties SAMs have a wide variety of applications including catalysis [27], corrosion prevention [33, 34] and adhesion [28, 35]. Their biocompatibility further provides biochemical possibilities e.g. in sensors [36, 37, 38]. In this thesis, the inhibition of the ALD process on a metal surface by a hydrophobic alkanethiol monolayer is examined.

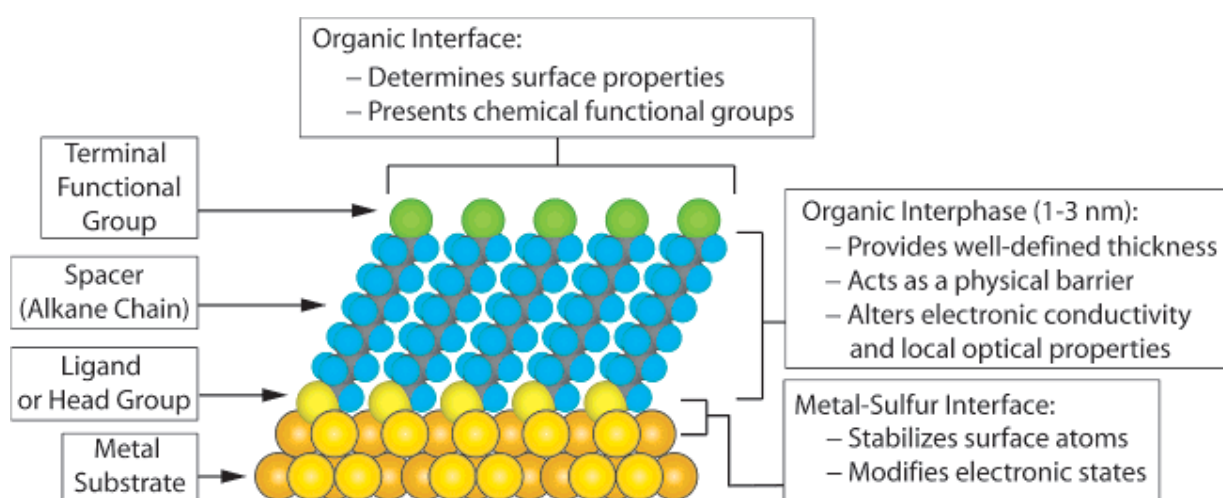


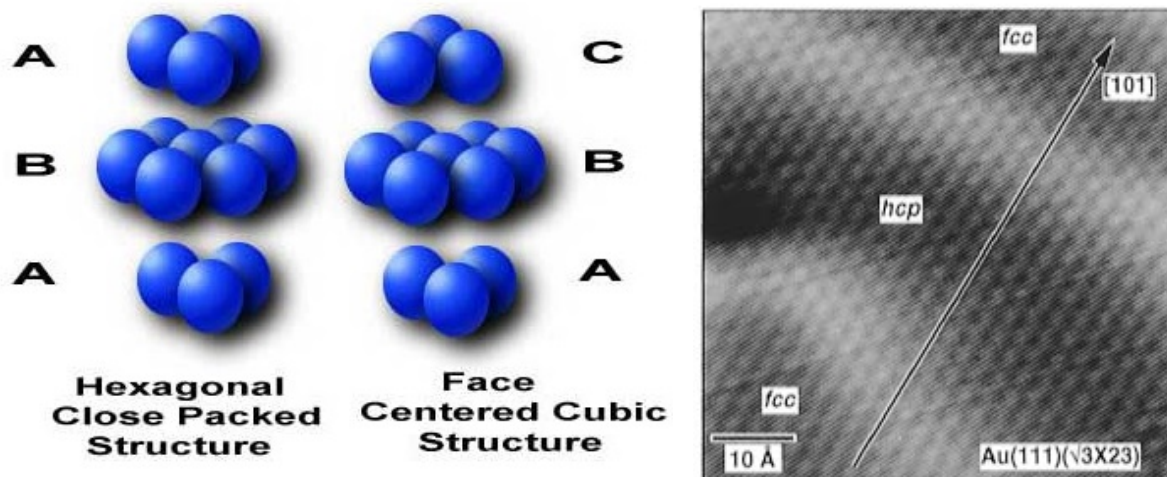
Figure 1.7: Components of an alkanethiol SAM on a Au(111) substrate with their properties. Figure taken from ref. [29].

1.4.2 The alkanethiol SAM structure on a Au(111) surface

The insights in the structure of an alkanethiol SAM on Au(111) grew with the application and improvement of analytical techniques. However, despite more than 25 years of intensive research and the application of a wide variety of techniques [39], the exact nature of these SAMs is still under debate [40]. In this subsection, an overview of the SAM structure will be given by a bottom-up approach. First, the geometry of the gold substrate will be discussed.

Gold is inert towards corrosion or oxidation [41], has a high sulphur affinity [31], it is not toxic to cells [29] and can be studied with several experimental techniques [27]. Bulk gold atoms arrange in a face-centred cubic (fcc) lattice. This is one of the two closed-packed structures with a coordination number of twelve, the other being the hexagonal close-packed polytype (hcp) [42], as depicted in Figure 1.8a. In Au(111) the brackets

denote the structure of the surface. The (111) Miller indices are allocated to a crystal cut by a plane orthogonal to the sum of the three lattice vectors.



(a) Hcp and fcc close-packed polytypes. Figure taken from ref. [42].

(b) STM topograph of the Au(111) herringbone reconstruction. Ridges appear bright. Figure taken from ref. [43].

Figure 1.8

The Au(111) orientation provides the lowest energy surface [39, 43]. Nevertheless, a bare Au(111) surface rearranges to lower the surface free energy. The reconstructed surface consists of alternating fcc and hcp domains which are separated by elevated ridges, as shown in Figure 1.8b [43, 44]. The domain sizes range from 50 Å to 150 Å but hcp regions consistently have a smaller width than fcc regions. The domain boundaries can be seen to align with the (121) lattice vector. However, due to the threefold lattice symmetry, domains and boundaries can be rotated 120°, so that equivalent patterns in three directions coexist. At the rotational edges, where boundaries intersect, atoms are raised above the surface plane. The atomic corrugation was identified both on bulk single crystals and thin films.

The position of the adsorption site of the alkanethiol SAM on a Au(111) surface and the chemical state of the head group are still unresolved [29, 40]. Experimental and theoretical papers point towards tetrahedral [30, 45] or octahedral holes [46, 47], bridge sites [48, 49] or on top positions [50, 51]. In addition, several groups observed the coexistence of different SAM bonding configurations [52, 53, 54, 55, 56]. Thiolate [47, 57, 58, 59] and disulphide [53, 55] formation at the interface was proposed first, but it is now generally accepted that the chemisorbed species is a thiolate [50, 52, 60, 61]. Diffraction [28, 35, 62], AFM [63] and STM [64] studies showed a hexagonal symmetry with a sulphur-sulphur spacing of 5.0 Å. A $(\sqrt{3} \times \sqrt{3})R30^\circ$ ordering was proposed, as shown in Figure 1.9. At saturation, the surface Au:S ratio equals 3:1 if a perfect monolayer is formed.

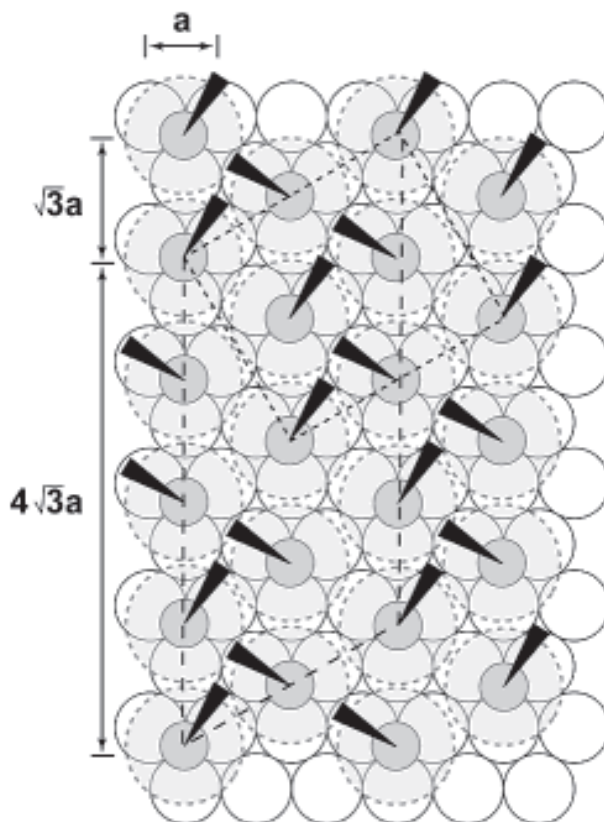


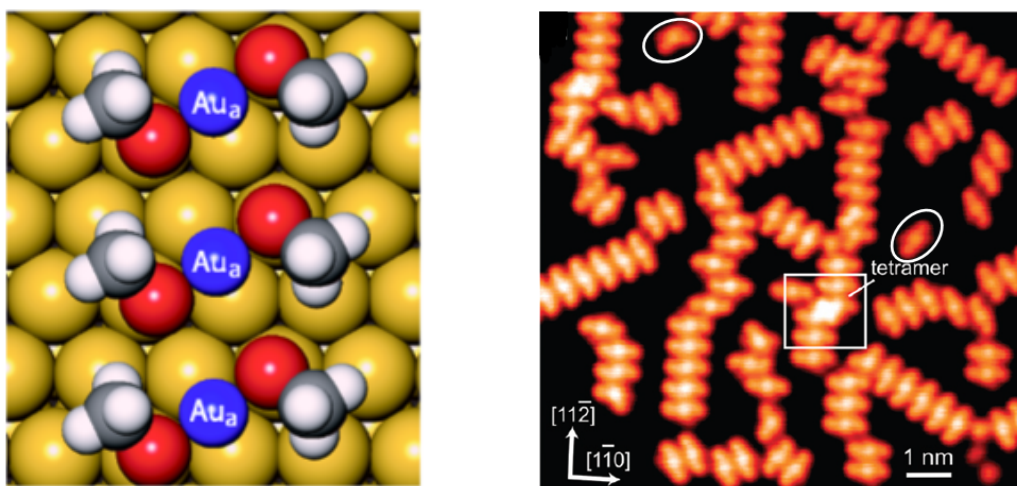
Figure 1.9: The arrangement of alkanethiols on Au(111) with white, grey and black Au, S atoms and alkanechains respectively. Figure taken from ref. [29].

As mentioned in the introduction, the chains tilt to maximise the van der Waals interactions by establishing the perfect interchain distance [52, 59]. This results in the formation of domains with a uniform tilt direction [40]. The tilt angle is defined as the angle between the surface normal and the alkanethiol backbone. Average tilt angles varying from 25° [27, 35] over 32° [62, 65] to 40° [26] were measured. In general, the tilt angle is mostly assumed to be around 30° [28, 66]. However, the tilt angles and orientations are temperature and chainlength dependent [65]. The diffraction studies of Camillone et al. [62] deduced a 45° twist angle, indicating that half of the backbones would be rotated 90° around their molecular axis as compared to the other half.

In 2006 an alternative model was proposed in which two thiolate molecules are bound to a gold adatom forming a staple motif RS-Au-SR [61]. The gold adatoms would originate from the surface reconstruction, from step edges or from one-atom deep pinholes and terraces in the gold surface [40, 67]. The position of the adatom was elucidated by means of DFT [61, 67, 68]. The results showed that the adatom is placed most likely on a bridge site, as demonstrated in Figure 1.10a. The head group binds to both the adatom and a surface gold atom [67]. The atop bond length of 2.49 \AA corresponds well to experimental

observations [50, 51].

The adatom model was first recognised on STM images of short-chain monolayers [61]. At low SAM coverages, methylthiolate staples cluster and form rows parallel to the $(11\bar{2})$ direction [40, 61, 67], as shown in Figure 1.10b. However, there are three different $(11\bar{2})$ directions due to the threefold symmetry of a Au(111) substrate, thus short rows of staples pointing in three different directions are observed. A row is stabilised by the ionic interaction between the positive adatoms and negative sulphur head groups. In order to avoid steric repulsion, all molecules in the stripes have the same configuration. Bright white spots appear on the STM image when two rows meet at their ends, as indicated by the white square in Figure 1.10b. Isolated cis and trans isomers can further be recognised, as indicated by the white ellipses in Figure 1.10b.



(a) Structure for an adatom model obtained by DFT with Au_a the adatom. Figure taken from ref. [61]. (b) STM images of a methylthiolate SAM at intermediate coverage. Figure taken from ref. [67].

Figure 1.10

At higher coverages, the rows are forced to align more closely and striped domains are formed. Various inter-row spacings coexist, but in general the rows are more closely spaced at higher coverages [40]. At the saturation coverage, the rows become staggered to reduce the compression of the negatively charged sulphurs and a (3×4) lattice is formed, as shown in Figure 1.11.

Up to now, only short-chain monolayers have been discussed. The experimental evidence for a long-chain alkanethiol model involving Au-adatoms is limited. STM images do not display the adatoms any more, because they are hidden beneath the backbones. A possible model will be presented that resolves the Au-adatom-dithiolate configuration, but this has not been proved yet [40].

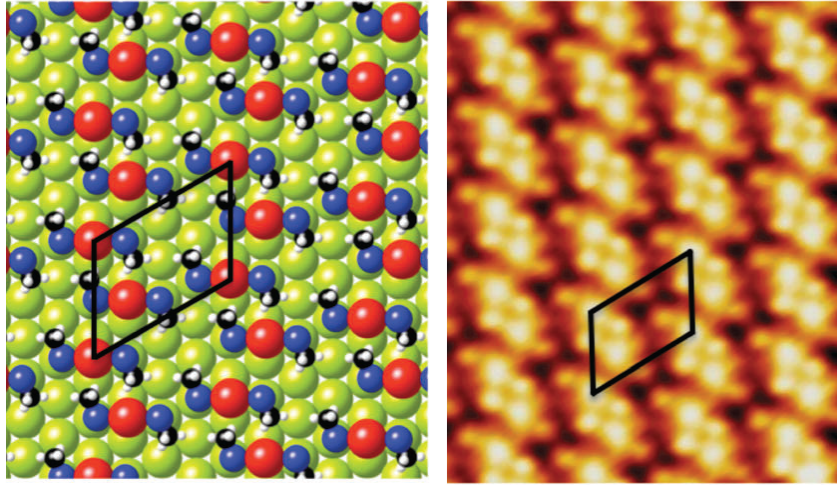


Figure 1.11: STM image and structural model of a methylthiol SAM at saturation coverage. Figure taken from ref. [40].

Starting from butanethiol monolayers, optimisation of the backbone vdW interactions would result in the translation of half of the rows along their backbone, accompanied by a cis-trans isomerisation, as shown in Figure 1.12. In this way a more regular interchain distance is achieved. The model of Guo et al. is not consistent with a $(\sqrt{3} \times \sqrt{3})R30^\circ$ structure, but with a $(3 \times 2\sqrt{3})$ -rect. phase. They argue that both phases cannot be distinguished by diffraction experiments.

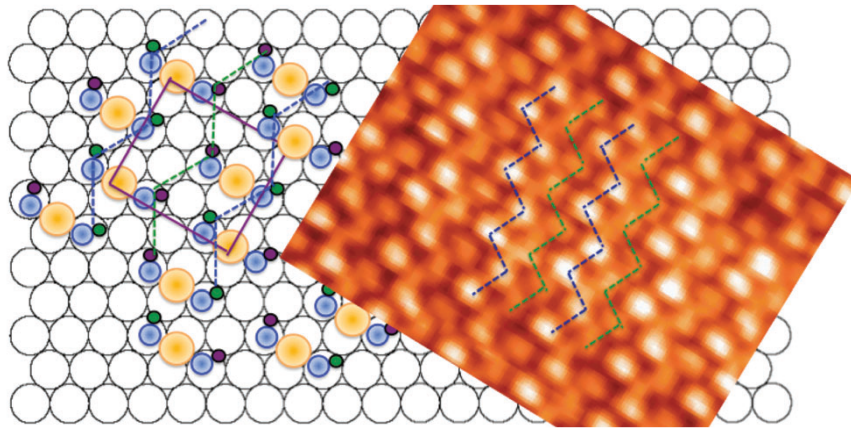


Figure 1.12: STM image and structural model of an octanethiol SAM. Figure taken from ref. [40].

1.4.3 Thermal stability of the SAM

The thermal stability of SAM conformation is very important for the area-selective deposition technique. As discussed above, the ALD process is only successful in a certain temperature window. However, at higher temperatures, typically starting from 400 K, the disorder in the SAM might diminish its blocking ability. Varying tilt and twist angles and gauche dihedrals in the alkane backbones are observed due to the thermal motion of the chains [28]. A second indication of disorder is the randomisation of the tilt direction. Each alkanethiol molecule is surrounded by six other alkanethiol molecules in a perfect monolayer. A tilt in the direction of a neighbouring molecule is called nearest-neighbour tilt (NN). A next-nearest neighbour tilt (NNN) denotes a tilt direction in between the six surrounding alkanethiol molecules.

An united-atom (UA) molecular dynamics (MD) study suggested a continuous phase transition between 250 K and 500 K [69]. The headgroup positions were fixed by modifying the van der Waals radii, so that the gold substrate could be omitted. An average NN tilt direction was observed at 250 K with gauche defects only at the surface of the SAM. Upon increasing the temperature to 300 K, some chains preferred to tilt in the NNN direction and the average tilt angle decreased. At 500 K, the SAM was untilted and disordered with gauche defects present throughout the hydrocarbon backbones and no preferential tilt direction. The study later was repeated using an all-atom force field, which generally performs better than an UA model [70]. Similar conclusions were drawn, except for the NNN tilt direction at 200 K.

On the other hand, a melting transition was clearly identified by UA MD simulations with unrestrained sulphur and gold atoms [71]. Around 400 K, the gauche fraction suddenly rose with gauche defects in the bulk of the monolayer, the tilt angles varied significantly and the tilt direction was randomised. Remarkably, the MD study with position restraints on the sulphur headgroups reported a continuous transition towards a disordered SAM [69], which implies that headgroup positional freedom is essential to observe a melting transition. Indeed, the unrestrained study observed 5-7 dislocation pairs in the melt. In a 5-7 dislocation pair, the headgroups deviate from their six-coordinated positions resulting in five and seven neighbour states. At 300 K, some coordinational modifications are already present. Upon raising the temperature, the density of dislocation pairs increases and four- and eight-coordinated headgroups arise. This enables a greater conformational freedom of the alkanethiol molecules resulting in a discrete phase transition.

The transition from a NN to NNN tilt direction was reported by several experimental groups at temperatures between 300 K and 350 K [71]. Phase diagrams have been made to indicate the chain orientation at certain pressures and temperatures [72]. Melting transition temperatures of 373 K and more were measured [39, 73]. However, SAM stability studies revealed the desorption of dodecanesulphonates after annealing a dodecanethiol SAM at 373 K for 10 h in aerobic conditions [74]. Temperature programmed desorption (TPD) studies of a hexadecanethiol monolayer on Au(111) performed in vacuum substantiated a minimum desorption temperature of 500 K [58], although lower temperatures, equal to 450

K, were also reported [39, 73]. The desorption temperature depends on the chain length of the SAM and the quality of the monolayer [65, 70, 71]. In vacuum, disulphide and thiolate desorption products are formed [75].

1.4.4 Defects

Even at low temperatures the structure of the SAM is not ideal. As all gold substrates are polycrystalline, grain boundaries are present [29, 76]. Terraces separated by step edges, one-atom deep pits or gold vacancy islands are common [54, 62]. Moreover, they are uniformly distributed over the surface. These intrinsic defects are reflected in the SAM, as shown in Figure 1.13.

The cleanliness or chemical purity of the substrate is very important for the performance. The amount of extrinsic defects depends on the experimental conditions. Fortunately, the sulphur affinity for gold is high, so that negligible amounts of impurities were reported by several experimental groups [27, 31, 52].

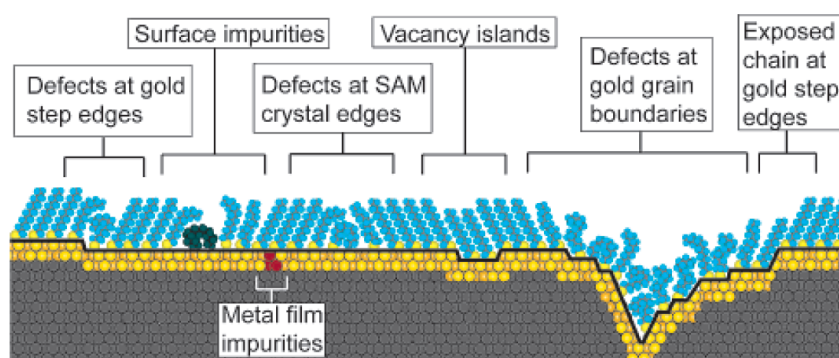


Figure 1.13: Schematic representation of the various defects in a monolayer, taken from ref. [29].

During the self-assembly process, the herringbone reconstruction of the Au(111) surface is altered [77] and depressions of monoatomic depth are etched in the gold substrate [78, 79]. Schönenberger et al. [80] clarified that the depressions are equally covered by a dense monolayer. Domains, characterised by an uniform tilt orientation, are formed in the SAM in register with the substrate structure [81]. Domain sizes range from 5 nm to 15 nm and more [35, 65]. They are delineated by straight rotational or antiphase boundaries and stacking faults [79, 82]. Line defects are commonly observed at the domain boundaries after annealing [74, 76]. On the other hand, the amount of pinholes was found to be negligible [31, 76].

1.5 Atomic diffusion in SAMs

The penetration of atoms in a SAM has been tested experimentally and theoretically for various elements [83]. Several groups examined the vapour deposition of gold atoms on SAMs [84]. A continuous diffusion leads to smooth gold layers at the Au-S interface without altering the SAM structure [85]. At the interface, islands of monoatomic height are assembled [86]. Once the clusters coalesce, a network is made and a second layer starts to grow [85]. The gold atoms only cluster on top of the SAM at low temperatures or high vapour pressures [87]. By exploring the influence of the end group, Zhu et al. [88] argued that static defects cannot explain the penetration. Moreover, the random distribution of the islands at the interface cannot be correlated to substrate defects [86]. Nevertheless, the exact mechanism for diffusion and the adatom mobility at the interface are still under debate.

The gold atom penetration through dodecanethiol monolayers on Au(111) was theoretically modelled by molecular dynamics simulations with the UFF force field [89]. No diffusion was observed. However, as the gold-alkanethiol binding energies predicted by the UFF force field were ten times lower than those calculated by DFT, the Au-C and Au-H van der Waals interactions were scaled by a factor of ten. This resulted in exhaustive penetration at 300 K, but not at 50 K, in agreement with experiments. Alkis et al. justify the force field modification by stating that the UFF force field was not parametrised for this problem.

Hooper et al. [90] investigated the diffusion of aluminium atoms through a hexadecanethiol monolayer on Au(111) by multiple spectroscopic techniques. Although there were no indications for an interaction between the Al atoms and the alkane chains, the spectra indicated the presence of Al atoms at the gold-sulphur interface, as shown in Figure 1.14. A uniform aluminium layer was deposited on the substrate without significantly altering the SAM conformation. After the formation of an one-atom-thick layer at the Au-SAM interface, the penetration stopped and aluminium started to accumulate on top of the blocking layer in a cluster-wise manner. The authors suggest that small, concerted movements of the alkanethiols introduces diffusion channels in the SAM. A reaction of the adatoms with sulphur headgroups at the interface would obstruct the dynamic hopping mechanism leading to overlayer formation. In a later publication, the observation of filaments at static defects is described [91]. Nevertheless, lateral headgroup fluctuations were still presented as the main reason for penetration.

Dai et al. [92] questioned the dynamic hopping mechanism, because the transient diffusion channels would be incompatible with the strong van der Waals interactions in long-chain alkanethiol molecules. They calculated that closely packed, defect-free monolayers intrinsically incorporate channels through which small metal atoms can diffuse. The critical diameter for penetration would be approximately 3 Å, which agrees with experimental data. A 25° tilt angle, covalent radii and a cylindric approximation were used. Although this model is simple and the regularly distributed channels can explain the adlayer uniformity, more research is needed to test its validity. In particular, the use of covalent radii instead

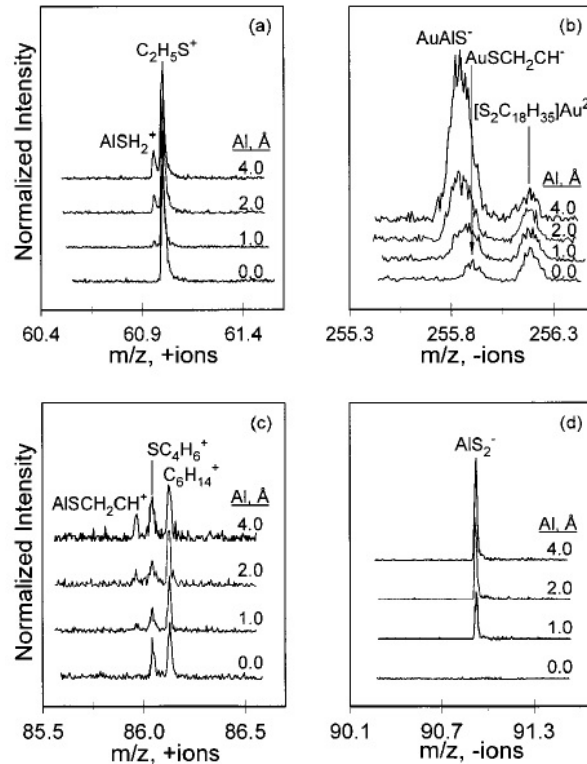


Figure 1.14: Mass spectra indicating the presence of aluminium atoms at the interface. Figure taken from ref. [90].

of van der Waals radii is questionable.

1.6 Area-selective deposition

1.6.1 Introduction

The use of SAMs for the purpose of AS-ALD was investigated by several groups [23, 93, 94]. The potential of the technique was highlighted by the experiments of Dong et al. [25]. Figure 1.15 illustrates a false-colour scanning electron microscopy (SEM) image and line-scanning energy-dispersive X-ray spectroscopy (EDS) scan of zinc oxide coated nanopillars and stripe arrays. The horizontal surfaces of Si structures were covered by a gold film and passivated with dodecanethiol molecules. The nanorods were then exposed to diethylzinc and water pulses, whereupon the vertical surfaces were covered by a uniform zinc oxide layer of 30 nm thickness. The presence of ZnO on horizontal surfaces was limited to minute amounts. Removal of the gold layer eliminated these horizontally deposited particles.

As demonstrated by Dong et al. [25], AS-ALD is an accurate method to replicate a substrate pattern. This is achieved by the selective adsorption of the SAM. For example, alkanethiol molecules adsorb on metals, but not on dielectric materials. A metal-dielectric

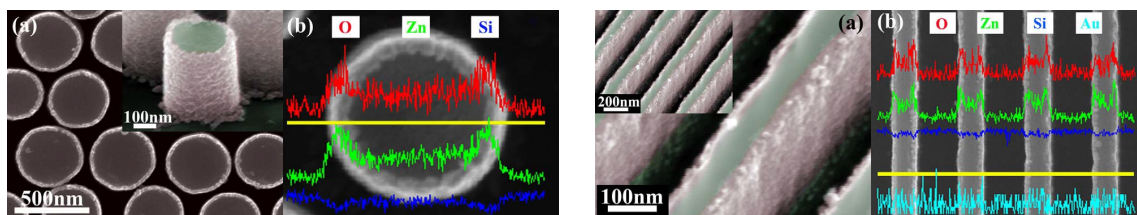


Figure 1.15: False-colour SEM images (a) and EDS scans (b) of selectively coated nanorods and stripes. Figure taken from ref. [25].

pattern can thus be replicated on an atomic scale by selectively inhibiting metal oxide deposition on the SAM passivated metal [23].

The alkanethiol molecules can be solution or vapour-deposited. Nevertheless, four days of solution deposition was needed in order to delay ZnO ALD [95]. Long SAM chemisorption periods are necessary to obtain a dense, efficient passivation layer [9]. On the other hand, very short formation times, thirty seconds or less, suffice to yield a good inhibition layer by vapour loading due to the faster kinetics [96]. Moreover, the SAM can be deposited in the ALD reactor which saves time and reduces the amount of impurities in the film [94]. Finally, the coverage of porous and three-dimensional structures is facilitated by a vapour process [22].

Alternatively, a patterned monolayer can be deposited by microcontact printing [97]. Microcontact printing is an inexpensive and efficient method to deposit a monolayer on unpatterned substrates [24].

1.6.2 Impact of the ALD process in area-selective deposition

Avila et al. [95] investigated how the blocking properties of a dodecanethiol SAM deposited on Au(111) depend on the ALD precursor. The nucleation of several metal oxides was monitored in situ by quartz crystal microbalance studies. A strong dependence of the precursor was observed for the ALD on the SAM, which is currently not yet understood. Figure 1.16 shows the growth curves of the TMA, tetrakis(dimethylamido)titanium (TDMATi), tetrakis(dimethylamido)tin (TDMASn) and diethylzinc (DEZ) / water processes. No growth inhibition is observed for the aluminium oxide deposition, as the TMA precursor is proposed to replace the monolayer. Despite having the same ligands, titanium dioxide growth is more inhibited than the tin oxide growth. The thickness of the zinc oxide film initially increased, after which it evolved to a constant value. The inhibition ability is explained by DEZ incorporation in the SAM. DEZ would align with the alkanethiols and hereby increase the resistance towards further DEZ adsorption. Longer experiments revealed depreciation of the blocking ability after the hundredth cycle, with a continuous growth curve approximately starting from cycle number 150. Interestingly, the ZnO would grow on top of the SAM according to Avila et al. [95] and not replace it as is the case for TMA.

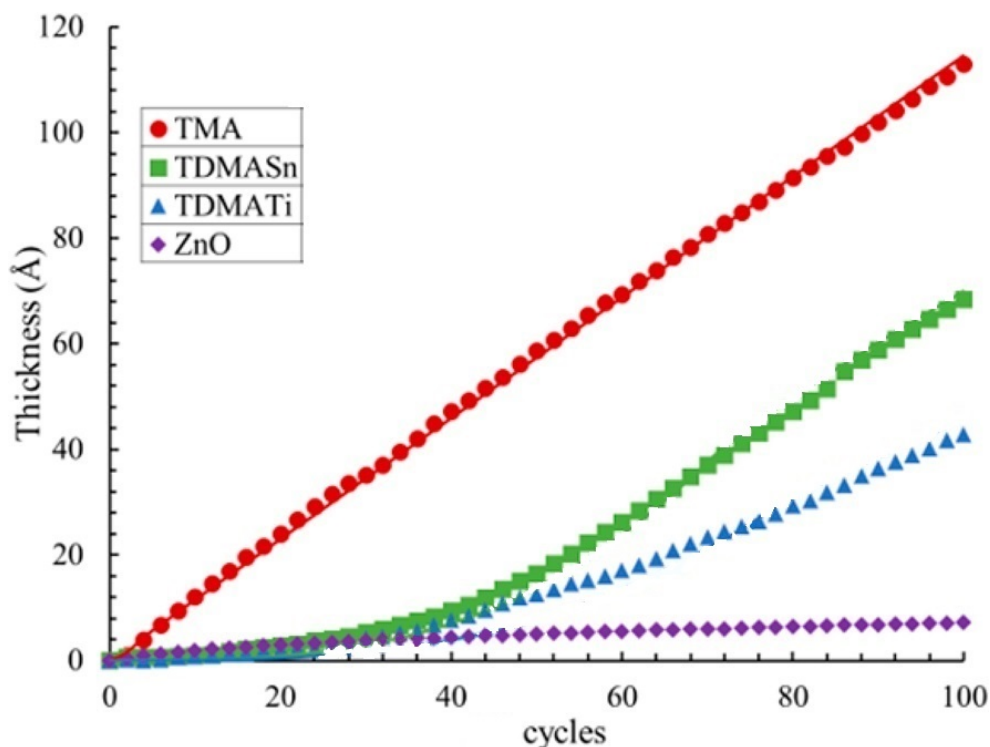


Figure 1.16: Growth curves of various ALD processes on dodecanethiol SAMs at 398 K. Figure adapted from ref. [95].

The hypothesis that the TMA precursor molecules replace the dodecanethiol SAM is contradicted by Preiner et al. [76]. They applied the aluminium oxide ALD technique to image defects in the monolayer. A defective SAM was deliberately created and exposed to a limited number of ALD cycles. The deposition did not introduce additional defects. SEM images revealed a high aluminium oxide density at the defective sites, whereas only a very little amount of aluminium covered the SAM. Hence, the defects act as nucleation sites for aluminium oxide film growth. DFT calculations confirmed that TMA does not react with the methyl end groups of the SAMs [13]. Only after wetting the SAM, an aluminium oxide layer can be deposited on top of the hydrophobic monolayer [98].

1.6.3 Enhanced selectivity

The group of professor Bent at Stanford University has published several papers on AS-ALD [99, 100, 101]. They proposed some interesting procedures to enhance the selectivity, which demonstrates the potential of area-selective deposition. In a first publication, octadecylphosphonic acid was deposited on a patterned Cu/SiO₂ substrate [23]. Whereas dense monolayers were formed on the copper, no adsorption was observed on the silicium oxide. Treatment with TMA and water precursors resulted in area-selective deposition up to 6 nm. However, combining the ALD process with an etching step significantly improved the

realisable film thickness. A sonication in acetic acid removed the SAM together with the diffused aluminium atoms, but did not damage the film on silicium oxide. This method successfully produced high-quality aluminium oxide patterns of 60 nm thickness.

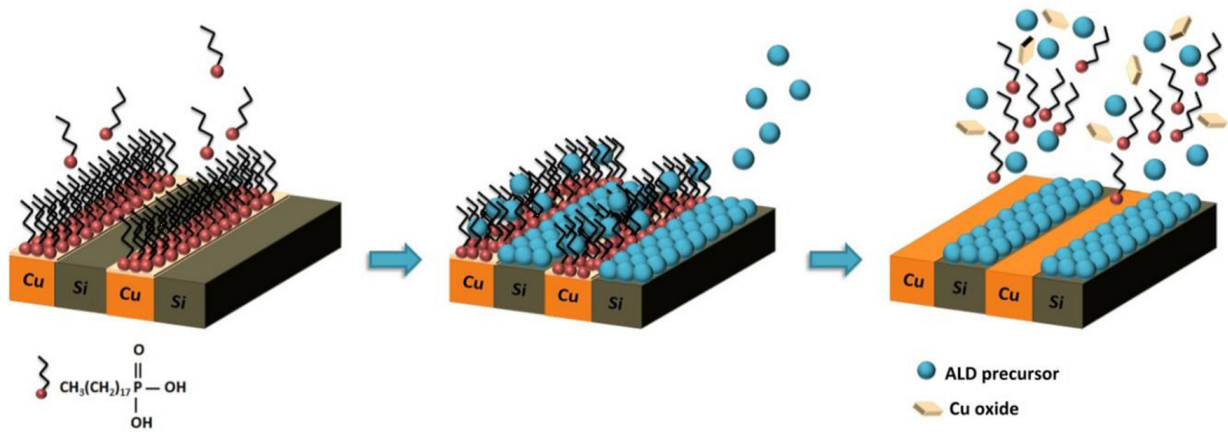


Figure 1.17: The selective deposition and removal of ODPA SAMs. Figure taken from ref. [23].

A second paper introduces the sequential regeneration of SAMs as a mean to achieve longer inhibition of the ALD process [96]. A dodecanethiol monolayer was vapour-deposited on a mixed *Cu/SiO₂* surface, followed by ZnO ALD. Only after 200 cycles, zinc was detected in the passivated areas. Experiments indicated the degradation and desorption of the SAM. Redeposition of the SAM restored the inhibition properties and did not alter the film on the dielectric. By applying this strategy every 150 cycles, a selectively deposited film of more than 100 nm could be obtained.

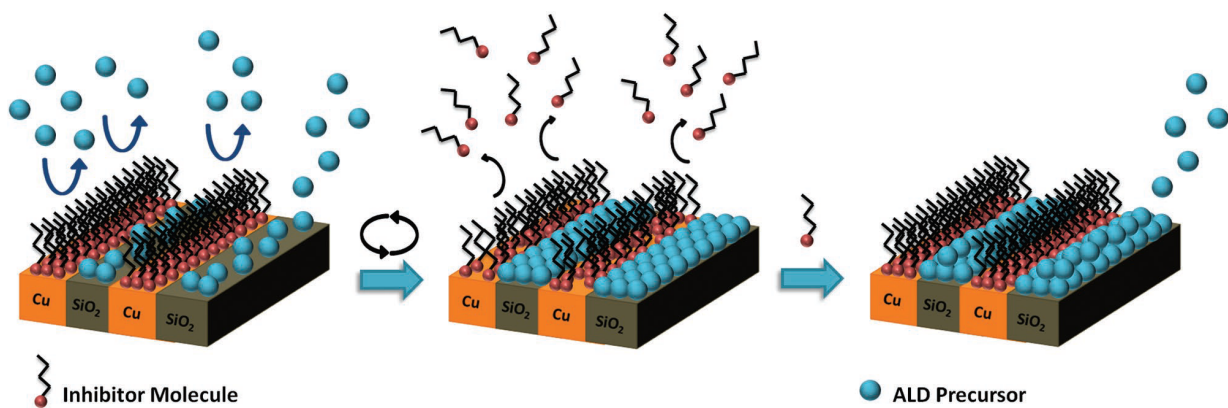


Figure 1.18: Schematic of the sequential regeneration technique. Figure taken from ref. [96].

1.7 Problem statement

The potential of area-selective deposition has been experimentally demonstrated for several patterned substrates and metal oxide depositions [22, 25, 94]. However, SAMs are only able to delay or inhibit the growth for a limited number of ALD cycles [96]. Insights into the nucleation mechanisms of ALD precursors on SAM passivated surfaces are lacking [95]. Since the formation of dense monolayers is required to inhibit the ALD process [24, 95], several research groups point towards defects in the monolayer as nucleation sites for thin film precursor molecules [93, 96]. The application of ALD was even suggested as a sensitive technique to visualise SAM defects [24, 76]. Nevertheless, the role of defects in reducing the passivating properties of the SAM has not been investigated on an atomic scale yet.

1.8 Objectives

The goal of this master thesis is to shed more light on the factors controlling the ability of the SAM layer to inhibit the ALD precursor nucleation processes by means of molecular dynamic simulations. This study will contribute to a better understanding of the interactions between a SAM and ALD precursor molecules. The dynamics of a dodecanethiol SAM on a flat Au(111) substrate and TMA precursor molecules were examined. Molecular dynamics simulations were performed in *Gromacs* using the OPLS force field.

First, the thermal stability of the SAM conformation will be investigated, because a reduction of the SAM inhibition properties with increasing temperature was experimentally observed [95]. Since OPLS is not parametrised for Au(111) substrates, new parameters will be added to the force field. The diffusion of gold atoms in the SAM will be examined next in order to gain insights in possible penetration processes. More specifically, the presence of intrinsic diffusion channels in a perfect monolayer, as hypothesised by Dai et al. [92], will be tested. Finally, the interaction of TMA with the SAM layer will be investigated by considering both a perfect monolayer and a monolayer with different coverage defects. In order to perform the simulations, new force field parameters will be derived by using reference data obtained with DFT. Several line and point defects will be introduced in order to unravel the role of defects in the TMA diffusion process.

1.9 Outline

The methods used in this thesis are explained in the second chapter. The methodology and the settings that were used to obtain the results are presented in the third chapter. The fourth chapter includes a description and discussion of the results. A summary of the results and outlook can be found in the last chapter. The Appendix includes additional figures, parameter files and scripts.

Chapter 2

Methods

This chapter will elaborate on the methods used in this thesis. The theory of molecular dynamics (MD) will be explained [102, 103, 104] and an overview of the different programs used to generate and process the results will be presented.

2.1 Molecular dynamics

In classical MD with an MM force field, as used in this thesis, the time evolution of a system is predicted based on the laws of classical mechanics. The dynamics is thus deduced from the nuclear coordinates, while neglecting the electronic motion. This is partly justified by the Born-Oppenheimer principle, which states that electrons readily adapt to changes in the nuclear conformation due to the difference in mass between nucleons and electrons. However, the lack of typical quantum phenomena in the energy and trajectory calculations induces errors. Tunnelling effects are not incorporated. Hydrogen bonds and polarisation cannot be described. Since the electrons are not considered, chemical reactions cannot be modelled. More specifically, the precursor diffusion through the monolayer can be investigated, but the subsequent surface reaction not. Nevertheless, MD is a unique technique to evaluate the time evolution of very large systems in reasonable computational times.

2.1.1 The simulation method

Newton's second law states that force equals mass times acceleration, where the force and acceleration are vectors in three-dimensional space (Eq. 2.1) [105]. Atomic interactions are described by position dependent forces. Since all particles continuously change their position, the force exerted on a particle at a certain point in space remains not constant. This couples the trajectories of all atoms in the system. Hence, the time evolution of one particle cannot be evaluated without considering the other particles too.

$$\mathbf{F} = m\mathbf{a} = m\frac{d^2\mathbf{r}}{dt^2} \quad (2.1)$$

This complex problem is handled in the finite difference method by making several approximations. First, the simulation time is divided in equally small steps, after which the positions and velocities are evaluated. During the time interval Δt , the forces, and thus the accelerations too, are kept constant. Second, the force exerted on a particle is approximated as a sum of the forces resulting from each interaction individually. The complex interplay between all particles is thus reduced to a discrete sum of forces.

The finite difference method encompasses multiple algorithms to calculate trajectories. A popular method was named after Verlet [106]. The Verlet algorithm can be derived by approximating the time dependent positions and velocities with a Taylor expansion.

$$\begin{aligned}\mathbf{r}(t + \Delta t) &= \mathbf{r}(t) + \Delta t \frac{d\mathbf{r}(t)}{dt} + \frac{\Delta t^2}{2} \frac{d^2\mathbf{r}(t)}{dt^2} + \frac{\Delta t^3}{6} \frac{d^3\mathbf{r}(t)}{dt^3} + \dots \\ &= \mathbf{r}(t) + \Delta t \mathbf{v}(t) + \frac{\Delta t^2}{2} \mathbf{a}(t) + \frac{\Delta t^3}{6} \frac{d^3\mathbf{r}(t)}{dt^3} + \dots\end{aligned}\quad (2.2)$$

$$\mathbf{v}(t + \Delta t) = \mathbf{v}(t) + \Delta t \frac{d\mathbf{v}(t)}{dt} + \frac{\Delta t^2}{2} \frac{d^2\mathbf{v}(t)}{dt^2} + \frac{\Delta t^3}{6} \frac{d^3\mathbf{v}(t)}{dt^3} + \dots\quad (2.3)$$

If $\mathbf{r}(t - \Delta t)$ is expanded too and summed with equation (Eq. 2.2), the position at time $t + \Delta t$ can be written as a function of the previous positions and the acceleration (Eq. 2.5).

$$\mathbf{r}(t - \Delta t) = \mathbf{r}(t) - \Delta t \mathbf{v}(t) + \frac{\Delta t^2}{2} \mathbf{a}(t) + \dots\quad (2.4)$$

$$\mathbf{r}(t + \Delta t) = 2\mathbf{r}(t) - \mathbf{r}(t - \Delta t) + \Delta t^2 \mathbf{a}(t)\quad (2.5)$$

Although the expression for $\mathbf{r}(t + \Delta t)$ given by the Verlet algorithm is simple, it does not include the velocity and two sets of initial conditions are required. The former remark is more important. Many physical properties, such as the momenta and kinetic energies of the particles or the temperature of the system, depend on the velocities. Therefore, an alternative algorithm, the leap-frog algorithm, is used in *Gromacs* [107]. This method updates the velocities halfway the time step and subsequently calculates the positions, where formula (Eq. 2.6) results from subtracting the Taylor expansions.

$$\begin{aligned}\mathbf{r}(t + \frac{\Delta t}{2} + \frac{\Delta t}{2}) &= \mathbf{r}(t + \frac{\Delta t}{2}) + \frac{\Delta t}{2} \mathbf{v}(t + \frac{\Delta t}{2}) + \frac{1}{2} \left(\frac{\Delta t}{2}\right)^2 \mathbf{a}(t + \frac{\Delta t}{2}) + \dots \\ \mathbf{r}(t + \frac{\Delta t}{2} - \frac{\Delta t}{2}) &= \mathbf{r}(t + \frac{\Delta t}{2}) - \frac{\Delta t}{2} \mathbf{v}(t + \frac{\Delta t}{2}) + \frac{1}{2} \left(\frac{\Delta t}{2}\right)^2 \mathbf{a}(t + \frac{\Delta t}{2}) + \dots \\ \mathbf{r}(t + \Delta t) &= \mathbf{r}(t) + \mathbf{v}(t + \frac{\Delta t}{2})\Delta t\end{aligned}\quad (2.6)$$

$$\mathbf{v}(t + \frac{\Delta t}{2}) = \mathbf{v}(t - \frac{\Delta t}{2}) + \mathbf{a}(t)\Delta t\quad (2.7)$$

2.2 Force field

In order to calculate the consecutive particle positions with the leap-frog algorithm (Eq. 2.6), the acceleration a must be known or Newton's equation of motion (Eq. 2.1) must be solved. A force field is a description of the equations used to calculate the forces and their parameters for different elements. As the force equals minus the gradient of the potential energy (Eq. 2.8), a force field is often expressed in terms of energy contributions. Several contributions to the potential energy can be distinguished, which are generally grouped in bonded and non-bonded interactions. The bonded interactions comprise bond, angle and dihedral terms. The non-bonded terms include the electrostatic and van der Waals components.

$$F = -\nabla V \quad (2.8)$$

Terms from several forcefields cannot be combined, because the functional forms may differ. Moreover, a forcefield is parametrised to perform in a way that is overall realistic. Since the values adopted by the constants are correlated and different contributions balance each other, individual components cannot be separately interpreted. The molecules and properties used in the parametrisation process outline the preferential applications. For some force fields, the transferability might be limited.

In this work, the OPLS, Optimised Potentials for Liquid Simulations, force field was used. The OPLS force field was chosen for its precise parametrisation and broad applicability. The all-atom description was preferred over an united-atom model, since more accurate results are obtained by including the hydrogen atoms [108]. In this section, the different components of a force field will be discussed and the functions used to describe the interactions in the OPLS force field will be provided.

2.2.1 Bond stretching and angle bending contributions

First the bonded interactions will be addressed. Figure 2.1 shows a typical Morse curve for a bond stretching potential, where the potential energy $v(l)$ is plotted as a function of the interatomic distance l [109]. The equilibrium distance l_0 between two particles corresponds to the minimal energy conformation. A very steep energy increase at shorter bond lengths and a horizontal asymptote at longer separations can be discerned. The functional form of the Morse potential of two particles with masses m_1 and m_2 is given in Equation (Eq. 2.9) with D_e the depth of the minimum, μ the reduced mass, ν the frequency of the vibration and k the system specific force constant.

$$\begin{aligned} V &= D_e(1 - \exp(-2\pi\nu\sqrt{\mu/2D_e}(l - l_0)))^2 \\ \mu &= \frac{m_1m_2}{m_1 + m_2} \quad \nu = \frac{1}{2\pi}\sqrt{\frac{k}{\mu}} \end{aligned} \quad (2.9)$$

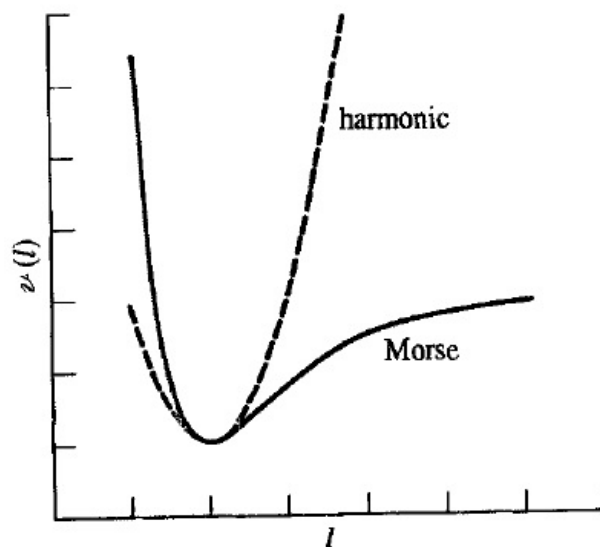


Figure 2.1: Morse curve and harmonic approximation. Figure taken from ref. [102].

Nevertheless, in OPLS the bond stretching is modelled by a simpler functional form, namely by a harmonic potential (Eq. 2.10). This requires less parametrisation and computational effort than a Morse potential. The harmonic approximation is quite accurate at small vibrational amplitudes or close to the equilibrium distance. Errors occur at short interatomic distances, where the repulsion is not strong enough, and at greater bond lengths, with an exaggerated potential increase.

$$V = \frac{k}{2}(l - l_0)^2 \quad (2.10)$$

Starting from triatomic molecules, an angle between two consecutive bonds can be defined with an equilibrium value depending on the hybridisation of the central atom. For example, the substituents of an sp^3 hybridised carbon are optimally 109.5° apart, whereas an sp^2 hybridisation leads to angles equal to 120° . The optimum is determined by a minimal repulsion between the electron clouds of the bonds and lone pairs, so any increase or decrease in angle is unfavourable. The angle bending term in the OPLS force field is also implemented as a harmonic function with a parametrised force constant k .

2.2.2 Dihedral contributions

The dihedral contributions to the force field incorporate the effect of torsion. The gauche and trans conformations of a butane molecule are shown in Figure 2.2. The torsional angle is defined as the angle between the first and the third bond vectors.

The dihedral energy term is mostly described by a cosine series expansion (Eq. 2.11). This approximation is called a Ryckaert-Bellemans potential. The angle ϕ is then defined

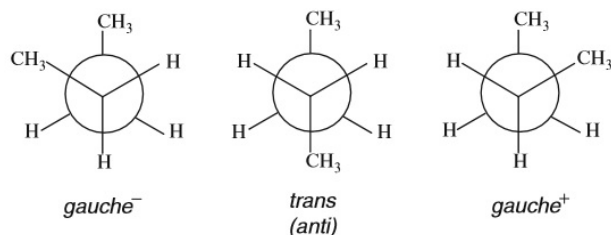


Figure 2.2: Newman projections of n-butane. Figure taken from ref. [110].

between the plane of the first and the second bonds and the plane characterised by the second and third bond vectors.

$$V(\phi) = \sum_{n=0}^5 C_n (\cos(\phi))^n \quad (2.11)$$

Nevertheless, an equivalent form of the dihedral potential (Eq. 2.12) is formulated in the OPLS paper [108]. The three terms in the Fourier series refer to three minima.

$$V(\psi) = \frac{V_1}{2}[1 + \cos(\psi)] + \frac{V_2}{2}[1 - \cos(2\psi)] + \frac{V_3}{2}[1 + \cos(3\psi)] \quad (2.12)$$

In *Gromacs*, the latter Fourier series is implemented with an additional fourth term. However, the Ryckaert-Bellemans function is used in calculations to increase the computational efficiency. Although the parameters in both functions can be easily converted, a different angular convention is followed. In the polymer convention used in (Eq. 2.11), $\phi = 0$ denotes a trans dihedral, whereas $\psi = 0$ is cis in the protein convention. In OPLS the 1-4 non-bonded interactions contribute to the dihedral too, whereas these terms are removed in some other force fields.

2.2.3 Improper torsions

Some molecules require an additional bonded term in the force field to achieve a certain conformation. The standard examples are mesomeric molecules, where electrons are delocalised over several atoms. The resonance energy is maximised in a planar arrangement when the p-orbitals of the contributing atoms overlap most. As this particular conformation deviates from the normal geometry and consequently is not expressed in the standard forcefield terms, an improper term is introduced. A first option is to define an improper dihedral. The improper dihedral angles for rings, ring substituents and tetrahedrals are illustrated in Figure 2.3. A second option incorporates a harmonic potential. Either the angle between a bond and a molecular plane is confined, or the perpendicular distance between an atom and a plane is restrained. However, negative side-effects, such as incorrect vibrational frequencies, can be expected [102].

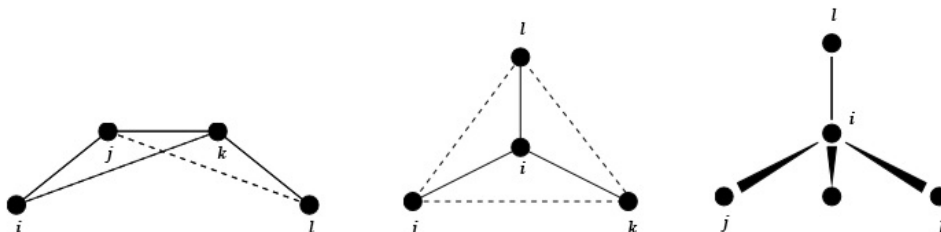


Figure 2.3: Improper dihedrals for rings, ring substituents and tetrahedrals are defined by the angle between the ijk and jkl planes respectively. Figure taken from ref. [104]

The bond stretching, angular and dihedral contributions to the force field express the forces between atoms that are one, two and three bonds apart respectively. The forces between all other atom pairs are included in the non-bonded interactions. Electrostatic interactions are attributed to partially charged particles, whereas van der Waals forces act on all atoms. In the following two subsections, the non-bonded contributions will be addressed.

2.2.4 Electrostatic contribution

Partial atomic charges are adopted if atoms with a different electronegativity are connected. Two particles with the same charge repel each other, whereas opposite charges work attractively, according to Coulomb's law (Eq. 2.13). The magnitude of the potential depends on the interatomic distance r_{ij} with ϵ_0 the vacuum permittivity and q_i, q_j the charge of the first and second atom respectively.

$$V(r_{ij}) = \frac{q_i q_j}{4\pi\epsilon_0 r_{ij}} \quad (2.13)$$

2.2.5 van der Waals contributions

The last potential term introduces the attraction and repulsion between all pairs of atoms that are separated by three bonds or more. Due to the Pauli principle, all short-range interactions are repulsive. At further distances, fluctuations in the electron density of one atom change the electronic distribution of another atom. This leads to a temporary attraction between the instantaneous dipoles. Since both interactions have a quantum-mechanical nature, they cannot be modelled with classical MD. Nevertheless, Lennard-Jones developed a computationally efficient function to approximate the interatomic potential (Eq. 2.14). The 1-4 Lennard-Jones potential is scaled by 0.5 to not interfere with the torsional term.

$$v(r) = 4\epsilon_{ij} \left[\left(\frac{\sigma_{ij}}{r_{ij}} \right)^{12} - \left(\frac{\sigma_{ij}}{r_{ij}} \right)^6 \right] \quad (2.14)$$

The Lennard-Jones expression contains two parameters, being the collision diameter σ and the well depth ϵ . Sigma corresponds to the distance at which the vdW potential is

equal to its asymptotic value. Epsilon defines the potential energy at the minimum. Since a critical point can be located by setting the first derivative equal to zero, the minimum energy separation r_{min} equals $2^{1/6}\sigma$. Although the sixth power for the attractive part is theoretically reasonable, the overlap energy normally decays exponentially [102]. The twelfth power is mathematically convenient in view of the large number of particles, but too steep for hydrocarbons.

Deriving the parameters for all combinations of elements in different chemical states would be a massive work. Hence, one set of parameters is assigned to each atom type and mixing rules were established. In OPLS, the values of epsilon and sigma are determined by geometrically averaging the atom type parameters.

$$\epsilon_{ij} = \sqrt{\epsilon_{ii}\epsilon_{jj}} \quad \sigma_{ij} = \sqrt{\sigma_{ii}\sigma_{jj}} \quad (2.15)$$

2.3 Atom types

The expressions for the forces contain several parameters and equilibrium values. To practically handle the MD calculations, atom types are created. An atom type is a collection of an atomic number, charge and set of parameters allocated to a particle. Various atom types can exist for the same element, depending on its geometry and hybridisation. For example, in OPLS sp , sp^2 and sp^3 hybridised carbons are distinguished. In addition, different constants are assigned to carbon atoms bonded to one, two or three hydrogen atoms. In total, the standard OPLS force field contains 805 different atom types to simulate the dynamics of biomolecules. The *Methodology* chapter will elaborate more on the practical implementation of atom types in the force field.

2.4 Parametrisation

The parametrisation of a force field is a massive and difficult task. A consistent set of parameters needs to be derived that computationally reproduce the experimental properties, preferably in a quantitative way. The van der Waals constants for alkanes in OPLS were determined by fitting the outputs of a series of Monte Carlo simulations to thermodynamic and structural properties of hydrocarbon liquids [111]. Jorgensen et al. specifically focused on reproducing the experimental densities and heat of vaporisation. A charge of 0.06 was assigned to alkane hydrogen atoms. The value of 0.06 was empirically established by Kaminski et al. [111] by simulating liquid hydrocarbons. All other charges were empirically adjusted to resemble experimental systems and to make neutral charge groups. The authors emphasise the importance of transferability in this regard. The bond stretching and angle bending functional forms were copied from the AMBER force field [112], except for the alkane values which were transferred from the CHARMM force field [113]. The adopted parameters were found by analysing vibrational and structural data. Finally, the torsional parameters were adjusted to match the conformational energy profiles calculated by ab-initio methods [108, 114].

The Gold-Protein (GolP) force field extension for OPLS was used in this thesis to account for the Au(111) substrate [115]. GolP was parametrised in order to reproduce the interaction of proteins with Au(111) substrates and gold nanoparticles in water. The Lennard-Jones interaction energies of chemisorbed molecules, including disulfides and thiols, in GolP were parametrised via DFT calculations. The vdW parameters for alkanes were optimised based on experimental desorption energies and Möller-Plesset perturbation theory (MP2) calculations.

2.5 Periodic boundary conditions

The goal of this thesis is to simulate the diffusion through a SAM. However, it is impractical to consider a large monolayer, as computational times will be very long. Periodic boundary conditions (pbc) allow to examine an infinite system from a limited input configuration. All particles are placed in a box. By applying pbc, this box is copied in all directions to cover space. The analogy to a crystal built from the translation of a single unit cell can be made. If a particle leaves the box, it enters an identical image of the box. In order to keep a constant number of particles, an identical atom enters the original box from the opposite site. In this way, bulk properties can be obtained from a limited simulation system. The box's walls further do not artificially repel the molecules. Of course, the size of the box limits the spatial extent of properties and interactions that can be studied.

The implementation of pbc implies that particles inside the box can interact with atoms in image boxes. This is necessary to approximate an infinite system, but significantly increases the complexity of the calculations. The slow decay of the Coulomb term particularly results in a considerable energy contribution from charge-charge interactions across the boxes. The particle mesh Ewald (PME) approximation was specified in this thesis to improve the performance of the calculations of the long-range Coulomb interactions [116].

2.6 Cut-offs

In large systems, the calculation of the non-bonded interactions is computationally demanding, even if PME is applied. The number of non-bonded interactions approximately scales as the number of atoms squared, whereas the number of bonded contributions to the force field increases linearly with the number of atoms. Especially the Coulomb interaction, which scales as r^{-1} must be truncated in order to save time. In *Gromacs*, the minimum-image convention is followed. This means that each atom only interacts with the nearest image of all other atoms in the box. In other words, all forces should not extend beyond half the box size to avoid that particles interact twice with the same atom. At a sufficiently large distance, the force is set equal to zero. Of course, this creates artefacts at the cut-off distance where a sharp transition is made. In order to avoid discontinuities at the cut-off distance, the potential is shifted.

2.7 Thermostats

Traditional molecular dynamics computations considered isolated systems. The total number of particles, the volume and energy were kept constant. This is called an NVE or microcanonical ensemble. In experiments, however, closed systems are treated, which allow for energy exchange with the surroundings. The temperature and pressure in a lab are constant, but the energy and volume of the sample are not. Only for infinite systems, both ensembles are equal. This discrepancy between experimental and theoretical conditions can be solved by applying a thermostat and a barostat. A thermostat reassigns particle velocities to ensure a certain temperature, whereas barostats adjust the system's volume to keep a constant pressure. The latter will not be discussed here, since it was not invoked in this thesis.

The equipartition theorem states that the temperature of a system is related to the kinetic energy of its components (Eq. 2.16) with v_i the root-mean-square speed of particle type i , N the total number of particles in the system and $\sum_i N_i = N$. In the MD algorithms discussed earlier, the kinetic energy continuously changes. Potential and kinetic energy are transposed, while the total energy remains constant. As a consequence, the temperature alters each step. Thermostats guarantee a constant temperature during the simulation.

$$E_{kin} = \sum_i \frac{N_i m_i v_i^2}{2} = \frac{3}{2} N k_B T \quad (2.16)$$

It is straightforward to just scale the velocities by a constant each step [117]. However, this method is rather abrupt. A more gentle method was developed by Berendsen in 1984 [118]. He employed an external heat bath. After each step energy is exchanged between the system and the bath, which remains at the desired temperature. A coupling parameter τ can be fit to smoothen the velocity scaling, as shown in (Eq. 2.17). The larger tau, the less coupling and the smaller the rate of temperature change. Overall, the system's temperature deviations are characterised an exponential decay in time with an asymptote at the intended temperature. Although the dynamics are slowly corrected, proportional to τ , the kinetic energy distribution and related properties can be incorrect, especially for smaller systems. This problem is solved in the velocity rescaling thermostat. It produces a correct distribution by adjusting the kinetic energy with a stochastic term [119].

$$\frac{dT}{dt} = \frac{T_0 - T}{\tau} \quad (2.17)$$

2.8 Energy minimisation methods

In the standard microcanonical MD simulations, the total energy remains constant. Potential energy is transformed into kinetic energy and vice versa, but their sum is not altered. The potential energy of the input structure is minimised before the simulation in order to avoid large particle velocities. There are several algorithms to minimise the energy of an input structure, two of which will be discussed here.

The potential energy of a system is a function of all the coordinates that specify a conformation. A potential energy surface (PES) plots the energy as a function of the internal coordinates. Each conformation denotes a point on the multidimensional PES. At stationary points, the partial derivative of the energy with respect to all coordinates equals zero. Hence, the force equals zero, according to (Eq. 2.8). If all the second derivatives are positive, the equilibrium structure is a minimum. The global minimum is defined as the lowest energy geometry, whereas local minima are higher energetic stable structures. Any change of the nuclear arrangement of a minimum conformation increases the energy. The other stationary points are maxima or saddle points, with all or some negative second derivatives respectively. This implies that the equilibrium point is unstable and that altering the structure can lower the energy.

Various techniques can be used in order to locate a minimum conformation starting from an input structure. The steepest descent and conjugate gradient methods follow the negative of the first derivative at a point on the PES. As previously stated, the negative of the gradient equals the force. The conformation is thus changed according to the 3N-dimensional force acting on the system. However, which step size should be used? In the steepest descent method implemented in *Gromacs*, the initial displacement vector equals 0.01 nm times the force divided by the maximal force component. As long as the energy decreases, the step size is increased. When a conformation moves uphill on the PES, it is rejected and a reduced step size is tried. This process is iterated until a predefined force or number of steps is reached. The steepest descent method was used throughout this work. It is not very efficient, but it is robust and a thorough energy minimisation is not required as a preparation for MD.

An alternative scheme, named conjugate gradient (CG), performs better close to the minimum. Whereas the step direction in the steepest descent method depends only on the gradient, a dependence on the previous direction is added in the CG method. As a result, successive directions on the PES are not orthogonal. In contrast to what the name suggests, successive gradients are still orthogonal. The same step size as in the steepest descent scheme is used in *Gromacs*. The l-bfgs method or limited-memory Broyden-Fletcher-Goldfarb-Shanno quasi-Newtonian minimiser is also available in *Gromacs* [120]. L-bfgs is a second-order method, meaning that a minimum is found by evaluating the gradient and an approximate form of the Hessian. Although it would converge faster as compared to CG, l-bfgs is not parallelised in *Gromacs*. Therefore the conjugate gradient scheme was used for the more accurate energy minimisations.

2.9 Density functional theory

The second computational method that was applied in this thesis is density functional theory. DFT was used for the parametrisation of TMA molecules. Whereas MD is based on classical mechanics, DFT relies on quantum techniques to predict the electronic distribution in molecules. Stationary points on the PES can be accurately located with DFT and the

vibrational frequencies can be determined by a normal mode analysis.

2.9.1 Level of theory

The B3LYP functional [121] and the split-valence def2-TZVP [122] basis set were used. An ultrafine integration grid was requested in order to increase the accuracy. B3LYP is hybrid functional with 20% exact exchange. Def2-TZVP is an abbreviation for default-2-triple zeta valence basis set with polarisation functions. The polarisations functions are 1p for H atoms, 2d 1f for C and 2d 1f for Al with a contracted additional d function. Pairwise dispersion corrections were added by requesting Grimme’s D3 function [123]. Finally, the atomic charges in TMA were calculated with the MK and ChelpG schemes [124, 125]. These methods fit the TMA electrostatic potential to atomic point charges according to a least-square method with Lagrangian multipliers.

2.9.2 Normal mode analysis

DFT was applied to locate the minimum energy conformation of a TMA molecule on the PES. A vibrational analysis was performed to confirm the nature of the structure [126]. In a minimum, the second derivative of the potential with respect to all internal coordinates is positive, as mentioned in the previous section. The partial second derivatives are represented in a matrix, called the Hessian. Diagonalisation of the mass-weighted Hessian results in the eigenvalues and eigenvectors of a TMA molecule. The vibrational normal modes are found by removing the 3 rotational and 3 translational degrees of freedom. The vibrational frequency ν is related to force constant k of a vibration by Equation (Eq. 2.18) with μ the reduced mass. Hence, a negative force constant corresponds to an imaginary frequency.

$$\nu = \frac{1}{2\pi} \sqrt{\frac{k}{\mu}} \quad (2.18)$$

2.10 Programs

The MD simulations were performed using the *Gromacs* program version 5.0.7 [127] compiled with MPI, Message Passing Interface, parallelisation. *Gromacs* or *Groningen Machine for Chemical Simulations* is a free package originally designed to investigate the dynamics of biochemical systems in solution [128]. *Gromacs* is widely used, because it is a comprehensive, fast and user-friendly program [129]. The DFT calculations were executed in *Gaussian09* revision E.01 [130]. All calculations were run on the *Dirac* computer cluster of the theoretical and computational chemistry department at KU Leuven. *Chemcraft* and *Avogadro* [131] were used to prepare the input configurations. Whereas *Chemcraft* allows for the precise manipulation of internal coordinates, *Avogadro* excels in crystallographic tools. Several scripts were written in *Python 3.6.0* to make and to adapt files. The output trajectories were visually inspected in *VMD* [132]. Finally, all graphs were plotted

in *Xmgrace*, except for the Lennard-Jones potentials. The latter curves were processed in *RStudio*.

Chapter 3

Structural model and methodology

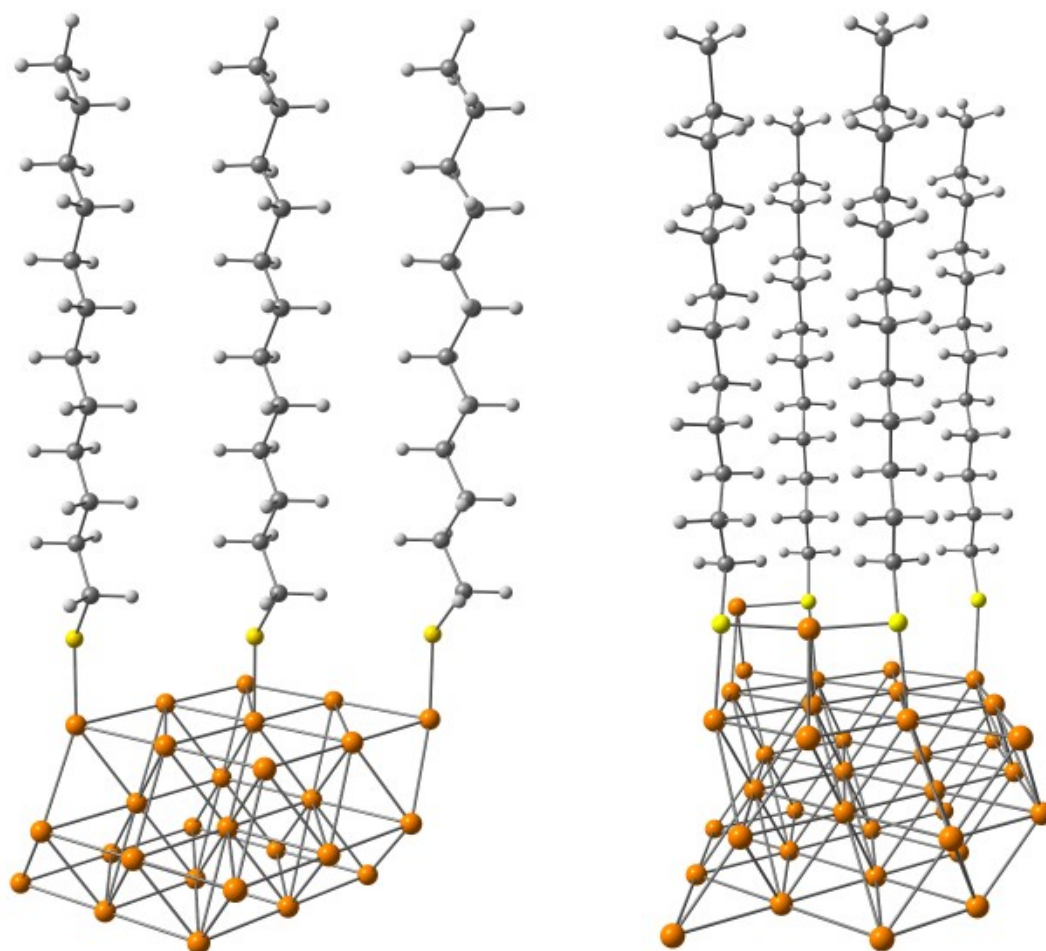
This chapter will elaborate on the structural model used in the simulations, on the set-up of the MD simulations and on the force field extensions for aluminium and gold atoms.

3.1 Structure of the dodecanethiol SAM on Au(111)

3.1.1 Structural model

As discussed in the *Introduction*, two models for the monolayer structure have been proposed in the literature [29, 40]. Historically, a flat gold substrate was assumed on which the alkanethiols arrange in a $(\sqrt{3} \times \sqrt{3})R30^\circ$ lattice. More recently the adatom model was proposed, in which two alkanethiols bind to one gold adatom in a staple motif [61]. Although the adatom model has been observed for short-chain monolayers and on gold nanoparticles, it has not been confirmed so far for dodecanethiol SAMs on a Au(111) substrate [40, 67, 133].

The repeat units for both models are shown in Figures 3.1a and 3.1b respectively. The models differ in interface and lattice structure, as can be observed from the different sulphur spacings. Whereas the headgroups are equidistant, 5 Å, in Figure 3.1a, several sulphur spacings are observed in Figure 1.10a. Nevertheless, the packing density of the dodecanethiol backbones is similar after tilting of the chains, because the van der Waals stabilisation is optimised for equidistant hydrocarbon chains. Given the fact that the two models yield similar densities and that the first model was used in most of the literature [29, 71, 92], the historical model was adopted in this work so to facilitate comparison of the results.



(a) Molecular structure of the repeat unit used in this work with orange, yellow, grey and light grey Au, S, C and H atoms respectively.

(b) Molecular structure of the repeat unit used for the construction of the adatom model with orange, yellow, grey and light grey Au, S, C and H atoms respectively.

Figure 3.1

Monolayers on Au(111) are studied the most due to the easy preparation and high quality SAMs [29, 39]. Hence, a Au(111) substrate was used for the simulations in this work. Since the structure of alkanethiol SAMs on other crystal planes and metals is different, the results obtained for a Au(111) surface cannot be generalised to other systems [59, 134].

The input configuration of the SAM monolayer on Au(111) was based on Figure 3.2 which was taken from the review paper of Love et al. [29]. At full coverage, the surface Au:S ratio equals 3:1. Although the sulphur atoms are positioned on top of hollow sites in Figure 3.2, there is no consensus on the adsorption position in the literature. DFT calculations on methylthiol monolayers point towards threefold hollow sites [45, 46, 47] or

bridge sites [48, 49] as being the most stable. In contrast, several experimental groups measured alkanethiol adsorption positions on top of a gold atom [50, 51]. Nevertheless, the exact adsorption site is not important for the performance of the simulations in this thesis, as the different binding sites can be interchanged by a translation the whole SAM layer on the gold surface. All three configurations, top, bridge or hollow sites, are characterised by identical SAM densities and hydrocarbon spacings.

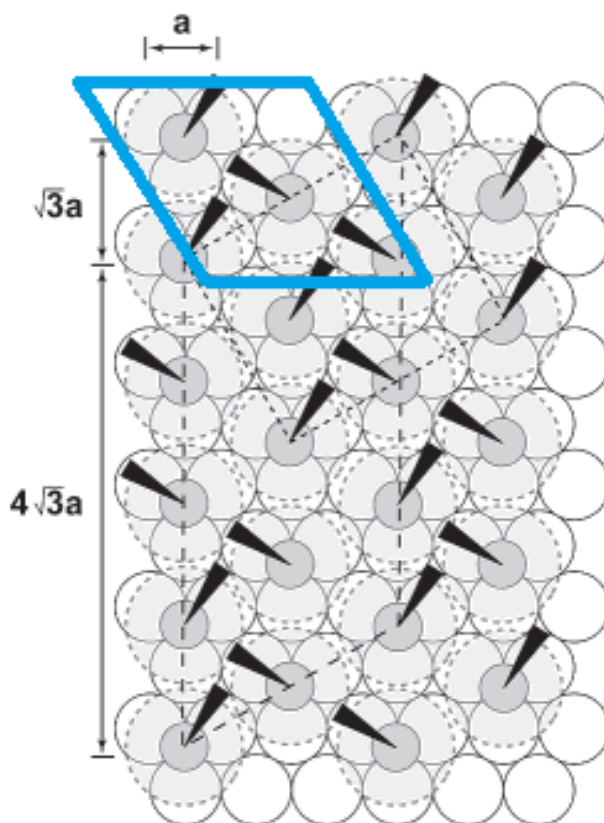


Figure 3.2: Schematic presentation of the SAM monolayer at full coverage, adapted from ref. [29]. Gold atoms in white, sulphur atoms in grey and alkanechains as black wedges. The repeat unit is indicated in blue.

In order to avoid changes of the lattice during the simulations, the positions of all gold and sulphur atoms were restrained. A script was written to generate the restraints and is included in Appendix D. To ensure that the lattice will remain rigid at all simulation temperatures a force constant of $500000 \text{ kJ/mol nm}^2$ was used. In practice, the translations of gold and sulphur atoms were limited to a few picometres. The use of restraints to fix the interface structure has two important consequences for this study. First, any desorption of the monolayer at higher temperatures, 400 K or more [74], is avoided. Second, as no headgroup movements are allowed, the formation of 5-7 dislocation pairs cannot be observed [71].

3.1.2 Building of the repeat unit

In order to perform MD simulations on the system of interest, an appropriate input file with all the atomic coordinates had to be created. The repeat unit in Figure 3.1a was build and multiplied via a script. First, the structure for a fcc gold lattice was downloaded from the *American Mineralogist Crystal Structure Database* [135, 136] and a crystal slab was cut in the (111) orientation. In a cubic closed packing arrangement, the lattice is build by repeating three distinct gold layers. Therefore, the gold lattice was represented by three layers of gold atoms. A parallelogram with a surface area of nine gold atoms was cut to serve as a repeat unit, as indicated in blue in Figure 1.9. This corresponds to a hexagonal unit cell with an angle of 60° defined between the two-dimensional lattice constants of length $3a$, with a the diameter of a gold atom. As a result, the repeat unit contains 27 gold atoms in total or nine per substrate layer.

At full coverage, the surface gold-thiol ratio equals one third. Hence, three alkanethiol molecules were placed on the gold surface. All sulphur atoms were positioned on top of a gold atom, because this conformation simplifies the definition of the bonded force field terms. In this case, only one Au-S bond needs to be defined, as compared to two and three for bridge and hollow sites respectively. Furthermore, the number of angles that need to be specified is significantly lower for an on top position. A 2.5 Å bond length was chosen, in agreement with theoretical and experimental results [49, 51].

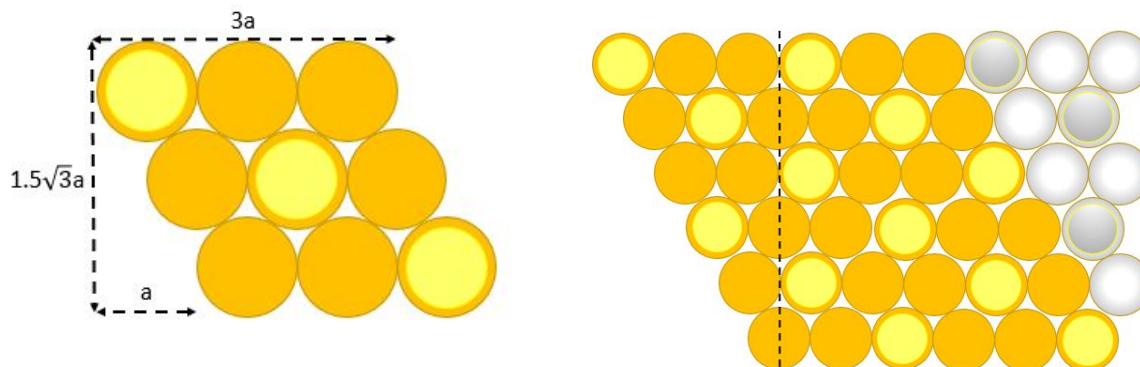
Since the results of Avila et al. [95] refer to a dodecanethiol SAM, the same chain length was used in this project. Several other publications also mention the use of dodecanethiols [25, 74, 89], because the vapour pressure is still sufficiently high to be vapour-deposited in the ALD reactor [22, 94] while the passivating properties and transition temperatures are higher as compared to shorter alkanes [24, 137]. The backbones were placed at right angles to the substrate, in analogy to the work of Mar et al. [70]. All C-C-C-C torsional angles are in the anti conformation and the chains have the same orientation, as shown in Figure 3.1a. During the equilibration of the systems, the chains will tilt and exhibit gauche defects according to the simulation temperature.

3.1.3 Multiplication of the repeat unit

The MD simulations were performed on a SAM consisting of 108 dodecanethiol molecules. A script was written to multiply the repeat unit. The script is included in Appendix D. In the y-direction, the repeat unit is translated over $1.5\sqrt{3}a$ with a the diameter of a gold atom (2.88375 Å), as calculated with the Pythagorean theorem. In a row, cells are translated over $3a$. Nevertheless, as the repeat unit is hexagonal, an additional translation of $1.5a$ is needed to obtain continuous edges.

A function was written to make the lattice orthorhombic, because this simplifies the definition of a box for the MD simulations. A wedge was defined by cutting the monolayer perpendicular to one pair of its parallel faces, as shown in Figure 3.3b. A translation of

this wedge over the length of the face transforms the surface area from a parallelogram into a rectangle.



(a) Schematic presentation of the unit cell multiplication parameters with gold atoms in orange and sulphur atoms in yellow.

(b) Schematic presentation of the transformation from a hexagonal to an orthorhombic lattice.

Figure 3.3

3.2 Set-up for the molecular dynamics simulations

In this section, the procedure and set-up of the MD simulations will be presented. An overview of the different steps and parameter files needed to set up a simulation will be given. The parameter files used in the simulations are included in Appendix C.

As *Gromacs* was developed for the simulation of biochemical compounds, it only processes protein database files *.pdb* as input structures. First, the *.pdb* file is converted to a Gromacs structure files *.gro*. This also creates a topology file *.top* and position restraints file *.itp* based on the selected force field. All conformational and atom-specific information is gathered in the topology file with a link to the force field. The position restraint file is automatically generated to restrain the positions of all non-hydrogen atoms. A script was written to replace this file, because only the positions of sulphur and gold atoms were restrained in this work.

After assigning a force field, the system is placed in a box. The SAM was positioned on the bottom of the box. The two-dimensional box vectors assigned to a monolayer of 108 dodecanethiol molecules were 5.1907 nm and 4.4953 nm in order to preserve the continuity of the crystal lattice. Since the orthogonal box vector was set equal to 5.0 nm, approximately half of the box contained vacuum to avoid SAM interactions with the next image box. Periodic boundary conditions were applied in all simulations in order to obtain bulk properties. Without pbc, the results obtained from our nanometre sized system would by no means be representative for the interactions occurring in an experimental SAM.

The next step is to minimise the energy of the system. The steepest descent minimisation algorithm was used for all simulations with a convergence criterium of 1 kJ/mol nm for the maximum force or a maximal number of 10^6 steps. A profound energy minimisation is not required in MD, as the trajectories are examined and not the equilibrium geometry. An equilibration run of 100 ps is performed next to assign particle velocities and to adjust the temperature of the system. Particle velocities in each direction are randomly assigned according to the Maxwell-Boltzmann velocity distribution function at the specified temperature and a correction is made to remove the center-of-mass motion. A constant temperature was maintained during the simulations by the v-rescale thermostat [119] with a time constant of 0.1 ps. A time step of 1 fs was used for the simulations. A small time step is necessary, because the hydrogen motions were not constrained. The van der Waals and Coulomb cut-off radii were set to 1 nm. PME was requested for long-range electrostatics and long-range dispersion corrections for the energy and the pressure were applied [104, 116].

The same settings as for the equilibration runs were used for the production runs. The coordinates and velocity information to start a production run was read from the output of the equilibration run. During the production run, the coordinates were written to a trajectory file in every 10 ps. As this file is used for the analysis of the results, the time resolution of the output analysis equals 10 ps.

3.3 OPLS force field extensions

The *Gromacs* program was originally developed to perform biochemical calculations. As a consequence, it is not optimised to simulate inorganic materials and the parameters for gold and aluminium atoms are not available. The force field extensions made for gold and aluminium atoms will be presented in this section and the parametrisation of a TMA molecule will be discussed.

3.3.1 Force field extension for gold atoms

New atom types for the gold atoms in the substrate had to be created. Three types of gold atoms can be distinguished, the atoms bound to sulphur, the atoms at the bottom of the box and the rest. An atomic mass of 196.96657 amu was assigned to each gold atom [138] and the position of all substrate atoms was restrained, as previously discussed.

The van der Waals parameters for gold were copied from the GolP force field [115]. GolP is a force field extension for OPLS designed to simulate the attraction of proteins to gold nanoparticles and Au(111) substrates in water. A rigid gold lattice without surface reconstruction was assumed in the GolP parametrisation, analogous to this work. The GolP force field is compatible with *Gromacs*.

Two bonded terms were added to the force field to account for the adsorption of the SAM on the substrate. First, a Au-S bond was defined. This pro forma term does not really

influence the dynamics, since the positions of both sulphur and gold atoms were restrained. Nevertheless, a bond was added to correctly represent the monolayer graphically. An equilibrium bond length of 2.5 Å was assigned in line with the input structure of the SAM. For the force constant, the largest value in OPLS was used. This corresponds to 502080 kJ/mol nm², which is close to the position restraint force constant. The value originates from the TIP4P four site water model [139].

Second, a Au-S-C angle was defined. Raman spectroscopy indicated that the S-C bond is approximately parallel to the gold surface [59]. DFT calculations on methanethiol monolayers proposed angles around 109° [30, 45, 48]. Since the exact value for a dodecanethiol SAM is not known, an equilibrium angle of 109° was set in this work. The Au-S-C force constant was set to 518.816 kJ/mol rad², by analogy with the C-S-C angle in thioethers such as methionine and thioanisole. The Au-S-C-C/H dihedrals were not defined because there were no appropriate torsional terms in OPLS which could be used in this case.

The gold atoms bonded to sulphur are partially charged by a value of 0.167 to compensate for the negatively charged, -0.335, sulphur headgroup. The value for the Au-S dipole corresponds well to the experimental charge obtained by surface potential studies [66]. A neutral charge was assigned to all other gold atoms.

3.3.2 TMA parametrisation

In order to simulate the TMA interaction with and diffusion through dodecanethiol SAMs, appropriate force field parameters had to be derived. This was done in a fitting procedure using reference data obtained with DFT. The MK [124] and CHelpG [125] population analyses as implemented in *Gaussian 09* were used to calculate the atomic charges for TMA. The molecular mechanics (MM) Lennard-Jones parameters were fitted to reproduce the potential curve of a rigid scan obtained by DFT. A DFT geometry optimisation defined the equilibrium bond lengths and angles in a TMA molecule. Finally, force constants for the bonded interactions were obtained from a normal mode analysis. Three new atom types, for Al, C and H atoms, were defined in OPLS to assign the parameters.

The B3LYP [121] functional and Def2-TZVP [122] basis set were used with Grimme’s empirical dispersion correction (GD3) [123], by analogy to the mechanistic investigations on the Al(CH₃)₃/H₂O ALD process discussed in the *Introduction* [14].

3.3.2.1 Non-bonded interactions

The most important force field terms to explore the TMA diffusion are the non-bonded contributions, as they determine the TMA-SAM interaction. It is essential to correctly model this interaction in order to obtain accurate results on the diffusion.

First, the atomic charges were calculated with the MK [124] and ChelpG [125] population analysis schemes. Both methods assigned slightly different charges on the hydrogen and carbon atoms of the three methyl groups in TMA, as shown in Figures A.1a and A.1b

in Appendix A. Averages of the hydrogen and carbon charges were taken and results were rounded to ensure the overall neutrality of TMA. The averaging is justified by the presence of a threefold rotational axis in a TMA molecule and the methyl group rotational symmetry [140]. The rounded TMA charges as calculated by the MK and CHelpG schemes are summarised in Table 3.1. Higher absolute values were calculated by the MK method as compared to the CHelpG analysis. Nevertheless, the difference in TMA-propane interaction energy by adopting a different set of charges was less than 1 kJ/mol. The CHelpG set with the smaller charges were used in the simulations.

Table 3.1: List of TMA charges calculated with the CHelpG and MK schemes.

Element	CHelpG charge	MK charge
Al	0.978	1.233
C	- 0.656	- 0.927
H	0.110	0.172

Second, the van der Waals interaction energy between TMA and the monolayer was established. In MD, the total vdW energy is approximated as a sum of pairwise contributions. Hence, the Lennard-Jones potential function presented in equation (Eq. 3.1) is evaluated for all pairs of atoms in the system and σ and ϵ need to be defined for all atomic combinations. This problem is handled in OPLS by assigning a set of parameters to each atom type. The parameters for the pairwise forces are obtained by geometrically averaging the atom type values, as indicated in (Eq. 3.2). The problem is thus reduced to finding an appropriate value of sigma and epsilon for the aluminium atom in TMA, as the standard van der Waals parameters were assigned to all carbon and hydrogen atoms.

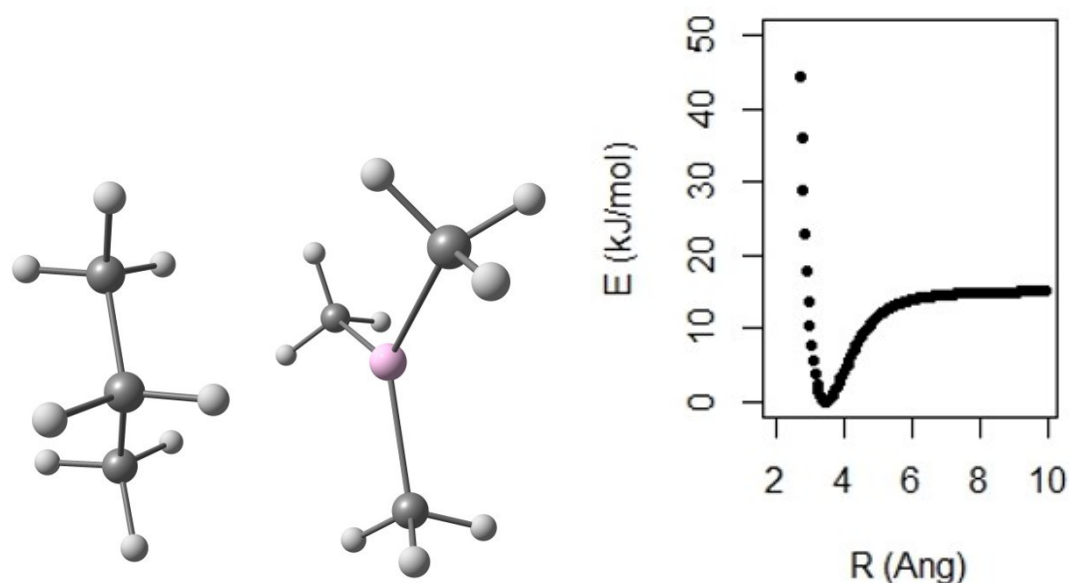
$$v(r_{ij}) = 4\epsilon_{ij} \left[\left(\frac{\sigma_{ij}}{r_{ij}} \right)^{12} - \left(\frac{\sigma_{ij}}{r_{ij}} \right)^6 \right] \quad (3.1)$$

$$\epsilon_{ij} = \sqrt{\epsilon_{ii}\epsilon_{jj}} \quad \sigma_{ij} = \sqrt{\sigma_{ii}\sigma_{jj}} \quad (3.2)$$

In order to correctly reproduce the monolayer-TMA interaction, the interaction energy as a function of the intermolecular distance was calculated with DFT. The SAM was approximated by a propane molecule, as the end group - TMA and alkane backbone - TMA interactions determine the diffusion probability. The limited extend of the van der Waals forces in combination with the use of cut-offs at 1 nm for the production runs eliminates the need to consider dodecanethiol molecules, because the non-bonded attraction of the sulphur headgroup does not reach beyond the dense dodecanethiol barrier. Furthermore, the penetration of the diffusant in the SAM was investigated. The TMA interactions at the interface, once reached, are not examined in this thesis.

First, the conformation of a TMA-propane complex was optimised. The equilibrium geometry is shown in Figure 3.4a. A rigid scan was performed to calculate the Lennard-Jones potential curve. In the rigid scan, the TMA-propane distance was linearly varied

without re-optimising the conformation and the potential energy was calculated at each step of the scan. A plot of the relative potential energy as a function of the TMA-propane distance is shown in Figure 3.4b. The scan comprised an increase and decrease of the TMA-propane distance as compared to the equilibrium distance by steps of 0.05 Å. In total, 161 steps were taken in the range of 1.96 to 9.96 Å. A well-depth of -15.0 kJ/mol was obtained.



(a) Equilibrium geometry of a TMA-propane complex.

(b) Lennard-Jones potential curve calculated with DFT.

Figure 3.4

The same configurations as in the scan were processed in *Gromacs*. Since there is no keyword in *Gromacs* to request a rigid scan, single point calculations were performed at the selected TMA-propane distances. A script was written to change the TMA-propane distance in steps of 0.25 Å, which corresponds to 5 times the DFT step size. The script is included in Appendix D. The molecules were placed in the middle of a cubic box with a lattice vector equal to 5 nm. Since the same settings as used in the simulations were applied, including pbc, the rather large box vector is necessary in order to avoid interactions with image boxes. Although a cut-off radius for the vdW and Coulomb interactions of 1 nm was used in the production runs described in the next chapter, the cut-off radii for the single-point calculations were doubled to 2 nm. The largest TMA-propane distance examined by DFT equalled 0.996 nm. The use of a larger cut-off radius prevents the introduction of a systematic error in the asymptotic value for the energy.

The potential energy of each TMA-propane configuration was calculated and scaled relative to the energy value at large distances. A well-depth of -8.7 kJ/mol was obtained. As the Lennard-Jones parameters for the aluminium atom were set equal to zero in the force field, the energy difference between the DFT calculated plot and the curve obtained from the MM single point calculations arises from the Al-propane Lennard-Jones interactions or 3 Al-C vdW terms and 8 Al-H vdW terms.

Estimates for σ and ϵ were made and improved by a fitting procedure. The vdW terms were written out for 18 different TMA-propane distances resulting in a system of 18 linear equations with two variables. A first guess for the parameter values was obtained by solving a system of two equations. A different set of equations returned a different set of parameters. This was expected, as several approximations are made in MM, e.g. the discretisation of the potential energy in several bonded and non-bonded force field terms. In addition, the functional forms implemented in the force field are not exact and electronic effects are not considered. As a result, there is a discrepancy between ab-initio and MM results.

Because of the complex relation between both parameters and the energy, a script was written to loop over all possible combinations of σ and ϵ between the smallest and largest values included in OPLS for the respective parameter. A step size of 0.001 nm and 0.01 kJ/mol was used respectively. The differences between the DFT and MM calculated relative energies was determined for each combination and a condition was added to ensure a small interaction potential at the largest distance. If the potential does not evolve to zero, a long-range particle attraction and systematically biased energy values can be expected.

By using the fitting procedure described above, a sigma value of 0.114856 nm was established. The optimisation of epsilon was more problematic. The larger ϵ , the stronger the TMA-propane interaction. Nevertheless, in order to obtain a well-depth comparable to the DFT result, a very large value for epsilon, around 200 kJ/mol, needs to be specified. This value is outside the range of ϵ values in OPLS as the largest value equals 26.15 kJ/mol, assigned to the lithium ion [141]. Moreover, the larger ϵ , the shorter the equilibrium TMA-propane distance. In addition, the root of the Lennard-Jones curve shifts to shorter distances and the asymptotic value slightly increases. The epsilon value was fixed at 100 kJ/mol, resulting in a well-depth of -13 kJ/mol. The DFT and MM calculated Lennard-Jones potentials are plotted in Figure 3.5 and the optimised van der Waals parameters are summarised in Table 3.2. The underestimation of the interaction potential made for TMA is lower than the thermal energy at the temperatures considered. Moreover, a rigid scan and single point energy calculations were also performed on a system consisting of two propane molecules. Whereas DFT assigned a maximal attraction energy of -9.6 kJ/mol relative to the value at large separation, -6.5 kJ/mol was calculated with OPLS in *Gromacs*.

Table 3.2: List of van der Waals parameters.

Element	σ (nm)	ϵ (kJ/mol)
S	0.360	1.485
C	0.350	0.276
H	0.250	0.126
Au	0.320	0.650
Al	0.115	100.0

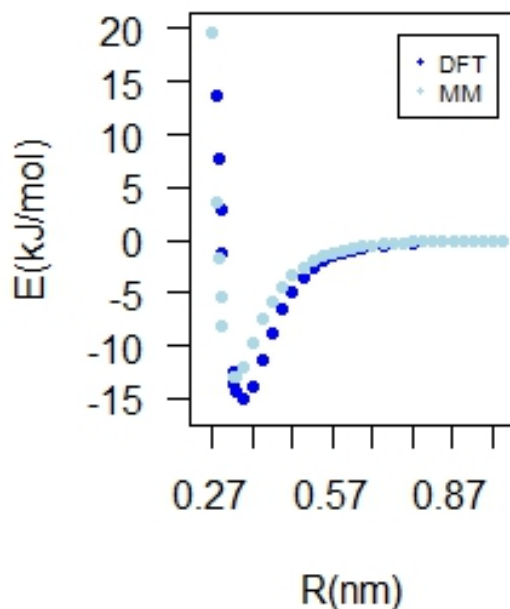


Figure 3.5: DFT and MM calculated Lennard-Jones potential curves for a TMA - propane interaction.

3.3.2.2 Bonded interactions

Once the parameters for the non-bonded force field terms were defined, the equilibrium values and force constants for the bonded terms were specified. A TMA molecule is completely defined by two bonds, C-Al and C-H, three angles, C-Al-C, H-C-Al and H-C-H, one dihedral angle, H-C-Al-C and one improper torsion to ensure a planar conformation. First, the latter two terms will be discussed.

The parameters for the Ryckaert-Bellemans dihedral were copied from the $H_{Me}-C_{Me}-C_{ring}-C_{ring}$ torsional angle in a toluene molecule. Six improper torsional terms are distinguished in the OPLS force field, three of which include a nitrogen atom. Improper terms are defined for carbonyl, nitro, amine and imine functional groups, alkenes and aromatic rings. The latter improper dihedral was selected for TMA, because of the configurational similarities to toluene. As shown on the Figures in the *Results*, a planar conformation was retained for all TMA molecules during the simulations.

The equilibrium bond lengths and angles shown in Figure 3.6 were obtained by a DFT geometry optimisation of a TMA molecule. The equilibrium values correspond well to the results of experimental [140] and theoretical [142] structure determinations.

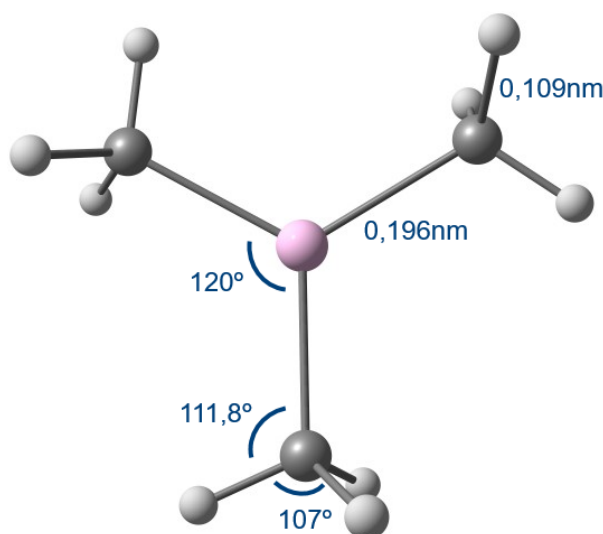


Figure 3.6: Equilibrium structure of a TMA molecule with the equilibrium values of the bonded force field terms indicated. C, H and Al atoms are grey, light grey and pink respectively.

The force constants were obtained via a normal mode analysis. First, the equilibrium bond lengths and angles and starting values for the force constants were entered in the OPLS force field. The starting force constants for the C-H bond and H-C-H angle were copied from alkanes. The $C_{ring}-C_{ring}-C_{Me}$ and $C_{ring}-C_{Me}-H_{Me}$ angular force constants from a toluene molecule were assigned to the C-Al-C and Al-C-H angles respectively. Finally, an initial value for the force constant of the Al-C bond vibration was replicated from a phosphonium molecule.

For the computation and diagonalisation of the Hessian, a double precision run is required in *Gromacs*. Since the double precision option was not installed on the *Gromacs* version 5.0.7 used throughout this thesis, the normal mode analysis was performed in *Gromacs* version 5.0+dftb. The TMA equilibrium geometry obtained by DFT was placed in a cubic box with a box vector of 5 nm. A potential-shift was requested for both Coulomb and vdW forces to ensure a smooth cut-off with a 2 nm cut-off radius.

The next step is to minimise the energy of the TMA molecule. A normal mode analysis requires a very tight energy minimisation. Since the standard steepest descent minimisation scheme is not sufficiently accurate, the conjugate gradient integrator with a maximum step size of 0.0001 nm and an unlimited number of steps was used. The maximal force was set equal to 10^{-7} kJ/mol nm, resulting in a complete minimisation of the energy.

After the energy minimisation step, the Hessian was calculated and diagonalised. The eigenvectors were visualised in *VMD* to determine the nature of the normal vibrational modes. Five modes were selected. The symmetric Al-C and C-H stretching vibrations and the symmetric methyl umbrella, rocking and degenerate bending motions were chosen to represent the Al-C, C-H bond stiffness and H-C-H, H-C-Al and C-Al-C angular stiffness respectively. The ratio between the DFT calculated frequencies and MD calculated frequencies was determined, squared and multiplied by the force constant of the respective mode in accordance with the relation between the frequency ν and the force constant k shown in (Eq. 3.3).

$$\nu = \frac{1}{2\pi} \sqrt{\frac{k}{\mu}} \quad (3.3)$$

The values for the force constants were adjusted in the force field and the whole procedure was repeated. By iteration, the force constants were improved until the MM calculated frequencies of the five modes converged to the values obtained by DFT. A comparison of the DFT and MM frequencies is included in Appendix B. There are still important differences between the two spectra, because MM is not an accurate method to examine a PES. Besides the approximations made to calculate the energy, as explained in the previous subsection, improper dihedrals are known to change the vibrational spectrum [102]. To eliminate errors arising from the calculation set-ups, the l-bfgs minimisation method and vdW PME long-range interactions were tested. The results obtained by the two methods, however, did not differ significantly. An overview of the final equilibrium values and force constants is given in Tables 3.3 - 3.4.

Table 3.3: List of bond stretching parameters for TMA.

bond	equilibrium value (nm)	force constant (kJ/mol nm ²)
C-Al	0.196	141754.7
C-H	0.109	310968.1

3.3.3 Force field extension for a SAM

Before the input structure can be processed in *Gromacs*, all atoms must be linked to the correct force field terms. In order to do that *Gromacs* groups particles in recognisable units called residues. For example, one amino acid corresponds to a residue in OPLS.

Table 3.4: List of angle bending parameters for TMA.

angle	equilibrium value ($^{\circ}$)	force constant (kJ/mol rad 2)
C-Al-C	120	177.44
H-C-Al	112	149.46
H-C-H	107	494.85

Other residues define ions or solvent molecules. The definition of residues to assign atom types has the advantage that an input file can be simultaneously processed by different force fields, because atom types are force field specific. One alkanethiol molecule and nine gold atoms were chosen as a residue. The input *.pdb* file assigns a residue type and a number to each atom. The residue file for the SAM was made by the *TPPmktop* program [143] and adapted to the system studied. The residue files for TMA, gold diffusants, propane and defective structures were made from scratch.

The sulphide atom type was assigned to the sulphur headgroups, in analogy to the methionine amino acid. Three different carbon atom types were used, CS, CH $_2$ and CH $_3$. All hydrogen atoms are of the same alkane type. Standard OPLS charges for S, C and H atoms were copied. In OPLS, the hydrogen atoms bear a charge of 0.06, which is counterbalanced by the charge on carbon to form a neutral charge group [111]. A charge group is a set of atoms whose charges sum to zero. The introduction of charge groups enhances the transferability of the force field and reduces artefacts at the cut-off distance [108]. The sulphur headgroups are negatively charged by a value of -0.335. The charge on the sulphur bonded carbon atoms equals 0.048, which is the standard charge for sulphide CH $_2$ carbons.

Chapter 4

Results and discussion

In this chapter, the results of the MD simulations will be presented and discussed. The goal of this thesis was to understand the interaction of TMA molecules with a dodecanethiol SAM on Au(111). This problem is of interest for the semiconductor industry in the context of area-selective deposition. Experimentally, a dodecanethiol monolayer failed to delay or inhibit the aluminium oxide thin film growth [95]. Several authors attribute the diffusion of ALD precursor molecules through the SAM to the presence of defects, but evidence supporting the assumption was not yet provided [93, 96]. Hence, our conclusions will help unravelling the role of defects in AS-ALD.

First, the thermal stability of the SAM conformation was examined at temperatures varying from 200 K to 600 K, because experiments revealed that the SAM inhibition properties towards the ALD process are inversely proportional to the temperature [95]. The obtained conformations will be compared with the results from previous MD simulations using various force fields [69, 70, 71]. Furthermore, the presence of a discrete melting transition was investigated, because it was hypothesised that headgroup mobility is a criterion to observe a melting point [71]. Our calculations allow to verify this hypothesis, as the substrate atoms and sulphur headgroup positions were restrained.

Second, the penetration of gold atoms in the SAM was inspected by inserting gold atoms in the vacuum above the monolayer. In particular, the presence of intrinsic diffusion channels in the monolayer was investigated [92]. Experiments indicated that gold atoms easily diffuse through the SAM and accumulate at the Au-SAM interface [86, 88]. Nevertheless, the mechanism for penetration has not been elucidated in the experimental studies.

Finally, the passivating properties of an alkanethiol SAM on Au(111) towards the aluminium oxide ALD process were explored. Trimethylaluminium molecules were inserted in the vacuum above the monolayer surface and the interaction with the SAM was examined. More specifically, the possibility of TMA penetration in the SAM was tested. Both a perfect monolayer and monolayers with point and line defects were simulated and the effect on the mobility of TMA was examined.

4.1 Thermal stability of the SAM conformation

4.1.1 Simulation set-up

The thermal stability of the SAM conformation was investigated on a perfect dodecanethiol monolayer at full coverage. Temperatures ranging from 200 K to 600 K were explored in steps of 100 K. Although most experimental results on TMA and Au atom diffusion are obtained in a temperature range between 300 K and 400 K, a simulation at 200 K was performed to obtain an ordered monolayer as a reference. The simulations at 500 K and 600 K were performed, because 600 K is the upper temperature for the aluminium oxide ALD process. At 600 K, TMA decomposes [10]. The desorption of the SAM at higher temperatures, approximately 450 K in vacuum conditions, is experimentally proven by several groups [58, 74, 144]. However, the alkanethiolates cannot desorb from the surface during the simulations due to the position restraints on the sulphur and gold atoms. Since no detailed study has been performed on the timescale of the desorption at various temperatures, the simulations are not superfluous. Whereas desorption experiments typically run over several minutes, the monolayer was only simulated for 20 ns.

First, the energy of the input structure was minimised and the SAM was equilibrated at 200 K for 100 ps. After a 20 ns production run, the temperature was raised by 100°. The temperature change was achieved by increasing the temperature of the external heat bath in the velocity rescaling thermostat [119]. The energy exchange between the heat bath and the box during the equilibration run gradually alters the particle velocities until a new equilibrium is found. Once the system was re-equilibrated, a production run of 20 ns was performed at 300 K. This scheme was repeated for all higher temperatures. Hence, the final structure of each production run served as an input for the equilibration run at a temperature increased by 100 K. The purpose of this strategy was to correlate the coordinates and velocities of the particles.

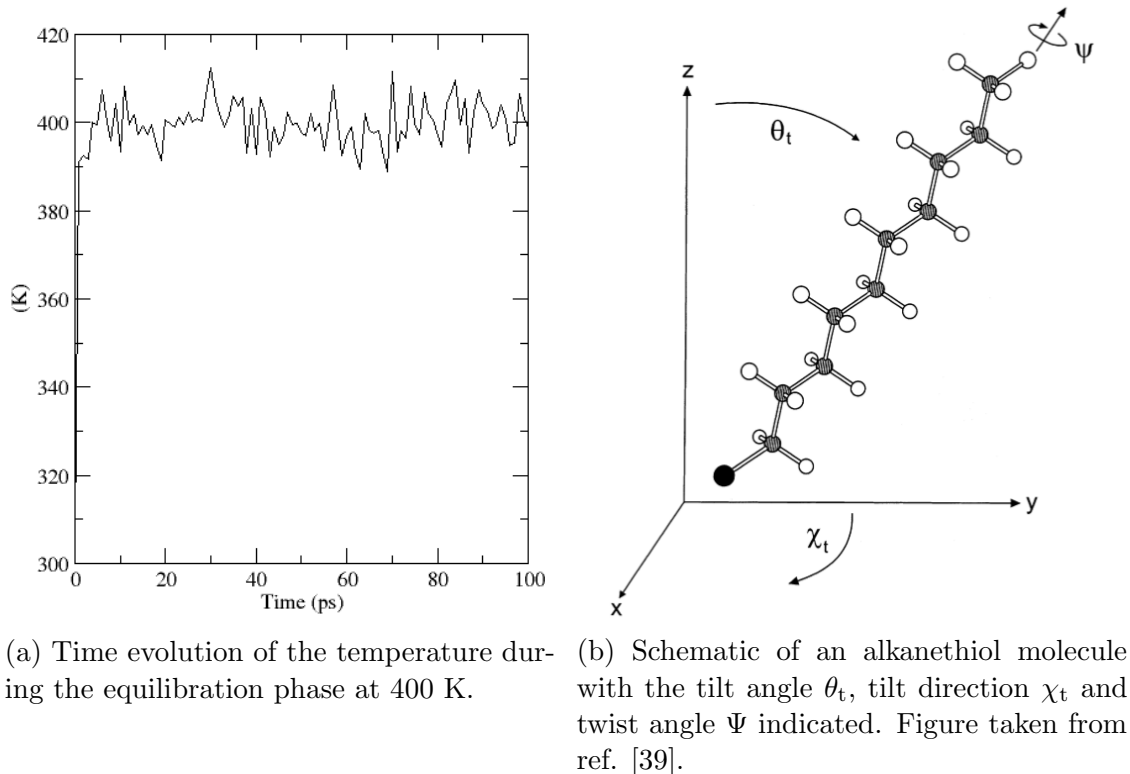


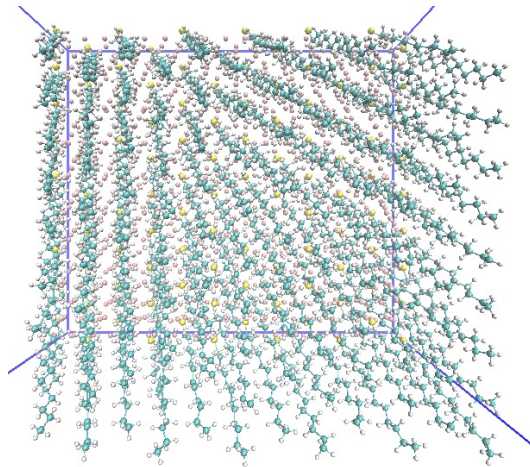
Figure 4.1

As shown in Figure 4.1a, 100 ps were sufficient to equilibrate the system at the new temperature. A fast initial temperature increase from 300 K to 400 K is achieved by using a coupling constant τ of 0.1 ps. Once at 400 K, the temperature deviations of the system are limited to approximately ± 10 K. Similar observations were made at 500 K and 600 K. The deviations at lower temperatures were limited to approximately ± 5 K.

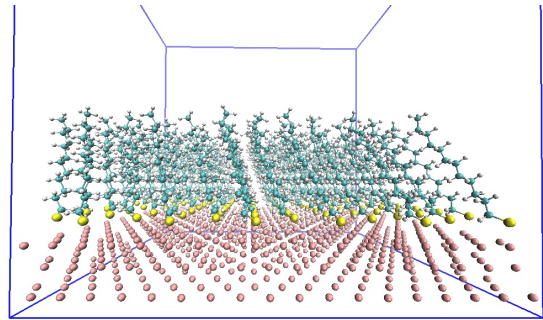
4.1.2 Results

The degree of order in the SAM is characterised by four angles. First, a tilt angle θ_t can be defined between the axis perpendicular to the surface and the dodecanethiol backbone, as shown in Figure 4.1b. Second, the tilt direction can be measured by evaluating the angle χ_t between the projection of the dodecanethiol backbone on the substrate and a Cartesian axis. Third, the twist angle Ψ denotes the rotation of the chains with respect to their axis. Finally, the fraction of anti-periplanar C-C-C-C torsional angles was quantified.

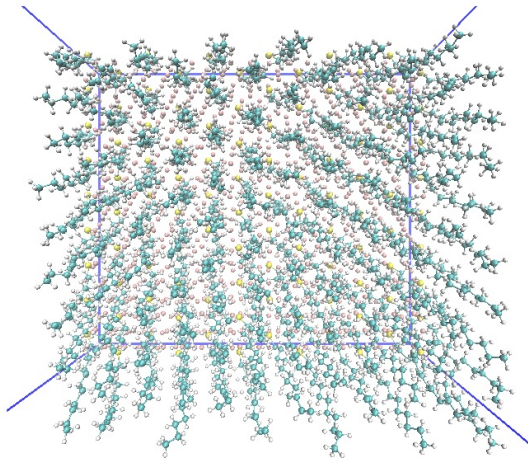
The monolayer conformations at 200 K, 400 K and 600 K are shown in Figure 4.2. Figures of the SAM at 300 K and 500 K are presented in Appendix A. While the backbones are all-anti and uniformly tilted at 200 K, the blocking layer is disordered at 600 K. Since the van der Waals interaction energy is optimised by adopting a constant hydrocarbon distance in the SAM, at low temperatures a perfect structure characterised by an uniform



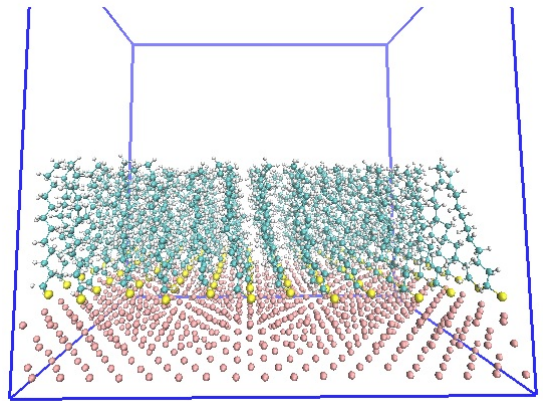
(a) Top view of the monolayer at 200 K.



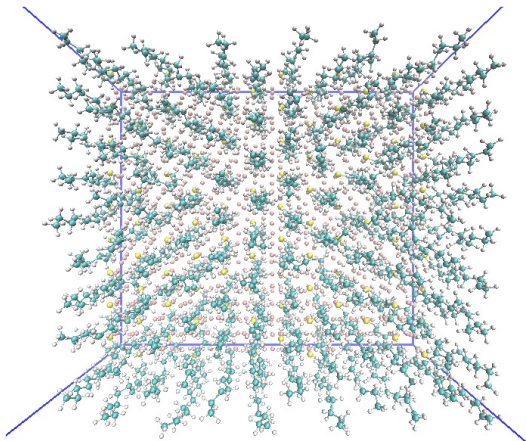
(b) Side view of the monolayer at 200 K.



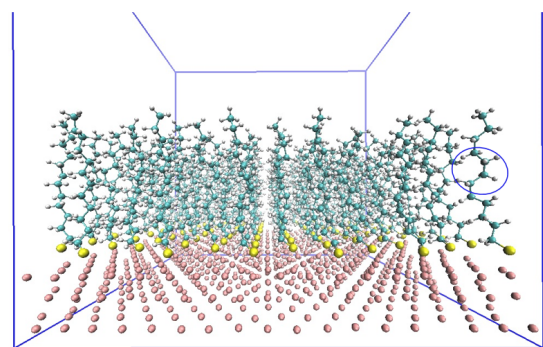
(c) Top view of the monolayer at 400 K.



(d) Side view of the monolayer at 400 K.



(e) Top view of the monolayer at 600 K.



(f) Side view of the monolayer at 600 K. The formation of a kink is indicated in blue.

Figure 4.2: SAM conformations at various temperatures.

tilt angle, tilt direction and all-trans conformation is observed. The increased thermal energy of the SAM at higher temperatures is reflected in more disorder in the monolayer.

The simulations indicate that the average tilt angle gradually decreases as a function of increasing temperature, as shown in Figure 4.2. To quantify the conformational changes, the tilt angles were calculated. The tilt angle was defined as the angle between a vector perpendicular to the SAM surface and a vector defined by the dodecanethiol headgroup and the sixth carbon atom in the SAM chain. As summarised in Table 4.1, an average tilt angle of $37.00^\circ \pm 0.38^\circ$ was measured at 200 K. The angle was reduced to $35.30^\circ \pm 1.73^\circ$ at 300 K. This is slightly higher as compared to most of the experimental values reported in the literature, being $30^\circ - 34^\circ$ [26, 62, 65]. At higher temperatures, the dodecanethiols untilt and the tilt angle is more broadly distributed, as shown in Figure A.4. Although a visual inspection of the conformation at 600 K reveals an untilted, disordered monolayer, a rather high average tilt angle is calculated. This is an artefact of the definition the tilt angle, since the Au-S-C bond angle of 109° and zigzag structure of the chains imposes an intrinsic tilt on the vector connecting the headgroup and the middle carbon atom of the dodecanethiol. Nevertheless, the overall trend of a reduced and more broadly distributed tilt angle at higher temperatures is clear.

Table 4.1: Average tilt angles at various temperatures.

Temperature (K)	Tilt angle \pm stdev. ($^\circ$)
200	37.00 ± 0.38
300	35.30 ± 1.73
400	29.83 ± 3.44
500	24.51 ± 4.17
600	21.31 ± 4.34

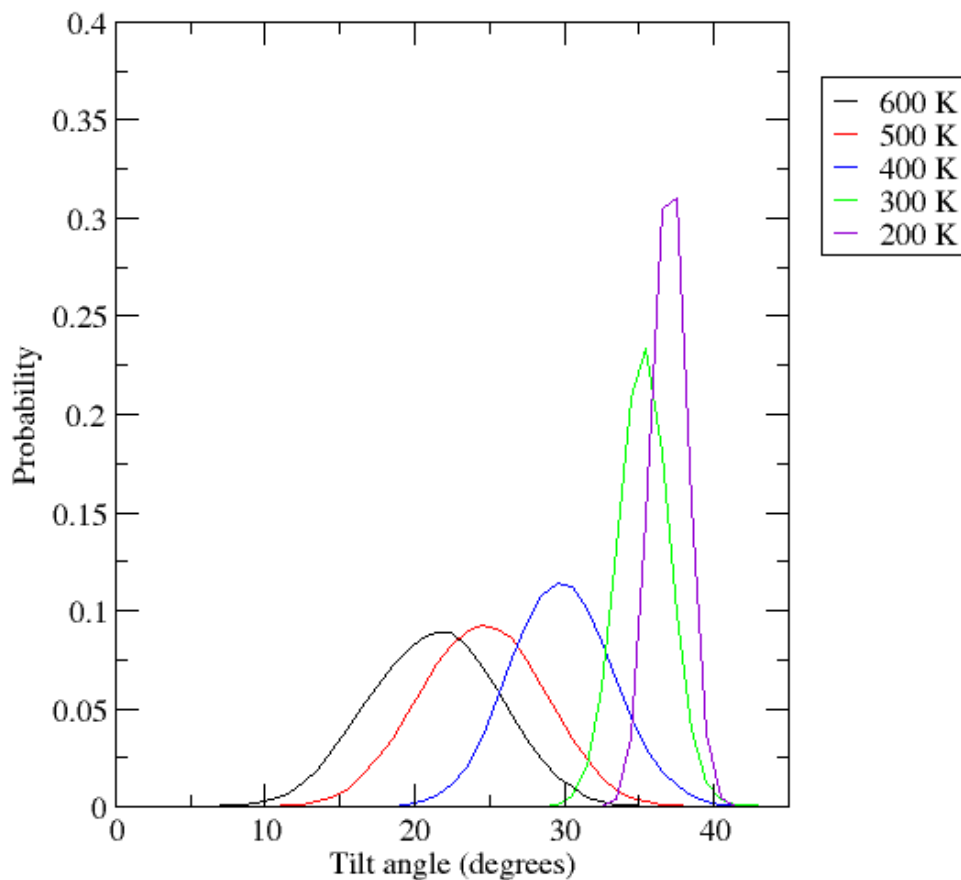


Figure 4.3: Distribution of the tilt angles at various temperatures.

Although the azimuthal angle was not determined, a uniform tilt direction is adopted at 200 K, 300 K and 400 K, as shown on Figures 4.2a, A.2b in Appendix A and 4.2c respectively. The presence of a next-nearest neighbour (NNN) tilt is concluded from visual inspection.

The presence of two discrete twist angles at 200 K and 300 K is deduced from visual inspection of the orientations of the first methylgroup in the SAM. A broadly distributed twist angle is observed at higher temperatures. A similar observation was made in earlier molecular dynamics studies on alkanethiol SAM structures [70].

Finally, the C-C-C-C dihedrals were examined. At 300 K, variations of the torsional angles are mainly concentrated near the end groups of the alkanethiols. At 400 K, conformational defects are also situated at the interface and the end groups are more readily disordered. At 500 K and 600 K, gauche and eclipsed conformations are present throughout the chain. Kinks are formed in order to accommodate the chain in the dense SAM layer, as indicated in Figure 4.2f. The temperature evolution of the fraction of anti-periplanar C-C-C-C dihedrals is summarised in Table 4.2. At 200 K the number of gauche defects is negligible. Although the anti-periplanar fraction decreases at higher temperatures, a high

percentage is measured even at 600 K. This results from the high density of alkanethiols in the SAM at full coverage. A slight change of the dihedral can significantly alter the conformation, resulting in a repulsive interaction with the neighbouring chains. A histogram of the C-C-C-C torsional angles at various temperatures is included in Appendix A. The distribution function is broader at higher temperatures, by analogy to the trend observed in the tilt angle distribution function.

Table 4.2: Fraction of anti-periplanar dihedrals at different temperatures.

Temperature (K)	fraction \pm stdev. (%)
200	99.88 ± 0.15
300	99.06 ± 0.49
400	94.41 ± 1.25
500	89.74 ± 1.55
600	87.73 ± 1.65

4.1.3 Discussion

Before drawing conclusions, the impact of the starting structure on the results was tested. According to Bhatia et al. [71] gauche defects are irreversibly trapped upon cooling of the monolayer. Hence, if the simulations would have been performed in the opposite order, starting from the disordered SAM at 600 K, different trans fractions would have been measured. However, the simulations performed in this thesis are 200 times longer than the production runs of Bhatia et al. [71]. Since the dihedral correlation times calculated in *Gromacs* were smaller than the simulation times, the torsional angles in the final conformation should be independent from the input structure. In Figure A.5 in Appendix A, the fraction of trans dihedrals is plotted as a function of time at 600 K. The average value does not change. Nevertheless, the hypothesis of Bhatia et al. [71] was tested by simulating a monolayer build from a defective repeat unit, shown in Figure 4.4. In one third of the chains a gauche conformation between the tenth and eleventh carbon atom was introduced. A kink was formed in the remaining dodecanethiols in the middle of the chain or near the interface. In the energy minimisation step, the conformational defects were already partly corrected in order to reduce the repulsion in the dense monolayer. After a 100 ps equilibration run and a 20 ns production run at 200 K, the tilt angle distribution and trans fraction did not differ from the previously calculated values. In conclusion, the results of the conformational analysis are independent of the starting conformation.

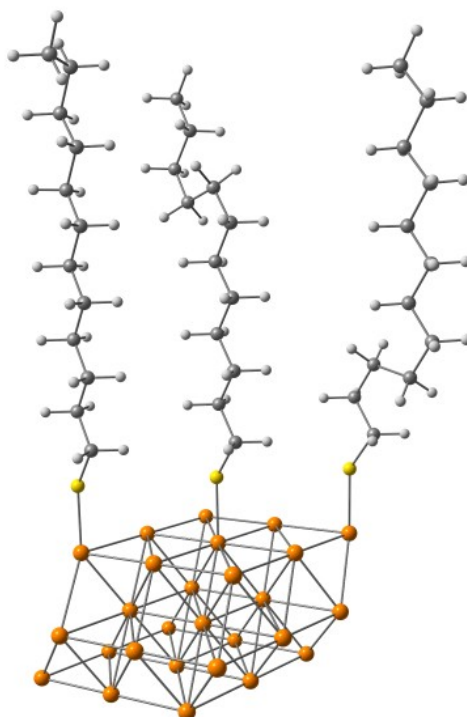


Figure 4.4: Repeat unit for the input configuration with torsional defects, with orange, yellow, grey and light grey Au, S, C and H atoms respectively.

At all temperatures, more ordered conformations are obtained in this study as compared to previous MD studies [69, 70, 71]. The gauche fractions measured by Hautman et al. [69], Mar et al. [70] and Bhatia et al. [71] are summarised in Table B.1. Whereas Bhatia et al. [71] used an united-atom model without position restraints on the sulphur and gold atoms, the temperature studies of Hautman et al. [69] and Mar et al. [70] were performed using restricted headgroup motions and an united-atom and all-atom approach respectively. The force fields were composed of fitted functions and potentials adopted from other groups. Although there is a discrepancy between the gauche fractions obtained in ref. [71] and ref. [69], the same hydrocarbon potentials were used. Hence, a restriction on the motion of the sulphur atoms results in a lower fraction of gauche dihedrals at higher temperatures.

The tilt angle distributions calculated by Bhatia et al. [71] are plotted in Figure 4.5. At 200 K and 300 K, the average tilt angles are consistently lower as compared to the tilt angles obtained in this study and the distributions are broader. MD simulations based on an all-atom model with headgroup restrictions also measured smaller tilt angles at all temperatures [70]. However, the evolution of the gauche positions and the twist angles correspond to previous observations [70]. In conclusion, a similar qualitative description of the conformational changes is presented, but the SAM is consistently more ordered in this study as compared to structures obtained with other force fields. Since a uniformly parametrised force field and less approximations were used in this study as compared to

the previous studies, it would be interesting to investigate the role of the force field in the degree of disorder in the SAM.

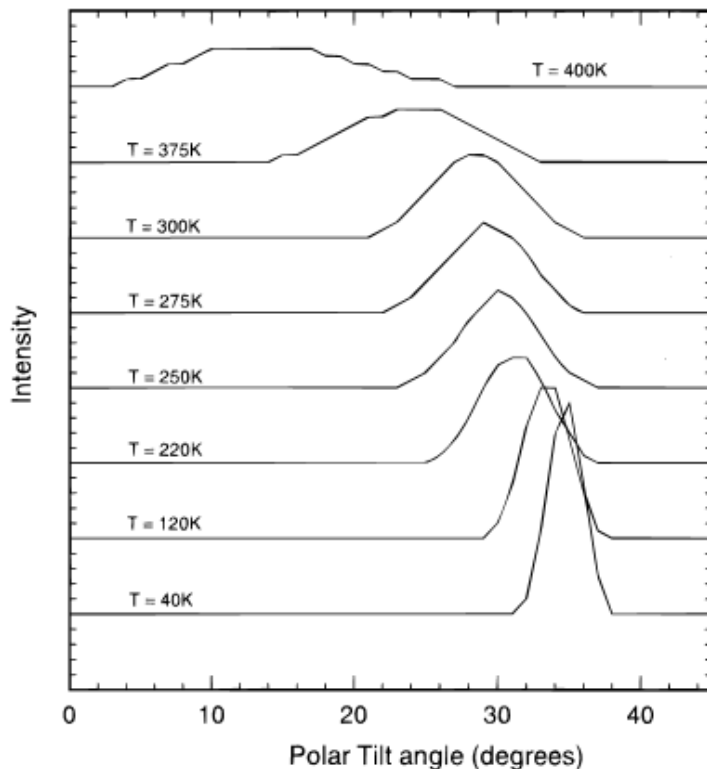


Figure 4.5: Distribution of the tilt angles at various temperatures as calculated by Bhatia et al. [71].

Table 4.3: Literature values for the fraction of gauche dihedrals at different temperatures.

Temperature (K)	Reference			This work
	[69]	[70]	[71]	
200	NA	NA	NA	0.12
250	0.3	2.2	NA	NA
300	NA	4.4	0.5	0.94
375	NA	NA	3.4	NA
400	8	NA	11.6	5.59
500	17	NA	NA	10.26
600	NA	NA	NA	12.27

The previous UA MD simulations on tridecane and hexadecane SAMs identified a low-temperature phase transition characterised by jumps in the tilt direction from the NN to

NNN direction at approximately 275 K [69, 71]. However, an uniform NNN tilt direction was found by MD simulations with an all-atom model, analogous to this work [70]. In addition, Bhatia et al. [71] observed a discrete phase transition from an ordered to a disordered conformation at 400 K, as evident from the broad tilt angle distribution in Figure 4.5, a randomisation of the tilt direction and an suddenly increased amount of gauche defects, present throughout the monolayer. A continuous phase transition was noticed in this thesis, by analogy with the results obtained from SAMs with position restraints on the sulphur atoms [69]. This confirms the hypothesis on the importance of the headgroup mobility in the observation of a discrete second phase transition [71]. The formation of 5-7 dislocation pairs is essential for the melting of the monolayer. The melting transition occurs over a wider temperature range if the translational freedom of the alkanethiol molecules is restricted.

4.2 Gold atomic diffusion

After having investigated the thermal stability of the SAM structure, gold atoms were added to the vacuum. As discussed in the *Introduction*, the vapour deposition of gold atoms on the monolayer results in the formation of gold islands at the substrate-SAM interface [86, 87]. Moreover, a continuous penetration of the monolayer was observed without significant changes in the SAM conformation [85]. The gold clusters at the interface were randomly distributed. As the positions of the clusters are not related to substrate defects, several groups hypothesised that the diffusion does not depend on the defectivity of the monolayer. Nevertheless, it is not clear whether the gold atoms separately diffuse to the interface and then cluster or whether clusters are formed before penetration [86]. As the mobility of the gold atoms at the interface is not resolved, the role of defects in the diffusion process cannot be excluded. By simulating the interaction of gold atoms with a SAM at full coverage, we hope to add to this discussion.

4.2.1 Simulation set-up

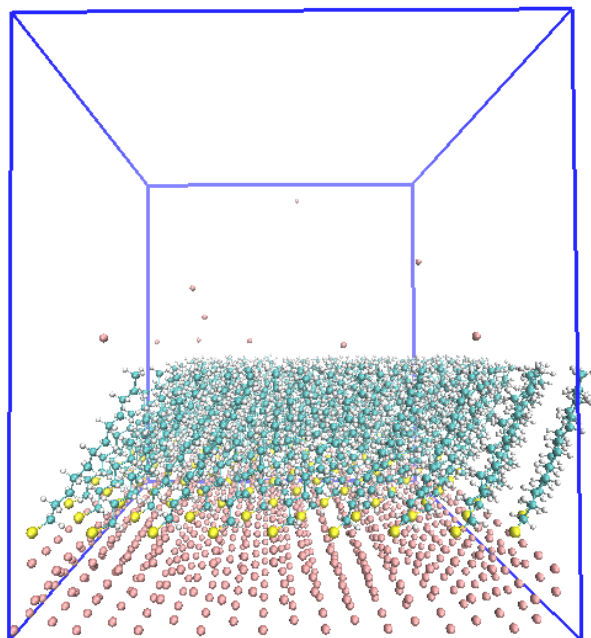


Figure 4.6: Image of the SAM and ten gold adatoms at 200 K with Au, S, C and H atoms pink, yellow, cyan and white respectively.

Ten gold atoms were randomly distributed in the vacuum above the SAM layer, as shown in Figure 4.6. This resulted in a partial pressure of 7.09 bar, under the ideal gas assumption at 300 K (Eq. 4.1). The number of gold atoms was chosen in analogy to previous MD simulations, where nine gold atoms were added to a monolayer of 90 dodecanethiols [89]. Hence, the partial pressure of gold is slightly lower in our simulations. Moreover, Alkis et al. [89] inserted the gold atoms in a 2 nm vacuum volume, whereas the boxes in this thesis are separated by a 2.5 nm vacuum layer.

$$p = \frac{Nk_B T}{V} = \frac{10 * 1.38 * 10^{-23} J/K * 300K}{5.19 * 4.50 * 2.50 * 10^{-27} m^3} = 7.09 \text{ bar} \quad (4.1)$$

First, a new residue and input file were written. Each contained only one gold atom, so that the number of atoms in the box could easily be adjusted. The atom type of the substrate gold atoms not bonded to a sulphur atom was assigned to the diffusants. This explains the choice to model the penetration of gold atoms, because appropriate parameters were already available in the force field.

Two adaptations to the force field were made before the diffusion was simulated. Due to the periodic boundary conditions, the gold atoms interact with the bottom of the gold layer in an image box positioned on top of the simulation box. In the GolP force field extension for OPLS, the gold-gold interaction is set equal to zero. As a result, the added

gold atoms can diffuse through the fcc lattice due to the lack of repulsive vdW interactions. Allocating the standard Lennard-Jones parameters for gold atoms to both diffusants and the gold substrate results in clustering of the added gold atoms near the substrate. In order to avoid attraction to or even penetration through the gold substrate, a repulsive vdW term was added to the force field.

$$v(r_{ij}) = 4\epsilon_{ij} \left[\left(\frac{\sigma_{ij}}{r_{ij}} \right)^{12} - \left(\frac{\sigma_{ij}}{r_{ij}} \right)^6 \right] \quad (4.2)$$

The expression for the Lennard-Jones potential as implemented in OPLS is presented in Formula (Eq. 4.2). A short-range repulsive term and long-range attractive term can be distinguished. As evident from (Eq. 4.2), the repulsive contribution is a lot steeper as compared to the attractive part. The expression in (Eq. 4.2) contains two parameters. The collision diameter σ corresponds to the root of the function, whereas the well-depth ϵ denotes the potential energy at the minimum. The collision parameter was set equal to twice the van der Waals radius of a gold atom. A vdW radius of 0.166 nm was used in agreement with the measurements of Bondi [145]. The Au-Au repulsion was realised by assigning a small value for ϵ . Whereas the Au-Au attraction is minimal for a small-well depth, the repulsive part remains rather steep due to the different powers in Equation (Eq. 4.2). Several values were tested. The fitting resulted in an optimal well-depth of 0.001 kJ/mol. Since the same atom type was used to describe the gold diffusants and the gold atoms in the substrate lattice, the position restraint force constant was doubled in order to avoid disintegration of the substrate. A force constant equal to 1000000 kJ/mol nm² was used.

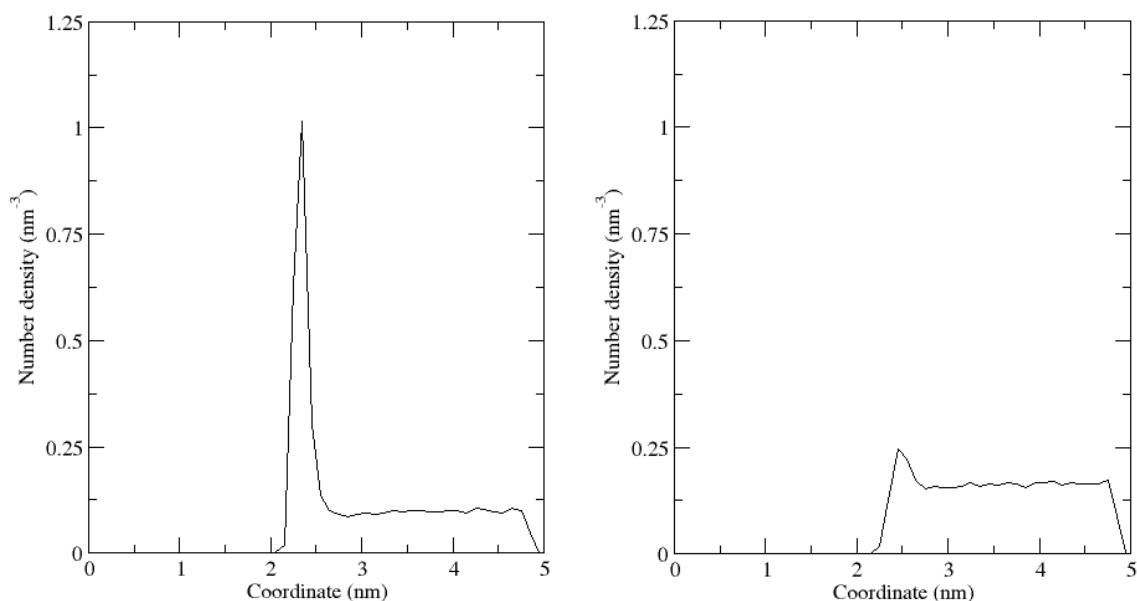
The gold atoms were added to the boxes from the thermal stability studies at 200 K, 300 K and 600 K. Hence, the monolayers were fully equilibrated at the correct temperatures. However, all velocity information is lost during the insertion, so only the coordinates were conserved. Velocities were reassigned according to the Maxwell-Boltzmann distribution function at the corresponding temperature by a 100 ps equilibration run. At 200 K, the monolayer is nearly ideal, which allows to test the presence of intrinsic diffusion channels in a perfectly ordered SAM [92]. Since the MD simulations of Alkis et al. [89] were performed at 300 K, the diffusion was also studied at 300 K. Finally, simulations at 600 K were performed to examine the effect of disorder in the SAM. In addition, the high thermal energy of the gold atoms at 600 K enhances the penetration.

After equilibrating the system at 200 K, 300 K and 600 K, three successive production runs of 20 ns, 50 ns and 30 ns were performed, resulting in a total simulation time of 100 ns. This is ten times longer as compared to the simulations performed by Alkis et al. [89].

4.2.2 Results

Despite the long simulation time, no diffusion of gold atoms in the SAM was observed at 200 K, 300 K or 600 K. Density profiles for the 50 ns simulations at 200 K and 600 K

are shown in Figures 4.7a - 4.7b respectively. The number density, the number of gold atoms per volume, is plotted versus the z-coordinate of the box, which is the coordinate perpendicular to the surface of the monolayer. The origin corresponds to the bottom of the gold substrate and the surface of the SAM is situated at approximately 2.1 nm. No density is present in the monolayer at both temperatures. At 200 K, the gold atoms are attracted to the SAM surface by the van der Waals interactions resulting in an increased density on top of the SAM surface. This peak is significantly reduced at 600 K due to the increased thermal energy of the gold atoms. The density drop near the top of the box results from the induced repulsive van der Waals interaction between the gold diffusants and the gold substrate in the next image box, as previously explained.



(a) Number density of the gold diffusants along the z-axis at 200 K.

(b) Number density of the gold diffusants along the z-axis at 600 K.

Figure 4.7

4.2.3 Discussion

The results contradict several hypotheses and conclusions from the literature. First, Alkis et al. [89] already investigated the penetration of gold atoms in dodecanethiol SAMs on Au(111) via MD simulations using the UFF force field. Although they initially did not observe diffusion, the UFF force field was modified to achieve a better agreement with experiments, predicting diffusion, and DFT calculations. The gold-alkane Lennard-Jones potentials were scaled by a factor of ten to match binding energy curves obtained by DFT, as shown in Figure 4.8. The binding energy of the gold atoms is plotted versus the height above the gold surface for tilted, by 35°, and untilted SAMs. Although they report a good agreement, an important difference was not mentioned. Peaks in the binding energy at the

SAM surface and interface were calculated by DFT, as shown in the left plot on Figure 4.8. In contrast, the binding energy as calculated with the scaled force field, shown on the right, increases during the diffusion in the tilted SAM. This difference has major consequences on the barrier properties of the monolayer. Almost all adatoms penetrated the monolayer when the scaled force field was used. The agreement with experiments reporting gold atom diffusion was merely a goal of their calibration, rather than a result of it. The calculations performed in this work question the validity of their approach. With the OPLS and GolP force fields, no diffusion was observed, although ten times longer simulations were run. The gold atoms are merely attracted to the SAM surface in agreement with the binding energy peak calculated by DFT [89].

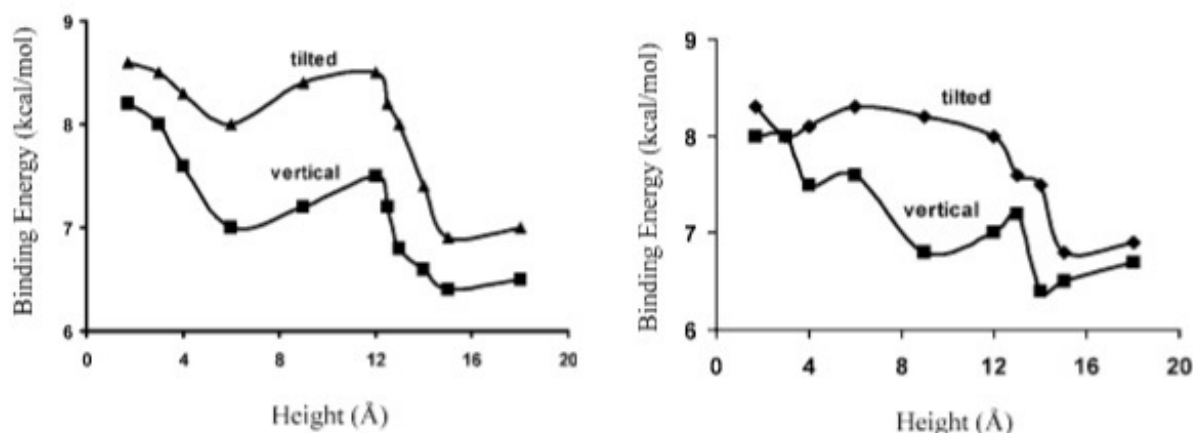


Figure 4.8: Plot of the gold atom binding energy versus the interface distance calculated by DFT (left) and UFF*10 (right), as used in ref. [89].

Hooper et al. [90] explained the aluminium diffusion through a hexadecanethiol monolayer via a headgroup hopping mechanism. Transient diffusion channels would be formed by fluctuations in the alkanethiol adsorption position. The hypothesis cannot be tested in this work as the headgroup positions were restrained. However, Dai et al. [92] disputed the hypothesis of Hooper et al. [90] by calculating the interchain distance in a perfectly ordered SAM based on the packing of the SAM backbones. They predicted that all particles with a diameter of less than 3 Å fit in the intrinsic channels present in an ideal monolayer. Two assumptions were made. First, a backbone tilt angle of 25° was assumed. Second, the alkanethiol molecules were represented by cylinders. The diameter of the cylinders was based on the covalent radii of the hydrogen atoms, which is significantly lower than the van der Waals radius. Channel diameters of 3.2 Å and 2.9 Å were obtained for untilted and tilted SAMs respectively. Calculations based on the vdW radii obtained a channel diameter of 1.4 Å if no chain tilt was assumed. The atomic and van der Waals radius of a gold atom equals 2.88 Å and 3.32 Å respectively [42, 145]. Hence, gold atoms should diffuse in the SAM if the van der Waals repulsion is not taken into account. Nevertheless, the 37° tilt angle obtained in this study at 200 K, as compared to the 25° assumption of

Dai et al. [92], results in a smaller channel diameter, equal to 2.56 Å and consequently no diffusion is expected. Indeed, no penetration was observed at 200 K during a 100 ns simulation.

Although at 600 K the average tilt angle is reduced to $21.31^\circ \pm 4.34^\circ$, no diffusion was observed either. Hence, increasing the thermal energy of the particles and the disorder in the SAM does not result in penetration of the SAM over a 100 ns timescale. In conclusion, diffusion of gold atoms through a dodecanethiol SAM at full coverage was not observed. The experimentally measured gold diffusion is likely to be caused by defects or by the headgroup hopping mechanism [90]. The results obtained in this study justify the use of ideal SAMs as blocking layers in the area-selective deposition technique.

4.3 TMA diffusion in a perfect monolayer

The main goal of this thesis was to resolve the interaction of a TMA precursor with a dodecanethiol SAM on Au(111) by computational means. The hydrophobic backbones have been reported to be effective barriers for several ALD processes [25]. Nevertheless, the SAM passivating properties depend on the ALD precursor and are not fully understood [95]. An unaffected growth curve for the aluminium oxide deposition was measured. By simulating the interaction of TMA molecules with a dodecanethiol SAM, we want to gain insight in the area-selective deposition process.

4.3.1 Simulation set-up

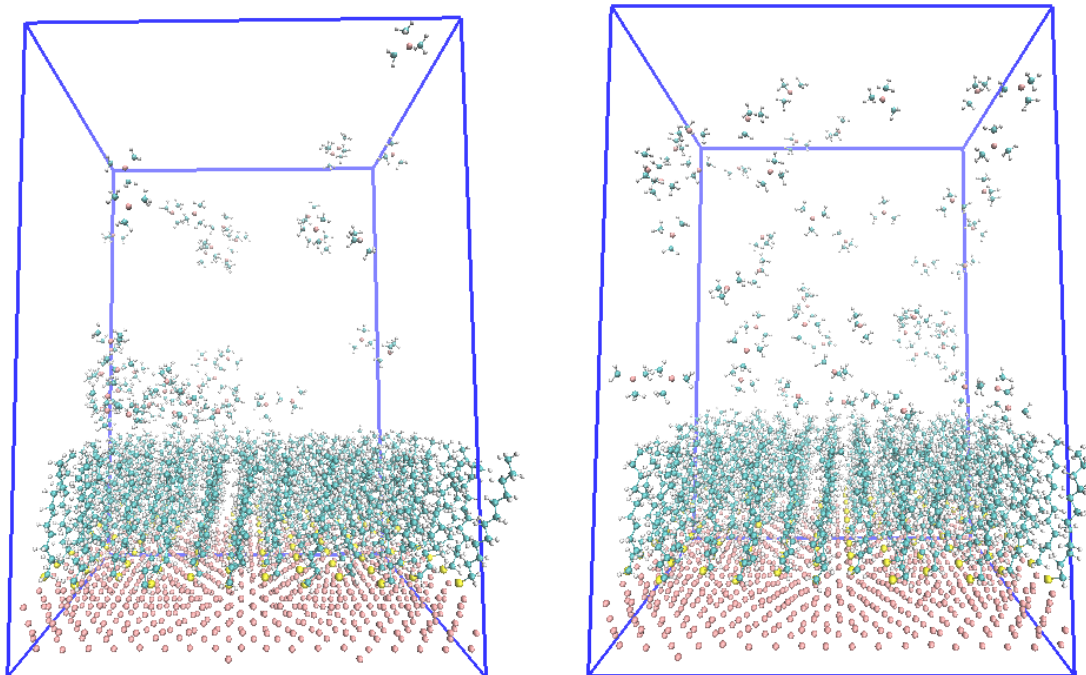
First, the interaction of TMA with a dense, perfect monolayer was investigated. The simulations were performed at two temperatures, 400 K and 600 K. A temperature of 400 K was selected, because this is the boundary of the SAM stability limit and the formation of TMA monomers [140]. Simulations at lower temperatures were not performed, because at low temperatures TMA exists as a dimer with a 3-center-2-electron bond [146]. The simulations at 600 K were run to serve as a first indication for the possibility of penetration in the SAM, because the increased thermal energy of the precursor molecules and the more disordered monolayer could enhance the penetration process. 600 K is the upper temperature for the TMA ALD process [10].

As explained in the previous section, the application of pbc introduces errors at the top of the simulation box, where the diffusants interact with the gold lattice of an image box. Therefore, the van der Waals interactions between TMA and the gold atoms on the bottom of the next image box were adjusted. A Lennard-Jones potential term was added and the well-depth was fitted. As opposed to the previous section, a different atom type was used for the lower gold layer as compared to the other gold atoms in the substrate. This allows to define a different vdW interaction. The repulsive contribution dominates for the TMA interaction with the bottom gold layer, whereas an attractive potential is maintained with the rest of the lattice. The collision diameter σ was set equal to the sum

of the vdW radii of gold and the respective elements in TMA [147]. An optimal epsilon value of 0.0002 kJ/mol was found.

The partial pressure of TMA in the ALD reactor depends on the reactor type used and is not always known [148]. Although it approaches one molecule for the box size simulated in this study, higher partial pressures were used in order to improve the statistics. No representative results can be obtained from one TMA molecule due to the limited simulation time, since the results from 50 ns simulations cannot be compared to experimental pulse times of 15 ms or more [95]. Various numbers of TMA molecules were added to the box. The highest number of TMA molecules added was 54, corresponding to a TMA:SAM ratio of 1:2. This number was chosen for the production runs, although it is much higher than the value implied by the experimental conditions. The enormous partial pressures, 15.5 bar and 42.7 bar at 400 K and 600 K respectively, significantly increase the chance of observing diffusion. In order to accommodate the large number of particles, the vacuum volume above the SAM was doubled. An orthogonal box vector of 7.5 nm was used for all TMA simulations resulting in a 5 nm vacuum layer. This also reduces the errors induced by the pbc, as the particles are less confined in the vertical direction.

As a consequence of the high partial pressure and aluminium van der Waals parameter, the TMA molecules tend to form clusters. Clusters of various sizes are clearly present at 400 K as shown in Figure 4.9a. Nevertheless, not all diffusants are part of a group and various small clusters do not aggregate further. As single TMA molecules were also present in the vacuum, the TMA-TMA vdW terms were not adjusted. Only the Al-Al Lennard-Jones potential was set equal to zero. At 600 K, the clustering is significantly reduced by the thermal energy of the precursor molecules, as shown in Figure 4.9b.



(a) Final conformation of the TMA diffusion simulation at 400 K.

(b) Final conformation of the TMA diffusion simulation at 600 K.

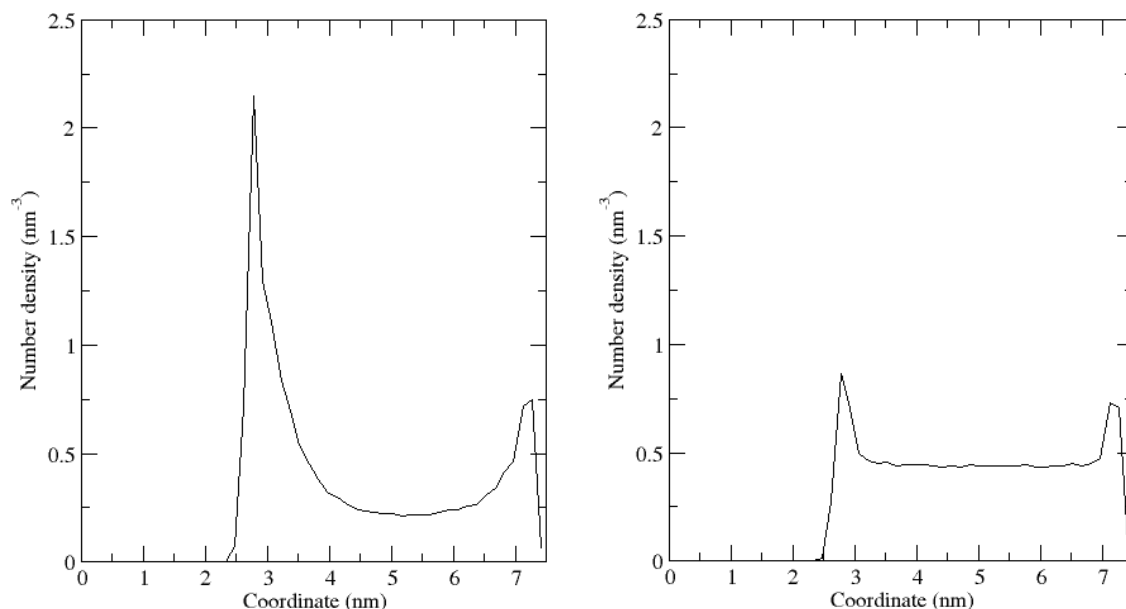
Figure 4.9

The TMA molecules were added to the pre-equilibrated boxes obtained from the temperature studies at 400 K and 600 K, in analogy to the set-up used for the simulations of gold atomic diffusion. A second equilibration run of 100 ps and production runs of 50 ns were performed. The energy of the system was not minimised after adding the TMA molecules, because the insertion algorithm ensures a random TMA distribution in the vacuum. Any overlap between particles is carefully avoided.

4.3.2 Results

A TMA molecule can be approximated as a cylinder with a height of 0.41 nm and a 0.69 nm diameter based on the vdW radii of the hydrogen atoms. The sulphur separation in the $(\sqrt{3} \times \sqrt{3})R30^\circ$ lattice of the SAM equals 0.5 nm. Hence, no diffusion was expected and no diffusion was observed at either 400 K or 600 K. The density profiles at both temperatures are shown in Figures 4.10a and 4.10b respectively. The peaks at 2.8 nm indicate the TMA-SAM attraction. Although reactions cannot be investigated with classical MD, Xu et al. [13] established by DFT that TMA does not chemisorb on the methyl end groups. Only after wetting of the surface, an aluminium oxide layer was deposited on top of the monolayer [98]. The increased thermal energy of the particles at 600 K results in a decreased TMA density on top of the SAM surface. A second peak is observed at the top of the simulation

box. The steep decrease at 7.5 nm results from the fitting of the van der Waals repulsion between TMA and the next image box, as previously explained.



(a) Number density of TMA along the orthogonal box vector at 400 K.

(b) Number density of TMA along the orthogonal box vector at 600 K.

Figure 4.10

4.4 TMA diffusion in a defective monolayer

Since no diffusion was observed in a SAM at full coverage, defects were introduced in the monolayer. The impact of point and line defects in the SAM on the interaction with TMA was examined. Several experimental studies emphasised the role of defects as nucleation sites for ALD precursor molecules [93, 95]. The aluminium oxide ALD process was even used to visualise defective sites in the SAM at 333 K [76]. The aluminium oxide nucleated at the defective sites, while the amount deposited on the surface of the SAM was minimal. Moreover, the deposition did not introduce new defects. In contrast, Avila et al. [95] ascribe the breakdown of the SAM passivating properties to defect formation. This argument was also formulated by Hashemi et al. [96]. They developed a sequential regeneration technique to restore the SAM layer after it gradually desorbed during the ALD process. Although a different substrate and precursor were used, desorption might explain the TMA deposition on a dodecanethiol passivated Au(111) substrate as well. Simulations of the effect of defects on the barrier properties of the SAM will contribute to this discussion.

4.4.1 Simulation set-up

Several point and line defects were introduced by selectively removing dodecanethiol molecules from a perfect monolayer. First, a new residue type was created for the defective sites. The new residue contained nine substrate gold atoms, by analogy with the SAM residue, but none of them is bonded to an alkanethiol molecule. In the input structure, all backbones were at right angles to the surface and the conformation of all hydrocarbon torsional angles was anti, as explained in the *Structural model* chapter. The input geometry for a SAM at full coverage with a point defect equal to two missing dodecanethiols is shown in Figure 4.11a. Point defects of various sizes were introduced in the middle of the monolayer. The surface area of the defective sites always was approximately circular. In this way, the simulations mimic an isotropically expanding pinhole. Circular point defects ranging from one to six missing chains were created. Second, line defects were introduced by removing one, two or three rows of dodecanethiol molecules. Since complete rows were deleted, infinite line defects were simulated by the application of pbc, by analogy with the missing rows on SAM domain boundaries [74, 76].

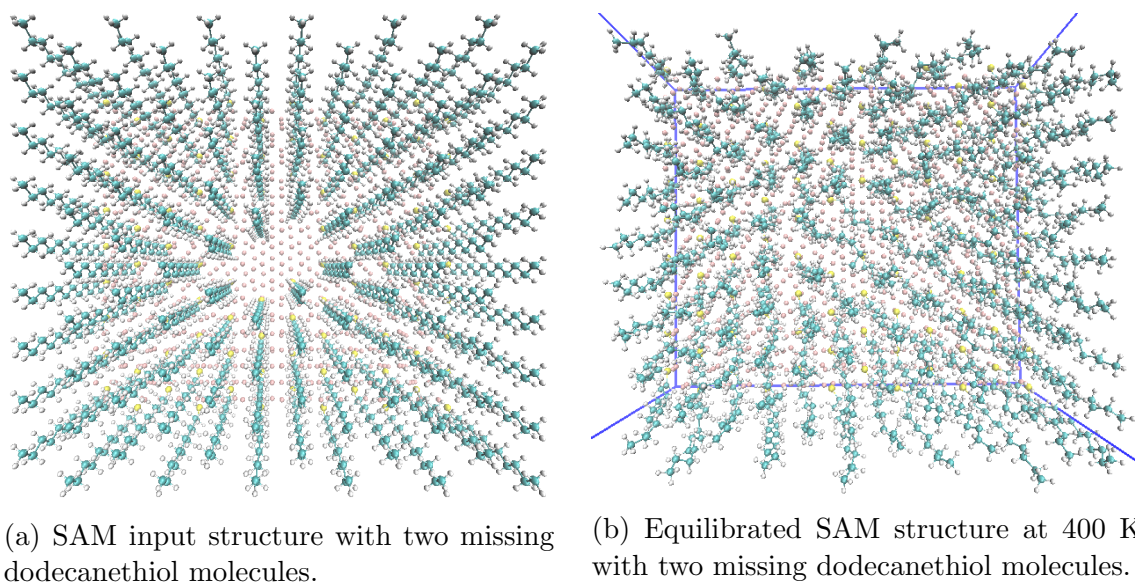


Figure 4.11

The energy of the input geometry was minimised and equilibration runs of 100 ps were performed. All defective sites were simulated at 400 K. After equilibration of the monolayer, 54 TMA molecules were added and a second equilibration run was performed to assign new particle velocities according to the Maxwell-Boltzmann distribution function at 400 K. The two equilibration runs are necessary due to the following reasons. The first run serves to adopt a realistic SAM conformation at 400 K before the TMA gas is added. After the energy minimisation, the dodecanethiol backbones are still perpendicular to the surface. As a result, the defective sites are not yet covered by the surrounding SAM

molecules. TMA molecules could possibly diffuse to the SAM-substrate interface in the early moments of equilibration resulting in wrong conclusions. After the first equilibration run, the defect is partly covered by neighbouring dodecanethiol molecules, as shown in Figure 4.11b for a monolayer with two adsorbates removed, and the TMA molecules can be inserted in the vacuum. The diffusion was investigated on a timescale of 50 ns.

4.4.2 Results

Penetration did not occur in monolayers with one or two deleted SAM molecules. However, a TMA molecule diffused in the pinhole made by removing three dodecanethiol molecules after 24 ns, as shown in Figure 4.12. The molecule remained in the monolayer for approximately 160 ps, after which it returned to the vacuum. The diffusion was established by visualising the trajectories in *VMD*. No TMA density was observed in the SAM layer on the density profile, because only a limited number of TMA molecules, out of 54, entered the monolayer for a short period of time during a 50 ns simulation. Hence, the TMA density in the monolayer was levelled out. As expected, larger pinholes promoted more diffusion.

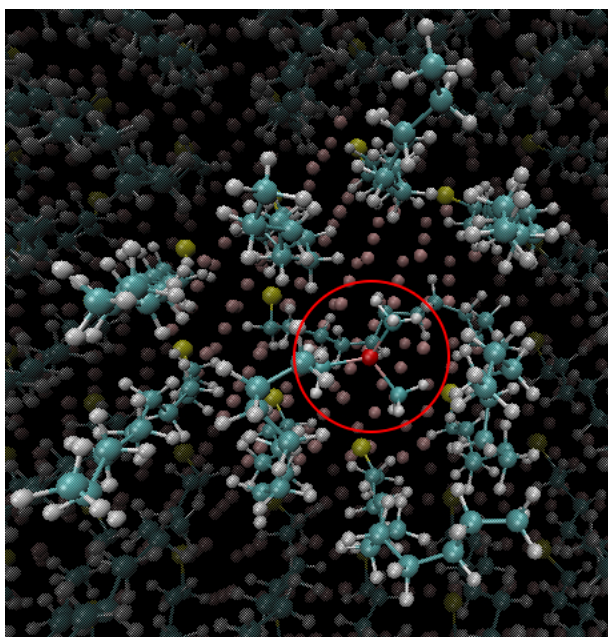


Figure 4.12: Image of a TMA molecule diffused in a defect made by removing three dodecanethiol molecules with Au, S, C, H and Al atoms in pink, yellow, cyan, white and red respectively.

Removing one row of dodecanethiol molecules did not promote diffusion. Line defects made by removing two and three rows in the SAM resulted in frequent diffusion with large peaks in the density profiles, as shown in Figure 4.13. The first peak at 0.975 nm corresponds to an aluminium position near the first and second carbon atoms of the dodecanethiol SAM. The latter two peaks were explained in the previous section in the

context of Figure 4.10a. The TMA molecules cluster on top of the SAM surface or diffuse to the interface, because the neighbouring dodecanethiol molecules tilt to cover the defect. Therefore, once a TMA molecule penetrated the SAM, it is trapped at the interface until the neighbouring SAM molecules untilt and TMA can diffuse back to the vacuum volume.

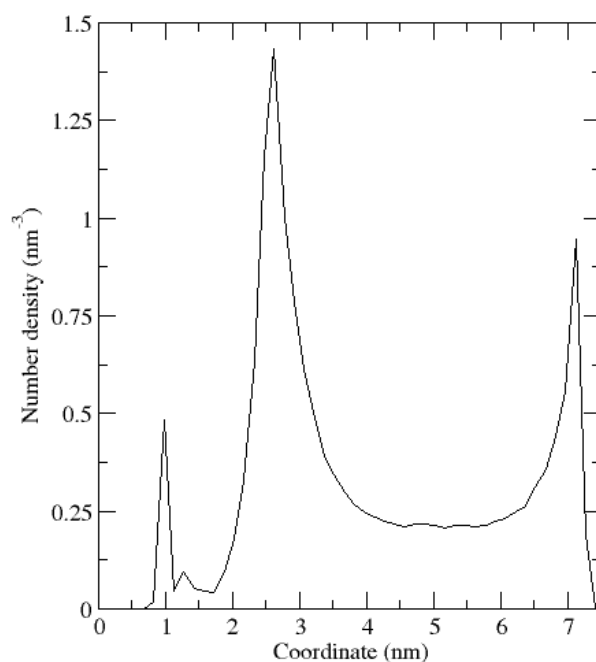


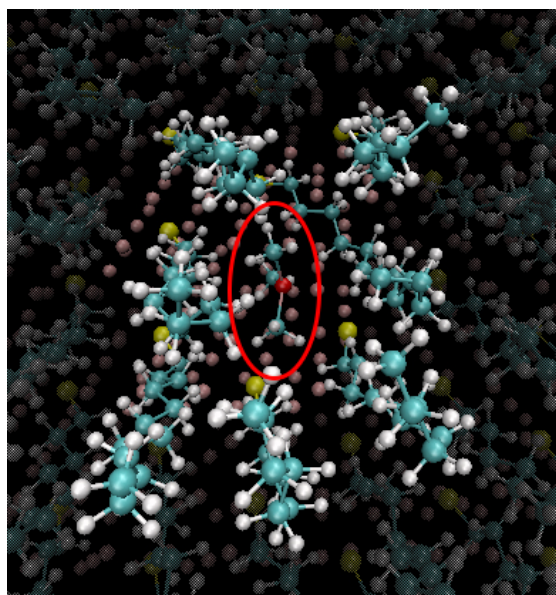
Figure 4.13: Density profile corresponding to TMA diffusion in a SAM with two missing rows.

4.4.3 Discussion

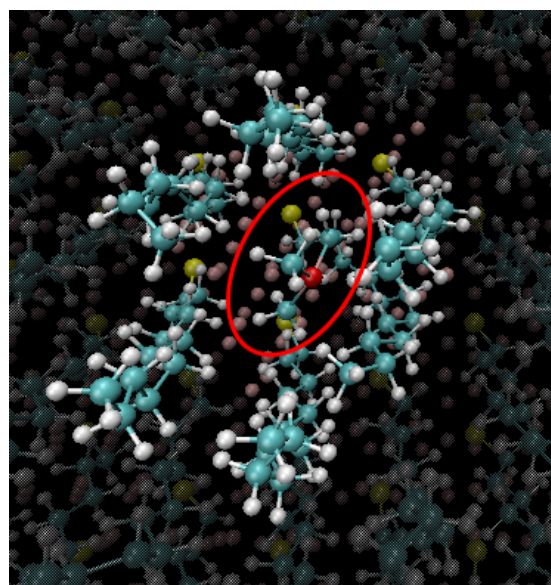
Whereas TMA penetrates into a pinhole of three missing chains, it does not penetrate into pinholes made by deleting one or two dodecanethiol molecules during the 50 ns simulations. This raises the question whether small defects can influence the passivation properties of the SAM layer. First, the errors induced by the force field need to be ruled out. The TMA - alkane interaction was based on DFT calculations, but the TMA - TMA interaction was not. Due to the high density and high epsilon vdW parameter of aluminium, the formation of TMA clusters was observed. Hence, the influence of varying the TMA - TMA attraction on the diffusion process was investigated. The $\text{Al} - \text{C}_{\text{TMA}}$ and $\text{Al} - \text{H}_{\text{TMA}}$ ϵ values were halved from 5.25 kJ/mol and 3.54 kJ/mol to 2.63 kJ/mol and 1.77 kJ/mol respectively. The TMA - TMA interaction is now equal to that of one TMA molecule and three SAM end groups.

The reduced TMA-TMA interaction generated diffusion. TMA molecules penetrated the pinhole formed by two missing dodecanethiol molecules, as shown in Figure 4.14a, and the line defect introduced by deleting one full row in the SAM. A TMA molecule

diffused halfway through the monolayer in the smallest point defect, made by removing one dodecanethiol molecule, but did not reach the SAM-Au interface, because the interface was covered by a neighbouring dodecanethiol molecule, as shown in Figure 4.14b.



(a) Image of a TMA molecule diffused in a defect made by removing two dodecanethiol molecules with Au, S, C, H and Al atoms in pink, yellow, cyan, white and red respectively.



(b) Image of a TMA molecule diffused halfway a defect made by removing one dodecanethiol molecule with Au, S, C, H and Al atoms in pink, yellow, cyan, white and red respectively.

Figure 4.14

Second, the diffusion was simulated at 600 K using the original vdW interaction parameters. The TMA molecules were not able to penetrate the monolayer, although a frequent interaction with the surface of the SAM was observed. The defective site was always covered by the neighbouring dodecanethiol molecules.

Chapter 5

Conclusions and outlook

The goal of this thesis was to investigate the interaction of trimethylaluminium molecules with a dodecanethiol self-assembled monolayer on Au(111). SAMs are used for the selective passivation of surfaces in the context of area-selective deposition. Nevertheless, an uninhibited growth of an aluminium oxide film by the ALD process on a dodecanethiol passivated Au(111) substrate was experimentally observed [95]. Since the experiments did not resolve the mechanism for TMA deposition, molecular dynamic simulations were performed to examine the SAM passivating properties on a molecular scale.

First, simulations at different temperatures between 200 K and 600 K were performed to evaluate the thermal stability of the monolayer conformation, because a reduction of the SAM passivating properties with increasing temperature was experimentally observed [95]. At 200 K, a dense and perfectly ordered monolayer is formed, characterised by all-trans hydrocarbon backbones, an average tilt angle of $37.00^\circ \pm 0.38^\circ$ and two discrete twist angles. Increasing the temperature resulted in reduced tilt angles and broadening of the tilt angle distribution. *Gauche* dihedrals in the hydrocarbon backbones, first at the end groups and starting from 500 K also in the middle of the SAM, and various twist angles were observed. In general, more ordered conformations were obtained as compared to previous MD studies, where less uniform force fields were used [69, 70, 71].

A continuous phase transition from an ordered SAM at 200 K to a disordered monolayer at 600 K is observed, as predicted by Bhatia et al. [71]. Position restraints on the alkanethiol headgroup, as applied in this work, obstruct the melting of the monolayer resulting in a continuous phase transformation. Analogous simulations without position restraints on the sulphur atoms could be performed to confirm this conclusion and elucidate the exact melting temperature of the SAM.

Second, the penetration of gold atoms in the SAMs was examined at 200 K, 300 K and 600 K. Gold atom penetration in an alkanethiol monolayer was described by several experimental groups, but the mechanism of diffusion is not yet resolved [84, 85, 87]. Ten gold atoms were added to the vacuum and 100 ns simulations were run in order to investigate the presence of intrinsic diffusion channels in the monolayer [92]. No diffusion of the gold atoms in the monolayer was observed, in line with a previous MD study on a

similar system using the UFF force field [89]. The authors modified the UFF force field to obtain a better agreement with DFT results, but the observations made in this thesis, based on the more accurate OPLS and GolP force fields, question this approach. Even at 600 K, when the system is characterised by a disordered monolayer and high thermal energies, no penetration was observed. Nevertheless, it is still possible that the simulation time of 100 ns is too short to observe diffusion. A more general conclusion could be drawn by performing an umbrella sampling, which could quantify the potential energy barrier for diffusion.

A second explanation for the atomic diffusion in SAMs is based on a headgroup hopping mechanism [90]. The formation of dynamic diffusion channels could not be investigated in this thesis due to the position restraints on the dodecanethiol headgroups. It would be interesting to test this hypothesis by simulating the gold atom diffusion in a monolayer without position restraints.

Third, the diffusion of TMA molecules in a perfect SAM at 400 K and 600 K was investigated. In order to perform the simulations, the OPLS force field as implemented in *Gromacs* was extended. Even for a very high TMA partial pressure (used in order to enhance the diffusion), no penetration was observed. This was expected based on the results from the gold diffusion. The TMA molecules formed clusters on top of the SAM surface. The umbrella sampling method could again provide more information on the probability of the diffusion process. Umbrella sampling calculations were started, but the study is not yet finished.

Finally, various point and line defects were introduced in the SAM by removing alkanethiol molecules from the fully packed SAM structure. Upon removal of two alkanethiol molecules, TMA penetrated in the monolayer and diffused to the Au-S interface, where reaction might occur. Hence, small point defects in the SAM may act as nucleation sites for aluminium oxide deposition. DFT calculations could be performed to elucidate the reactivity of TMA at the interface. Will the monolayer be replaced by an aluminium oxide film, as suggested by Avila et al. [95], or will the film grow on top of the monolayer, as hypothesised by Preiner et al. [76]?

A flat, perfect Au(111) substrate was examined, despite experimental observations of various rearrangements, in the assumption that the structure of the interface does not influence the hydrocarbon density in the SAM. As the probability of diffusion was tested in this thesis and not the processes occurring at the gold-SAM interface, the approximation of a flat surface is acceptable. Nevertheless, simulations of the adatom model could shed more light on the role of the interface structure on the diffusion. In addition, a computational study of the SAM passivation of an industrially more relevant substrate, such as copper, has not been performed yet. The passivation of a copper substrate by an alkanethiol SAM was experimentally investigated in the group of prof. Delabie. Octadecanethiol molecules were found not to inhibit the aluminium oxide ALD process on a copper substrate (by analogy to Au(111)), but this observation was not explained.

Further research is needed to elucidate the role of defects in the diffusion of other

ALD precursor molecules as well as the impact of the ALD precursor. Avila et al. [95] suggested that diethylzinc molecules align with the SAM backbones, which increases the monolayer density and therefore enhances the passivating properties towards later cycles, but they were not able to prove it. If so, the selectivity of AS-ALD could be improved by optimising the ALD precursor ligands. On the other hand, the titanium dioxide and tin oxide growth were not equally inhibited, despite having similar precursor molecules. Corrosion passivation studies suggested that the reactivity of the alkanethiol SAM on Au(111) is more important than the defectivity of the monolayer in order to resist corrosion [33]. MD and DFT studies could test the validity of this hypothesis in the context of AS-ALD.

From an experimental point of view, there are several interesting questions to be answered. A detailed study of the SAM degradation and possible reactions with precursors during the ALD process has not been performed yet. By altering the end groups of the SAM, a myriad of chemical and physical properties can be achieved [29]. A variety of SAMs has been deposited and characterised [26, 31, 149]. The efficiency of AS-ALD would benefit from a consistent study of the barrier properties of different monolayers towards the ALD process [13, 24, 96]. Finally, although the AS-ALD technique was successfully tested for several ALD processes on micrometre sized substrates [25, 96], the performance on nanometre scale is unclear. The edge sharpness and concentration of defects near the edge of the SAM pattern need to be investigated in order to develop the high quality patterns required for the application of AS-ALD in the semiconductor industry [24].

Bibliography

- [1] Moore, G. E. (1965). *Electronics*, 38, 114.
- [2] Intel corporation (2015). *Form 10-K*, Santa-Clara, California, p. 151.
- [3] Huang, X., Lee, W. C., Kuo, C., Hisamoto, D., Chang, L., Kedzierski, J., Anderson, E., Takeuchi, H., Choi, Y. K., Asano, K., Subramanian, V., King, T. J., Bokor, J., Hu, C. (2001). *IEE Trans. Electon Dev.*, 48, 880-886.
- [4] Lee, M. L., Fitzgerald, E. A., Bulsara, M. T., Currie, M. T., Lochtefeld, A. (2005). *J. Appl. Phys.*, 91, 011101.
- [5] Lin, B. J. (1987). *Microelectronic engineering*, 6, 31-51.
- [6] Waldrop, M. M. (2016). *Nature*, 530, 145-147.
- [7] McDonnell, M. D., Boahen, K., Ijspeert, A., Sejnowski, T. J. (2014). *Proc. IEEE*, 102, 646-651.
- [8] Editorials (2015). *Nature*, 520, 408.
- [9] Kim, H., Lee, H. B. R., Maeng, W. J. (2009). *Thin solid films*, 517, 2563-2580.
- [10] Puurunen, R. L. (2005). *J. Appl. Phys.*, 97, 121301.
- [11] George, S. M. (2010). *Chem. Rev.*, 110, 111-131.
- [12] Elliott, S. D., Greer, J. C. (2004). *J. Mater. Chem.*, 14, 3246-3250.
- [13] Xu, Y., Musgrave, C. (2004). *Chem. Mater.*, 16, 646-653.
- [14] Delabie, A., Sioncke, S., Rip, J., Van Elshocht, S., Pourtois, G., Mueller, M., Beckhoff, B., Pierloot, K. (2012). *J. Vac. Sci. Technol. A*, 30, 01A127.
- [15] Groner, M. D., Fabreguette, F. H., Elam, J. W., George, S. M. (2004). *Chem. Mater.*, 16, 639-645.
- [16] Puurunen, R. L., Lindblad, M., Root, A., Krause, A. O. I. (2001). *Phys. Chem. Chem. Phys.*, 3, 1093-1102.

- [17] Travis, C. D., Adomaitis, R. A. (2014). *Theor. Chem. Acc.*, 133, 1414.
- [18] Puurunen, R. L., Vandervorst, W., Besling, W. F. A., Richard, O., Bender, H., Conard, T., Zhao, C., Delabie, A., Caymax, M., De Gendt, S., Heyns, M., Viitanen, M. M., de Ridder, M., Brongersma, H. H., Tamminga, Y., Dao, T., de Win, T., Verheijen, M., Kaiser, M., Tuominen, M. (2004). *J. Appl. Phys.*, 96, 4878-4889.
- [19] Butt, H. J., Graf, K., Kappl, M. (2008). *Physics and chemistry of interfaces*, Wiley-VCH, Weinheim, p. 386.
- [20] Khaleel, H. R., Al-Rizzo, H. M., Abbosh, A. I. (2013). *Advancement in microstrip antennas with recent applications.*, Intech, Rijeka, p. 383.
- [21] Willson, C. G., Dammel, R. A., Reiser, A. (1997). *Proc. SPIE*, 3049, 28-41.
- [22] Hashemi, F. S. M., Birchansky, B. R., Bent, S. F. (2016). *Appl. Mater. Interfaces*, 8, 33264-33272.
- [23] Hashemi, F. S. M., Prasittichai, C., Bent, S. F. (2015). *ACS nano*, 9, 8710-8717.
- [24] Jiang, X., Bent, S. F. (2009). *J. Phys. Chem. C*, 113, 17613-17625.
- [25] Dong, W., Zhang, K., Zhang, Y., Wei, T., Sun, Y., Chen, X., Dai, N. (2014). *Sci. Rep.*, 4, 4458.
- [26] Nuzzo, R. G., Dubois, L. H., Allara, D. L. (1990). *J. Am. Chem. Soc.*, 112, 558-569.
- [27] Porter, M. D., Bright, T. B., Allara D. L., Chidsey, C. E. D. (1987). *J. Am. Chem. Soc.*, 109, 3559-3568.
- [28] Dubois, L. H., Nuzzo, R. G. (1992). *Annu. Rev. Phys. Chem.*, 43, 437-463.
- [29] Love, J. C., Estroff, L. A., Kriebel, J. K., Nuzzo, R. G., Whitesides, G. M. (2005). *Chem. Rev.*, 105, 1103-1169.
- [30] Sellers, H., Ulman, A., Shnidman, Y., Eilers, J. E. (1993). *J. Am. Chem. Soc.*, 115, 9389-9401.
- [31] Keller, H., Schrepp, W., Fuchs, H. (1192). *Thin Solid Films*, 210/211, 799-802.
- [32] Ulman, A. (1996). *Chem. Rev.*, 96, 1533-1554.
- [33] Zamborini, F. P., Crooks, R. M. (1998). *Langmuir*, 14, 3279-3286.
- [34] Laibinis, P. E., Whitesides, G. M. (1992). *J. Am. Chem. Soc.*, 114, 9022-9028.
- [35] Strong, L., Whitesides, G. M. (1988). *Langmuir*, 4, 546-558.

- [36] Ferretti, S., Paynter, S., Russell, D. A., Sapsford, K. E. (2000). *Trends Anal. Chem.*, 19, 530-540.
- [37] Gooding, J. J., Praig, V. G., Hall, E. A. H. (1998). *Anal. Chem.*, 70, 2396-2402.
- [38] Wink, T., van Zuilen, S. J., Bult, A., van Bennekom, W. P. (1997). *Analyst*, 122, R43-R50.
- [39] Schreiber, F. (2000). *Prog. Surf. Sci.*, 65, 151-256.
- [40] Guo, Q., Li, F. (2014). *Phys. Chem. Chem. Phys.*, 16, 19074-19090.
- [41] Nuzzo, R. G., allara, D. L. (1983). *J. Am. Chem. Soc.*, 105, 4481-4483.
- [42] Atkins, P., Overton, T., Rourke, J., Weller, M., Armstrong, F. (2010). *Inorganic chemistry*, Oxford university press, 824p.
- [43] Poirier, G. E. (1997). *Chem. Rev.*, 97, 1117-1127.
- [44] Woll, C., Chiang, S., Wilson, R. J., Lippel, P. H. (1989). *Phys. Rev. B*, 39, 7988-7991.
- [45] Beardmore, K. M., Kress, J. D., Gronbeck-Jensen, N., Bishop, A. R. (1998). *Chem. Phys. Lett.*, 286, 40-45.
- [46] Yourdshahyan, Y., Zhang, H. K., Rappe, A. M. (2001). *Phys. Rev. B.*, 63, 081405.
- [47] Gronbeck, H., Curioni, A., Andreoni, W. (2000). *J. Am. Chem. Soc.*, 122, 3839-3842.
- [48] Gottschalk, J., Hammer, B. (2002). *J. Chem. Phys.*, 116, 784-790.
- [49] Hayashi, T., Morikawa, Y., Nozoye, H (2001). *J. Chem. Phys.*, 114, 7615-7621.
- [50] Kondoh, H., Iwasaki, M., Shimada, T., Amemiya, K., Yokoyama, T., Ohta, T., Shimomura, M., Kono, S. (2003). *Phys. Rev. Lett.*, 90, 066102.
- [51] Roper, M. G., Skegg, M. P., Fisher, C. J., Lee, J. J., Dhanak, V. R. (2004). *Chem. Phys. Lett.*, 389, 87-91.
- [52] Kato, H. S., Noh, J., Hara, M., Kawai, M. (2002). *J. Phys. Chem. B*, 106, 9655-9658.
- [53] Fenter, P., Eberhardt, A., Eisenberger, P. (1994). *Science*, 266, 1216-1218.
- [54] Muller-Meskamp, L., Lussem, B., Karthaus, S., Waser, R. (2005). *J. Phys. Chem. B*, 109, 11424-11426.
- [55] Heister, K., Zharnikov, M., Grunze, M. (2001). *J. Phys. Chem. B*, 105, 4058-4061.
- [56] Yeganeh, M. S., Dougal, S. M., Polizzotti, R. S., Rabinowitz, P. (1995). *Thin Solid Films*, 226-229.

- [57] Bain, C. D., Biebuyck, H. A., Whitesides, G. M. (1989). *Langmuir*, 5 (3), 723-727.
- [58] Nuzzo, R. G., Zegarski, B. R., Dubois, L. H. (1987). *J. Am. Chem. Soc.*, 109, 733-740.
- [59] Bryant, M. A., Pemberton, J. E. (1991). *J. Am. Chem. Soc.*, 113, 8284-8293.
- [60] Noh, J., Hara, M. (2000). *Langmuir*, 16, 2045-2048.
- [61] Maksymovych, P., Sorescu, D. C., Yates, J. T. Jr. (2006). *Phys. Rev. Lett.*, 97, 146103.
- [62] Camillone, N. III, Leung, T. Y. B., Scoles, G. (1997). *Surf. Sci.*, 373, 333-349.
- [63] Alves, C. A., Smith, E. L., Porter, M. D. (1992). *J. Am. Chem. Soc.*, 114, 1222-1227.
- [64] Widrig, C. A., Alves, C. A., Porter, M. D. (1991). *J. Am. Chem. Soc.*, 113, 2805-2810.
- [65] Fenter, P., Eisenberger, P., Liang, K. S. (1993). *Phys. Rev. Lett.*, 70, 2447-2450.
- [66] Evans, S. D., Ulman, A. (1990). *Chem. Phys. Lett.*, 170, 462-466.
- [67] Voznyy, O., Dubowski, J. J., Yates, J. T., Maksymovych, P. (2009). *J. Am. Chem. Soc.*, 131, 12989-12993.
- [68] Nagoya, A., Morikawa, Y. (2007). *J. Phys.: Condens. Matter*, 19, 365245.
- [69] Hautman, J., Klein, M. L. (1990). *J. Chem. Phys.*, 93, 7483-7492.
- [70] Mar, W., Klein, M. L. (1994). *Langmuir*, 10, 188-196.
- [71] Bhatia, R., Garrison, B. J. (1997). *Langmuir*, 13, 765-769.
- [72] Schmid, F., Stadler, C., Duchs, D. (2001). *J. Phys.: Condens. Matter*, 13, 8653-8659.
- [73] Zhang, Z. S., Wilson, O. M., Efremov, M. Y., Olson, E. A., Braun, P. V., Senaratne, W., Ober, C. K., Zhang, M., Allen, L. H. (2004). *Appl. Phys. Lett.*, 84, 5198-5200.
- [74] Delamarche, E., Michel, B., Kang, H., Gerber, C. (1994). *Langmuir*, 10, 4103-4108.
- [75] Vericat, C., Vela, M. E., Benitez, G., Carro, P., Salvarezza, R. C. (2010). *Chem. Soc. Rev.*, 39, 1805-1834.
- [76] Preiner, M. J., Melosh, N. A. (2009). *Langmuir*, 25, 2585-2587.
- [77] Poirier, G. E., Pylant, E. D. (1996). *Science*, 272, 1145-1148.
- [78] Cavalleri, O., Hirstein, A., Bucher, J.-P., Kern, K. (1996). *Thin Solid Films*, 392-395.
- [79] Poirier, G. E., Tarlov, M. J. (1994). *Langmuir*, 10, 2853-2856.

- [80] Schönenberger, C., Sondag-Huethorst, J. A. M., Jorritsma, J., Fokkink, L. G. J. (1994). *Langmuir*, 10, 611-614.
- [81] Kawasaki, M., Sato, T., Tanaka, T., Takao, K. (2000). *Langmuir*, 16, 1719-1728.
- [82] Delamarche, E., Michel, B., Gerber, C., Anselmetti, D., Güntherodt, H. J., Wolf, H., Ringsdorf, H. (1994). *Langmuir*, 10, 2869-2871.
- [83] Jung, D. R., Czanderna, A. W. (1994). *Crit. Rev. Solid State Mater. Sci.*, 19, 1-54.
- [84] de Boer, B., Frank, M. M., Chabal, Y. J., Jiang, W., Garfunkel, E., Bao, Z. (2004). *Langmuir*, 20, 1539-1542.
- [85] Ohgi, T., Sheng, H. Y., Dong, Z. C., Nejob, H. (1999). *Surf. Sci.*, 442, 277-282.
- [86] Ohgi, T., Sheng, H. Y., Nejob, H. (1998). *Appl. Surf. Sci.*, 130-132, 919-924.
- [87] Wang, B., Xiao, X., Sheng, P. (2000). *J. Vac. Sci. Technol. B*, 18, 2351-2358.
- [88] Zhu, Z., Daniel, T. A., Maitani, M., Cabarcos, O. M., Allara, D. L., Winograd, N. (2006). *J. Am. Chem. Soc.*, 128, 13710-13719.
- [89] Alkis, S., Cao, C., Cheng, H. P., Krause, J. L. (2009). *J. Phys. Chem. C*, 113, 6360-6366.
- [90] Hooper, A., Fisher, G. L., Konstadinidis, K., Jung, D., Nguyen, H., Opila, R., Collins, R. W., Winograd, N., Allara, D. L. (1999). *J. Am. Chem. Soc.*, 121, 8052-8064.
- [91] Maitani, M. M., Daniel, T. A., Cabarcos, O. M., Allara, D. L. (2009). *J. Am. Chem. Soc.*, 131, 8016-8029.
- [92] Dai, J., Jin, J., Zhang, H., Bi, S. (2012). *Physics Procedia*, 32, 198-205.
- [93] Lee, W., Dasgupta, N. P., Trejo, O., Lee, J., Hwang, J., Usui, T., Prinz, F. B. (2010). *Langmuir*, 26, 6845-6852.
- [94] Färm, E., Vehkamäki, M., Ritala, M., Leskelä, M. (2012). *Semicond. Sci. Technol.*, 27, 074004.
- [95] Avila, J. R., DeMarco, E. J., Emery, J. D., Farha, O. K., Pellin, M. J., Hupp, J. T., Martinson, A. B. F. (2014). *Appl. Mater. Interfaces*, 6, 11891-11898.
- [96] Hashemi, F. S. M., Bent, S. F. (2016). *Adv. Mater. Interfaces*, 3, 1600464.
- [97] Yan, M., Koide, Y., Babcock, J. R., Markworth, P. R., Belot, J. A., Marks, T. J., Chang, R. P. H. (2001). *Appl. Phys. Lett.*, 79, 1709-1711.
- [98] Kobayashi, N. P., Donley, C. L., Wang, S. Y., Williams, R. S. (2007). *J. Cryst. Growth*, 299, 218-222.

- [99] Hashemi, F. S. M., Prasittichai, C., Bent, S. F. (2014). *J. Phys. Chem. C.*, 118, 10957-10962.
- [100] Hong, J., Porter, W. D., Sreenivasan, R., McIntyre, P. C., Bent, S. F. (2007). *Langmuir*, 23, 1160-1165.
- [101] Chen, R., Kim, H., McIntyre, P. C., Bent, S. F. (2004). *Appl. Phys. Lett.*, 84, 4017-4019.
- [102] Leach, A. R. (1996). *Molecular modelling, principles and applications*, Addison Wesley Longman Limited, 595p.
- [103] C. J. (2005). *Essentials of computational chemistry*, John Wiley & Sons Ltd, 596p.
- [104] Abraham, M. J., van der Spoel, D., Lindahl, E., Hess, B. and the GROMACS development team (2015). *GROMACS User Manual version 5.0.7*, p. 296.
- [105] Jewett, J. W. Jr., Serway, R. A. (2010) *Physics for scientists and engineers with modern physics*, Cengage learning, p. 1440.
- [106] Verlet, L. (1967). *Phys. Rev.*, 159, 98-103.
- [107] Hockney, R. W., Goel, S. P., Eastwood, J. W. (1974). *J. Comput. Phys.*, 14, 148-158.
- [108] Jorgensen, W. L., Maxwell, D. S., Tirado-Rives, J. (1996). *J. Am. Chem. Soc.*, 118, 11225-11236.
- [109] Morse, P. M. (1929). *Phys. Rev.*, 34, 57-64.
- [110] Schlick, T. (2010). *Molecular modeling and simulation, an interdisciplinary guide*, Springer, New York, p. 623.
- [111] Kaminski, G., Duffy, E. M., Matsui, T., Jorgensen, W. L. (1994). *J. Phys. Chem.*, 98, 13077-13082.
- [112] Weiner, S. J., Kollman, P. A., Nguyen, D. T., Case, D. A. (1985). *J. Comput. Chem.*, 7, 230-252.
- [113] Brooks, B. R., Bruccoleri, R. E., Olafson, B. D., States, D. J., Swaminathan, S., Karplus, M. (1983). *J. Comput. Chem.*, 4, 187-217.
- [114] Maxwell, D. S., Tirado-Rives, J., Jorgensen, W. L. (1994). *J. Comput. Chem.*, 16, 984-1010.
- [115] Iori, F., Di Felice, R., Molinari, E., Corni, S. (2009). *J. Comput. Chem.*, 30, 1465-1476.
- [116] Darden, T., York, D., Pedersen, L. (1993). *J. Chem. Phys.*, 98, 1008910092.

- [117] Woodcock, L. V. (1971). *Chem. Phys. Lett.*, 10, 257-261.
- [118] Berendsen, H. J. C., Postma, J. P. M., van Gunsteren, W. F., DiNola, A., Haak, J. R. (1984). *J. Chem. Phys.*, 81, 3684-3690.
- [119] Bussi, G., Donadio, D., Parrinello, M. (2007). *J. Chem. Phys.*, 126, 014101.
- [120] Zhu, C., Byrd, R. H., Lu, P., Nocedal, J. (1997). *ACM Trans. Math. Softw.*, 23, 550-560.
- [121] Becke, A. D. (1993). *J. Chem. Phys.*, 98, 5648-5652.
- [122] Weigend, F., Ahlrichs, R. (2005). *Phys. Chem. Chem. Phys.*, 7, 3297-3305.
- [123] Grimme, S., Antony, J., Ehrlich, S., Krieg, H. (2010). *J. Chem. Phys.*, 132, 154104.
- [124] Besler, B. H., Merz, K. M. Jr., Kollman, P. A. (1990). *J. Comput. Chem.*, 11, 431-439.
- [125] Breneman, C. M., Wiberg, K. B. (1990). *J. Comput. Chem.*, 11, 361-373.
- [126] Ochterski, J.W. (2000). Thermochemistry in Gaussian. Gaussian, Inc., Wallingford, 1-19.
- [127] van der Spoel, D., Lindahl, E., Hess, B., Groenhof, G., Mark, A. E., Berendsen, H. J. C. (2005). *J. Comput. Chem.*, 26, 1701-1718.
- [128] Berendsen, H. J. C., van der Spoel, D., van Drunen, R. (1995). *Comp. Phys. Comm.*, 91, 43-56.
- [129] Abraham, M. J., Murtola, T., Schulz, R., Páll, S., Smith, J. C., Hess, B., Lindahl, E. (2015). *SoftwareX*, 1, 19-25.
- [130] Frisch, M. J., Trucks, G. W., Schlegel, H. B., Scuseria, G. E., Robb, M. A., Cheeseman, J. R., Scalmani, G., Barone, V., Mennucci, B., Petersson, G. A., Nakatsuji, H., Caricato, M., Li, X., Hratchian, H. P., Izmaylov, A. F., Bloino, J., Zheng, G., Sonnenberg, J. L., Hada, M., Ehara, M., Toyota, K., Fukuda, R., Hasegawa, J., Ishida, M., Nakajima, T., Honda, Y., Kitao, O., Nakai, H., Vreven, T., Montgomery, J. A., Peralta, J. E., Ogliaro, F., Bearpark, M., Heyd, J. J., Brothers, E., Kudin, K. N., Staroverov, V. N., Keith, T., Kobayashi, R., Normand, J., Raghavachari, K., Rendell, A., Burant, J. C., Iyengar, S. S., Tomasi, J., Cossi, M., Rega, N., Millam, J. M., Klene, M., Knox, J. E., Cross, J. B., Bakken, V., Adamo, C., Jaramillo, J., Gomperts, R., Stratmann, R. E., Yazyev, O., Austin, A. J., Cammi, R., Pomelli, C., Ochterski, J. W., Martin, R. L., Morokuma, K., Zakrzewski, V. G., Voth, G. A., Salvador, P., Dannenberg, J. J., Dapprich, S., Daniels, A. D., Farkas, O., Foresman, J. B., Ortiz, J. V., Cioslowski, J., Fox, D. J. (2013). *Gaussian Inc.*, Wallingford CT.
- [131] Hanwell, M. D., Curtis, D. E., Lonie, D. C., Vandermeersch, T., Zurek, E., Hutchison, G. R. (2012). *J. Cheminform.*, 4, 17.

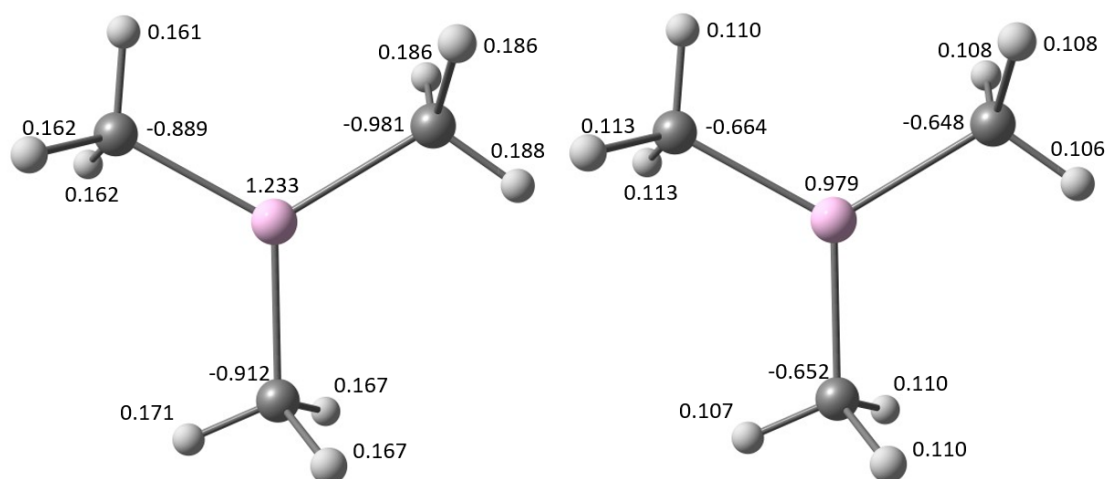
- [132] Humphrey, W., Dalke, A., Schulten, K. (1996). *J. Molec. Graphics*, 14, 33-38.
- [133] Pensa, E., Cortes, E., Corthey, G., Carro, P., Vericat, C., Fonticelli, M. H., Benitez, G., Rubert, A. A., Salvarezza, R. C. (2012). *Acc. Chem. Res.*, 45, 1183-1192.
- [134] Cheng, H. C., Hsu, Y. C., Wu, C. H., Chen, W. H. (2011). *Appl. Surf. Sci.*, 257, 8665-8674.
- [135] Downs, R. T., Hall-Wallace, M. (2003). *Am. Min.*, 88, 247-250.
- [136] Wyckoff, R. W. G. (1963). *Crystal structures*, Interscience publishers, New York, p. 83.
- [137] Hautman, J., Klein, M. L. (1989). *J. Chem. Phys.*, 91, 4994-5001.
- [138] Meija, J., Coplen, T. B., Berglund, M., Brand, W. A., De Bièvre, P., Gröning, M., Holden, N. E., Irrgeher, J., Loss, R. D., Walczyk, T., Prohaska, T. (2016). *Pure Appl. Chem.*, 88, 265-291.
- [139] Jorgensen, W. L., Chandrasekhar, J., Madura, J. D., Impey, R. W., Klein, M. L. (1983). *J. Chem. Phys.*, 79, 926-935.
- [140] Almenningen, A., Halvorsen, S., Haaland, A. (1971). *Acta Chem. Scand.*, 25, 1937-1945.
- [141] Chandrasekhar, J., Spellmeyer, D. C., Jorgensen, W. L. (1984). *J. Am. Chem. Soc.*, 106, 903-910.
- [142] Berthomieu, D., Bacquet, Y., Pedocchi, L., Goursot, A. (1998). *J. Phys. Chem. A*, 102, 7821-7827.
- [143] Krasilnikov, P. M. (2015). *All-atom automatic OPLS-AA topology generator*. [online] Available at: <http://erg.biophys.msu.ru/tpp/> [Accessed 9 Nov. 2016].
- [144] Bensebaa, F., Ellis, T. H., Badia, A., Lennox, R. B. (1995). *J. Vac. Sci. Technol. A*, 13, 1331-1336.
- [145] Bondi, A. (1964). *J. Phys. Chem.*, 68, 441-451.
- [146] Prager, M., Grimm, H., Parker, S. F., Lechner, R., Desmedt, A., McGrady, S., Koglin, E. (2002). *J. Phys.: Condens. Matter*, 14, 1833-1845.
- [147] Mantina, M., Chamberlin, A. C., Valero, R., Cramer, C. J., Truhlar, D. G. (2009). *J. Phys. Chem. A*, 113, 5806-5812.
- [148] Frank, M. M., Chabal, Y. J., Green, M. L., Delabie, A., Brijs, B., Wilk, G. D., Ho, M. Y., da Rosa, E. B. O., Baumvol, I. J. R., Stedile, F. C. (2003). *Appl. Phys. Lett.*, 83, 740-742.

- [149] Hautman, J., Bareman, J. P., Mar, W., Klein, M. L. (1991). *J. Chem. Soc. Faraday Trans.*, 87, 2031-2037.

Appendix A

Figures

A.1 TMA charges

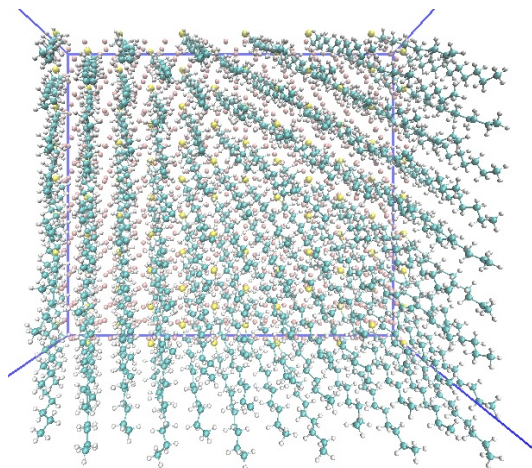


(a) Equilibrium geometry of a TMA molecule with the atomic MK charges indicated.

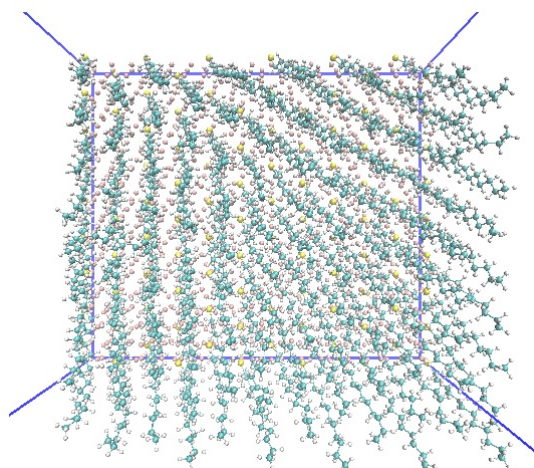
(b) Equilibrium geometry of a TMA molecule with the atomic ChelpG charges indicated.

Figure A.1

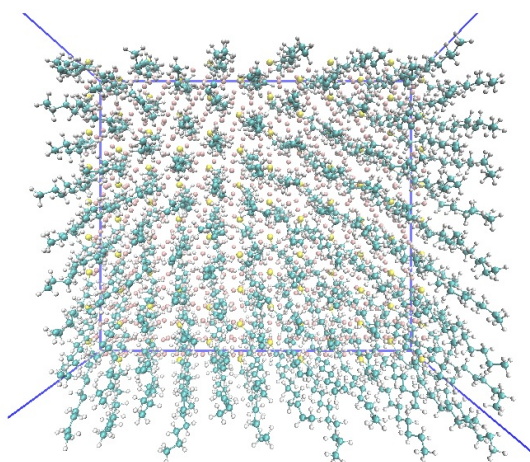
A.2 Temperature dependent SAM conformations



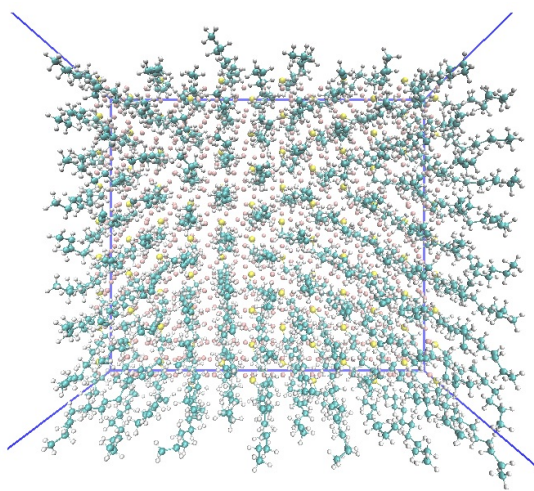
(a) Top view of the monolayer at 200 K.



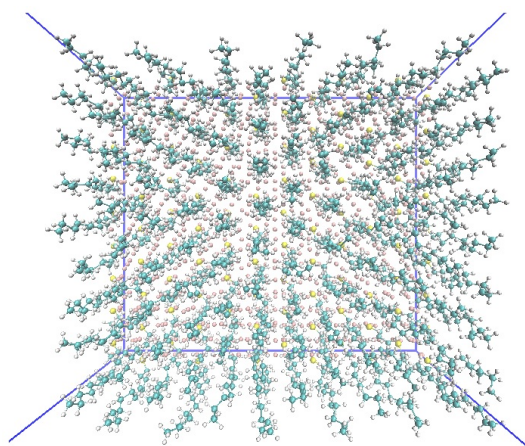
(b) Top view of the monolayer at 300 K.



(c) Top view of the monolayer at 400 K.



(d) Top view of the monolayer at 500 K.



(e) Top view of the monolayer at 600 K.

Figure A.2: Top views of the SAM at various temperatures.

A.3 Dihedral distribution function

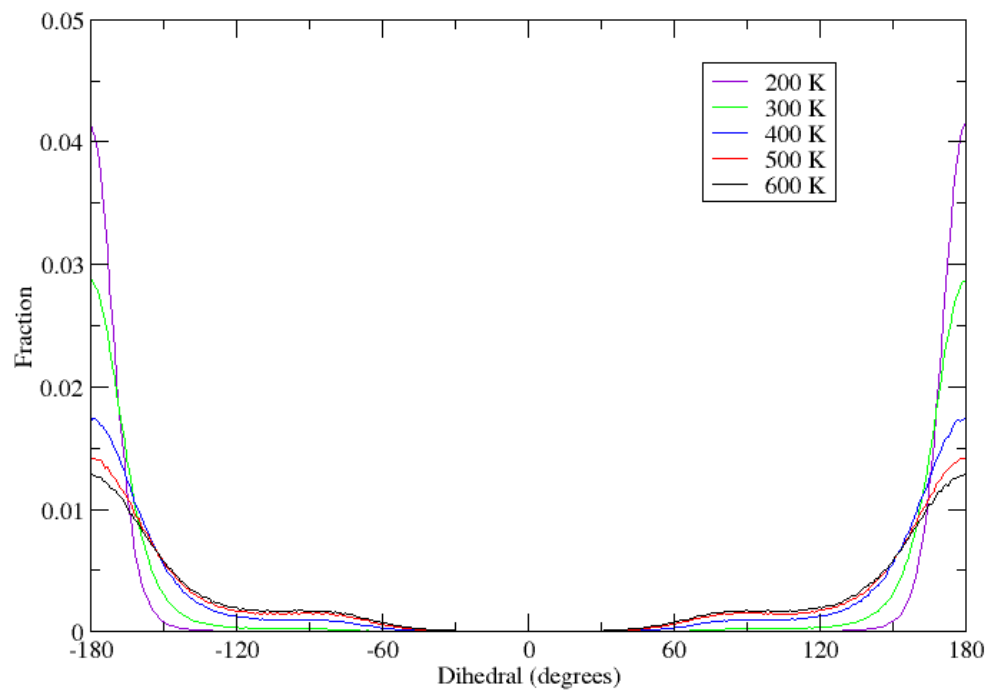
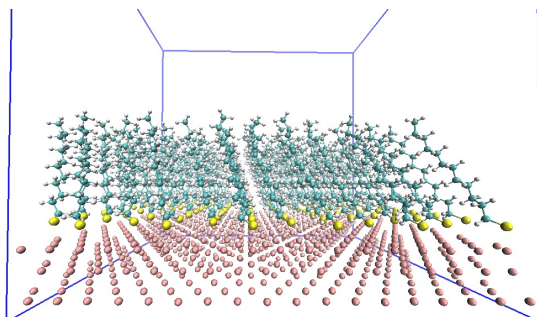
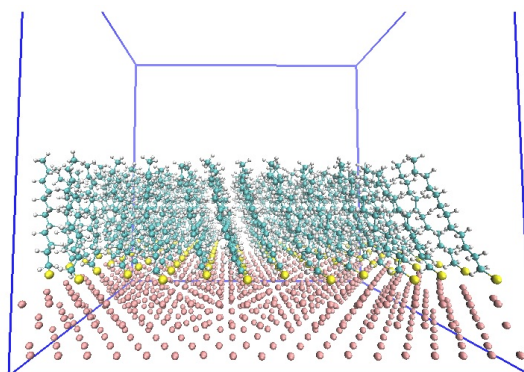


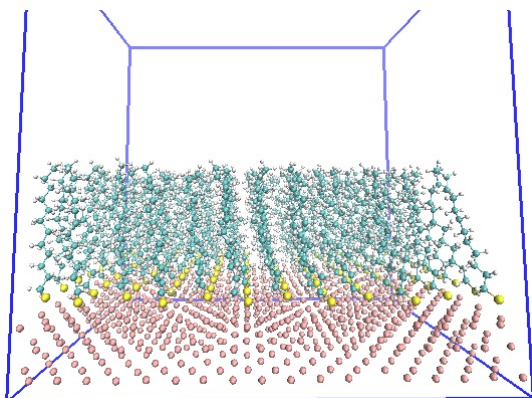
Figure A.4: Distribution of C-C-C-C torsional angles at various temperatures.



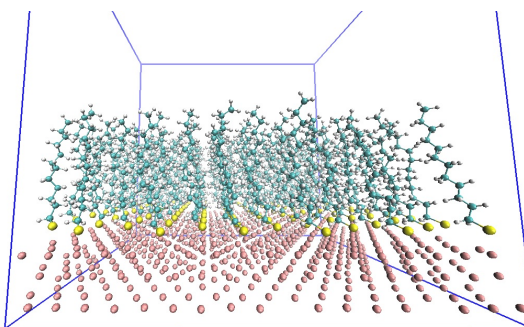
(a) Side view of a monolayer at 200 K.



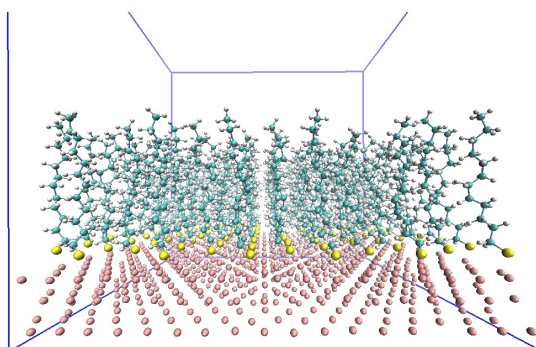
(b) Side view of a monolayer at 300 K.



(c) Side view of a monolayer at 400 K.



(d) Side view of the monolayer at 500 K.



(e) Side view of a monolayer at 600 K.

Figure A.3: Side views of the SAM at various temperatures.

A.4 Average fraction of anti-periplanar torsional angles

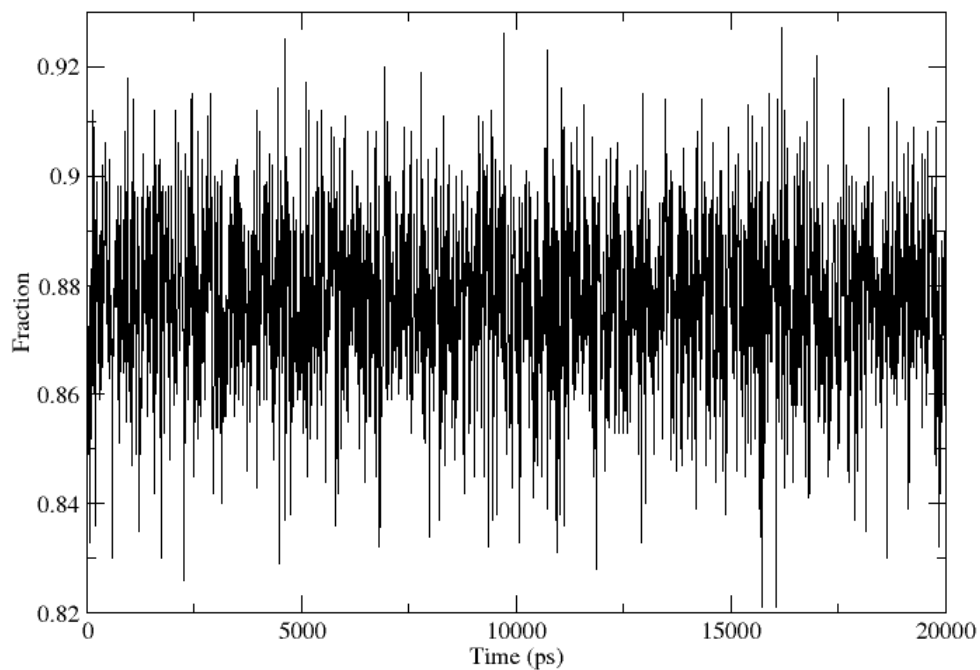


Figure A.5: Time evolution of the average C-C-C-C trans fraction at 600 K. Since the average does not change, the system is fully equilibrated.

Appendix B

TMA vibrational frequencies

Table B.1: TMA vibrational frequencies calculated by DFT and MM.

DFT (cm^{-1})	MM	DFT (cm^{-1})	MM	DFT (cm^{-1})	MM
18.47	11.19	639.08	593.35	1452.76	1737.61
18.47	11.30	714.69	614.02	1454.81	1737.61
44.56	21.89	755.64	702.25	3002.64	3003.48
165.45	70.87	755.64	702.81	3002.64	3003.48
165.45	165.45	1230.20	1449.77	3004.38	3004.40
179.15	165.62	1230.20	1450.23	3057.48	3110.17
513.73	513.95	1232.43	1450.25	3057.48	3110.31
553.78	589.45	1449.30	1736.96	3057.56	3110.31
553.78	589.53	1449.30	1737.05	3086.25	3110.72
590.25	590.26	1451.07	1737.05	3086.63	3111.10
639.07	593.31	1452.76	1737.19	3086.63	3111.11

Appendix C

Parameter files

C.1 Parameter file for the energy minimisations

```
; Run parameters
define = -DPOSRES ; places position restraints on the S and Au atoms
integrator = steep ; the steepest descent minimisation method was used
nsteps = 1000000 ; maximum number of minimisation steps
emtol = 1 ; If the force is lower than 1 kJ/mol nm, convergence is reached.
pbc = xyz ; Periodic boundary conditions in three dimensions

; Cut-offs
cutoff-scheme = Verlet ; scheme for generating the neighbour lists
ns_type = simple ; all atoms are checked to construct the neighbour list
nstlist = 10 ; the neighbour list is updated at every energy calculation
coulombtype = PME ; Particle Mesh Ewald is used for long-range electrostatics
```

C.2 Parameter file for the equilibration runs

```
; Run parameters
integrator = md ; leap-frog integrator
nsteps = 100000 ; the total simulation time equals 100 ps
dt = 0.001 ; 1 fs time step
continuation = no ; first dynamics run
constraints = none ; no constraints
define = -DPOSRES ; places position restraints on the S and Au atoms
pbc = xyz ; Periodic boundary conditions in three dimensions

; Output control
```

```

nstxout = 1000      ; coordinates are saved every 1.0 ps
nstvout = 1000      ; velocities are saved every 1.0 ps
nstenergy = 1000    ; energies are saved every 1.0 ps
nstlog = 1000      ; log file is updated every 1.0 ps
compressed-x-grps = System      ; write everything to a compressed trajectory file

; Cut-offs
cutoff-scheme = Verlet      ; scheme for generating the neighbour lists
ns_type = grid ; Only atoms in neighbouring grid cells are checked
                        to construct the neighbour list
rlist = 1      ; neighbour list cut-off distance (nm)
rcoulomb = 1 ; electrostatic cut-off distance (nm)
rvdw = 1 ; van der Waals cut-off distance (nm)
coulombtype = PME ; Particle Mesh Ewald is used for long-range electrostatics
pme_order = 4 ; cubic interpolation
fourierspacing = 0.16 ; maximal gridspacing for Fourier transformation in PME
DispCorr = EnerPres ; long-range dispersion corrections for the energy
                        and pressure are requested

; Ensemble information
tcoupl = V-rescale ; thermostat
gen_seed = -1 ; the stochastic term is based on a random seed
tc-grps = system ; the whole box is coupled to the external heat bath
tau_t = 0.1 ; time constant (ps)
ref_t = 200 ; reference temperature (K)
pcoupl = no ; no barostat is requested
gen_vel = yes ; initial velocities are assigned according to the
                        Maxwell-Boltzmann velocity distribution function
gen_temp = 200 ; reference temperature for the Maxwell-Boltzmann
                        velocity distribution function

```

An analogous parameter file was used for the production runs, but the velocities and coordinates were read from the output file of the equilibration run (continuation = yes and gen_vel = no). In addition, the simulation time and time steps to save the outputs were increased.

Appendix D

Scripts

D.1 Script to multiply the repeat unit

```
inputfile = input("Enter repeat unit file: ")
if len(inputfile) == 0:
    inputfile = "unitcell.pdb"
x = input("Enter amount of x duplications: ")
xx = int(x)
y = input("Enter amount of y duplications: ")
yy = int(y)
input = open(inputfile,'r')
xvalues = list()
yvalues = list()
zvalues = list()
element = list()
atomtype = list()
for line in input:
    if line.startswith('ATOM') == True:
        word = line.split()
        atomtype.append(word[2])
        xvalues.append(word[5])
        yvalues.append(word[6])
        zvalues.append(word[7])
        element.append(word[10])
newxvalues = list()
newyvalues = list()
newzvalues = list()
newelement = list()
newatomtype = list()
newresidue = list()
```

```

# multiplication of the unit cell
import math
scheiding = 1.5*math.sqrt(3)*2.88375
counter = 0
resnr = 0
for ordinaat in range(yy):
    for abcis in range(xx):
        for coord in yvalues:
            yval = float(coord)
            newyvalues.append(yval + ordinaat*scheiding)
            dummy = xvalues[counter]
            newxvalues.append(float(dummy) - 1.5*2.88375*ordinaat + abcis*3*2.88375)
            if atomtype[counter] == "C8":
                resnr = resnr + 1
                newresidue.append(resnr)
            else:
                newresidue.append(resnr)
            counter = counter + 1
        counter = 0
        newzvalues = newzvalues + zvalues
        newelement = newelement + element
        newatomtype = newatomtype + atomtype

#making the lattice cubic instead of hexagonal
def cubism():
    teller = 0
    for coordinate in newxvalues:
        if coordinate < 7.208:
            newxvalues[teller] = newxvalues[teller] + 3*xx*2.88375
            teller = teller + 1

#writing the file
cubism()
name = "_Au_" + x + "x" + y + ".pdb"
file = open(name,"w")
file.writelines("TITLE " + name + "\n")
for nummer in range(len(newxvalues)):
    c = counter + 1
    file.write("ATOM ")
    file.writelines("%4d %3s" % (c,newatomtype[counter]))
    file.write(" SAM A ")
    file.writelines("%3d %3s %7.3f %7.3f %7s" % (newresidue[counter]," ",

```

```

        newxvalues[counter],newyvalues[counter],newzvalues[counter]))
file.write(" 1.00  0.00      ")
file.writelines("%2s %s"% (newelement[counter],"\n"))
counter = counter + 1
file.write("END")
file.close()

```

D.2 Script to generate the position restraints file

```

x = input("Enter amount of x duplications: ")
xx = int(x)
y = input("Enter amount of y duplications: ")
yy = int(y)
totalsams = xx*yy*3
name = "posre.itp"
file = open(name,"w")
file.writelines("[ position_restraints ]\n")
for nummer in range(totalsams):
    for nr in range(10):
        nr = nr + 1 + 47*nummer
        file.writelines("%6d"% (nr))
        file.writelines("      1 500000 500000 500000\n")
file.close()

```

D.3 Script to generate the position restraints file for a defective monolayer

```

x = input("Enter amount of x duplications: ")
y = input("Enter amount of y duplications: ")
totalsams = int(x)*int(y)*3
res = input("Enter the amount of missing residues: ")
set=set()
for nr in range(int(res)):
    misres = input("Enter number of missing residue: ")
    set.add(int(misres)-1)
nrres = 0
#writing the file
name = res + "posre.itp"
file = open(name,"w")
file.writelines("[ position_restraints ]\n")
for nummer in range(totalsams):

```

```

if nummer in set:
    for nr in range(9):
        nr = nr + 1 + 47*(nummer-nrres) + 9*nrres
        file.writelines("%6d"% (nr))
        file.writelines("      1  500000  500000  500000\n")
        nrres = nrres + 1
else:
    for nr in range(10):
        nr = nr + 1 + 47*(nummer-nrres) + 9*nrres
        file.writelines("%6d"% (nr))
        file.writelines("      1  500000  500000  500000\n")
file.close()

```

D.4 Script to change the TMA - propane distance

```

inputfile = input("Enter file with TMA-propane configuration: ")
if len(inputfile)==0:
    inputfile = "boxedTMApropane.gro"
input = open(inputfile,'r')
xvalues = list()
yvalues = list()
zvalues = list()
atomtype = list()
number = list()
newzvalues = list()
for line in input:
    if line.startswith('      1TMA') == True:
        word = line.split()
        atomtype.append(word[1])
        number.append(word[2])
        xvalues.append(word[3])
        yvalues.append(word[4])
        zvalues.append(word[5])
for coordinate in range(len(zvalues)):
    coord = coordinate + 1
    zval = float(zvalues[coordinate])
    if coord > 13:
        zval = zval + 0.005
        newzvalues.append(zval)
    else:
        newzvalues.append(zval)
name = "newTMApropane.gro"

```

```
file = open(name,"w")
file.writelines("TITLE " + name + "\n")
counter = 0
for nummer in range(len(xvalues)):
    c = counter + 1
    file.write("    1TMA    ")
    file.writelines("%3s %4d"% (atomtype[counter],c))
    file.writelines("%8s %7s %7.3f"% (xvalues[counter],yvalues[counter],
        newzvalues[counter]))
    file.writelines("\n")
    counter = counter + 1
file.write("    5.00000    5.00000    5.00000 ")
file.close()
```

QUANTUM and PHYSICAL CHEMISTRY
Celestijnenlaan 200F bus 2404
3000 LEUVEN, BELGIË
tel. + 32 16 32 73 56
fax + 32 16 32 79 92
www.kuleuven.be

